

5-1-1991

Frequency modulated pulse for ultrasonic b-scan imaging in attenuating medium

Sumat Mehra

Follow this and additional works at: <http://scholarworks.rit.edu/theses>

Recommended Citation

Mehra, Sumat, "Frequency modulated pulse for ultrasonic b-scan imaging in attenuating medium" (1991). Thesis. Rochester Institute of Technology. Accessed from

This Thesis is brought to you for free and open access by the Thesis/Dissertation Collections at RIT Scholar Works. It has been accepted for inclusion in Theses by an authorized administrator of RIT Scholar Works. For more information, please contact ritscholarworks@rit.edu.

**FREQUENCY MODULATED PULSE FOR
ULTRASONIC B-SCAN IMAGING IN
ATTENUATING MEDIUM**

by

Sumat Mehra

B.Sc. University of Poona (India)

(1988)

A thesis submitted in partial fulfillment
of the requirements for the degree of
Master of Science in the Center for
Imaging Science in the College of
Graphic Arts and Photography of the
Rochester Institute of Technology

May 1991

Center for Imaging Science
College of Graphic Arts and Photography
Rochester Institute of Technology
Rochester, New York

CERTIFICATE OF APPROVAL

M.S. DEGREE THESIS

The M.S. Degree Thesis of Sumat Mehra
has been examined and approved
by the thesis committee as satisfactory
for the thesis requirement for the
Master of Science degree

Dr. N.A.H.K. Rao, Thesis Advisor

Dr. Mehdi-Vaez Iravani

Dr. Zoran Ninkov

May 24th, 1991
Date

Center for Imaging Science
Rochester Institute of Technology
Rochester, New York

THESIS RELEASE PERMISSION FORM

Title of Thesis: Frequency Modulated Pulse For Ultrasonic B-Scan
Imaging In Attenuating Medium.

I Sumat Mehra, grant permission to the Wallace Memorial Library of the
Rochester Institute of Technology to reproduce this thesis in whole or in
part provided any reproduction will not be of commercial use for profit.

Sumat Mehra

May 24th 1991
Date

FREQUENCY MODULATED PULSE FOR ULTRASONIC B-SCAN IMAGING IN ATTENUATING MEDIUM

by

Sumat Mehra

Submitted to the Center for Imaging Science in
partial fulfillment of the requirements for the
Master of Science degree at the
Rochester Institute of Technology

ABSTRACT

A rigorous study of a new technique for Ultrasonic B-Scan imaging was performed. This technique made use of a Frequency Modulated (FM) pulse as opposed to the conventional Short pulse for imaging. The simulation studies offered sufficient support for this method, which was then implemented in the laboratory. Experiments were performed on phantoms which mimicked the attenuating medium. Due to the more flexible nature of this FM pulse, changes in the point spread function were studied as a function of bandwidth and depth of the scatterer. The backscattered signal was digitized post processed, and then displayed as a gray-scale B-scan image. The beam profile and the propagation of the pulse in the attenuating medium was carefully studied. Applications for tissue characterizations were explored through simulation studies.

Acknowledgements

I would like to thank everyone at the Center for Imaging Science for being by my side, at every step of my work. Special thanks to Dr. Navalgund Rao, for introducing me to Ultrasound Imaging, suggesting the topic of this thesis and for giving me the opportunity to learn so much.

Thanks to Dr. Mehdi Vaez-Iravani for the inspiring talks, and for his suggestions to the betterment of this work.

Thanks to Dr. Zoran Ninkov for being my third referee.

I would also like to acknowledge the expertise of Rolando Raqueno, without the help of whom I would be unable to obtain my images. Mark Aubry, for being there all along, and providing the ever so important suggestions. My friends Amit, Eran, Katrein, Shyam, Yidong, HongPing and many more for their unending support. And last but not the least, the support of my aunt's family.

*Dedicated to my parents, grandparents and
my ever loving sister Samita.*

Here's to you all...

Contents

Table of Contents	i
List of Figures	iv
List of Tables	viii
Chapter 1 Introduction	1
Chapter 2 Background	4
2.1 Historical Background of Ultrasound Imaging.....	4
2.2 Fundamental Principles of Imaging by Ultrasound.....	7
2.2.1 Propagation of Sound	8
A. Speed.....	8
B. Power	9
C. Attenuation.....	10
2.2.2 Contrast	12
2.2.3 B-Scan Imaging.....	15
2.2.4 Continuous-wave and Pulsed Excitation.....	18
2.2.5 Resolution	20
A. Axial Resolution	21
B. Lateral Resolution	21
2.2.6 Production of Ultrasound - Transducers	23

	A. Vibration and Frequency	24
	B. Bandwidth.....	24
	C. Focusing.....	25
2.3	Principles and Theory of Image Generation.....	25
2.3.1	Pulse-echo Scanning	25
2.3.2	Speckle.....	29
Chapter 3	Experimental Approach	30
3.1	Imaging Scheme with Frequency Modulated Pulse.....	30
3.1.1	Pulse Compression Processing	32
3.1.2	The Three-dimensional Point Spread Function	34
	A. Non-Attenuating Medium.....	34
	B. Attenuating Medium.....	37
3.2	Effects of Attenuation : A Computer Simulation.....	38
3.3	Experimental Setup	43
3.5	Procedure	49
Chapter 4	Results.....	57
4.1	Results	57
4.2	Analysis	72
4.3	Discussion	77
4.3.1	Spectrum of the Backscattered Signal	78
4.3.2	Axial Resolution.....	79
4.3.3	Frequency Downshift.....	80
4.3.4	Lateral Resolution in Far-Field.....	81
4.3.5	Lateral Resolution in the Near-Field.....	83
Chapter 5	Applications.....	85
5.1	Reduction of Speckle Noise	85
5.2	Tissue Characterization using Speckle Statistics	87
5.3	Reduction of Cavitation Possibilities.....	87

Chapter 6	Conclusions and Recommendations	89
Appendix A	Solving for Impulse Response in Attenuating Medium	92
Appendix B	Discussion of Program for FM Pulse Scheme Simulation	94
Appendix C	Polynomial Waveform Generator	102
Appendix D	Transmitter-Receiver Circuit	107
Appendix E	Table for Transducer Transfer Function Measured	108
Appendix F	Analogic Corporation Dual Pre-Amp	109
Appendix G	Analogic Corporation Data 6000	110
Appendix H	Program for Converting Data6000 Format to ASCII	119
Appendix I	Program for Converting A-Scan data to a B-Scan Image	121
Appendix J	Applications	125
References		132

List of Figures

Figure 2.1 Range of speeds	9
Figure 2.2 Attenuation variations in various media.....	11
Figure 2.3 Mechanical motion and image format for (a) linear, (b) sector, and (c) arc B-scans.....	16
Figure 2.4 Fraunhofer and (on-axis) Fresnel solutions for the pressure amplitude in front of a plane circular source of radius a radiating a continuous sine wave	19
Figure 2.5 Axial Resolution	22
Figure 2.6 Lateral Resolution.....	22
Figure 2.7 Digital simulations of processing steps.....	28
Figure 2.8 Artefactual details	28
Figure 3.1 Post-processing step of pulse compression	33
Figure 3.2 (a)-(d) Simulation of frequency dependent attenuation of the medium in the FM pulse imaging process.....	40

Figure 3.3 Backscattered RF signals from various depths (a) 2 cm, (b) 6 cm, (c) 10 cm. & (d) is a plot of the time-bandwidth product as a factor of depth.....	41
Figure 3.4 (a)-(b) shows the pulse spectrum for signals reflected from 2cm and 10cm respectively.....	42
Figure 3.5 Time-bandwidth product as a function of center frequency f_0 and depth z , for attenuating medium of $a_0 = 0.01725$ Np/cm/MHz (a) $\Delta f = 0.5$ MHz, (b) $\Delta f = 2.0$ MHz.....	42
Figure 3.6 Block diagram of experimental setup used	44
Figure 3.7 Instruments used in the experimental setup	44
Figure 3.8 Transducer transfer function, evaluated using a hydrophone.....	46
Figure 3.9 Data6000 processing in Attenuating Medium.....	48
Figure 3.10 The phantom with targets and axis shown.....	50
Figure 3.11 RF signal along center scan for (a) non-attenuating and (b) attenuating medium	52
Figure 3.11 Flow chart of all the data recorded, for various parameters.....	54
Figure 3.13 (a) Gray scale Backscattered RF signal, (b) post processed (after crosscorrelation) signal and (c) signal after envelope detection.....	55
Plate 4-1 Block diagram of settings of the pictures in the templates shown later on in this section.....	59
Figure 4.1 Envelope detected data of 2nd scatterer (a)-(b) Non Attenuating Medium (c)-(d) Attenuating Medium for 1MHz and 2MHz bandwidth, $f_0 = 2.4$ MHz. Crosscorrelation done with input FM pulse	62

Figure 4.2 Envelope detected data of 3rd scatterer (a)-(b) Non Attenuating Medium (c)-(d) Attenuating Medium for 1MHz and 2MHz bandwidth, $f_0 = 2.4$ MHz. Crosscorrelation done with input FM pulse 63

Figure 4.3 Envelope detected data of 5th scatterer (a)-(b) Non Attenuating Medium (c)-(d) Attenuating Medium for 1MHz and 2MHz bandwidth, $f_0 = 2.4$ MHz. Crosscorrelation done with input FM pulse 64

Figure 4.4 Envelope detected data of 2nd, 3rd & 5th scatterers (a)-(b) Non Attenuating Medium (c)-(d) Attenuating Medium for 1MHz and 2MHz bandwidth, $f_0 = 2.4$ MHz. Crosscorrelation done with input FM pulse 65

Figure 4.5 Envelope detected data of 2nd scatterer (a)-(b) Non Attenuating Medium (c)-(d) Attenuating Medium for 1MHz and 2MHz bandwidth, $f_0 = 2.4$ MHz. Crosscorrelation done with 5th scatterer (central scan) 66

Figure 4.6 Envelope detected data of 3rd scatterer (a)-(b) Non Attenuating Medium (c)-(d) Attenuating Medium for 1MHz and 2MHz bandwidth, $f_0 = 2.4$ MHz. Crosscorrelation done with 5th scatterer (central scan) 67

Figure 4.7 Envelope detected data of 5th scatterer (a)-(b) Non Attenuating Medium (c)-(d) Attenuating Medium for 1MHz and 2MHz bandwidth, $f_0 = 2.4$ MHz. Crosscorrelation done with 5th scatterer (central scan) 68

Figure 4.8 Envelope detected data of 2nd, 3rd & 5th scatterers (a)-(b) Non Attenuating Medium (c)-(d) Attenuating Medium for 1MHz and 2MHz bandwidth, $f_0 = 2.4$ MHz. Crosscorrelation done with 5th scatterer (central scan) 69

Figure 4.9 Envelope detected data of 2nd scatterer (a)-(b) Non Attenuating Medium (c)-(d) Attenuating Medium for 1MHz and 2MHz bandwidth, $f_0 = 2.4$ MHz. Crosscorrelation done with input FM pulse 70

Figure 4.10 Envelope detected data of 3rd scatterer (a)-(b) Non Attenuating Medium (c)-(d) Attenuating Medium for 1MHz and 2MHz bandwidth, $f_0 = 2.4$ MHz. Crosscorrelation done with input FM pulse **71**

Figure 4.11 Envelope detected data of 5th scatterer (a)-(b) Non Attenuating Medium (c)-(d) Attenuating Medium for 1MHz and 2MHz bandwidth, $f_0 = 2.4$ MHz. Crosscorrelation done with input FM pulse **72**

Figure 4.12 Comparison of power spectrums for (a) input FM pulse, (b) 2nd scatterer, (c) 3rd scatterer and (d) 5th scatterer **75**

Figure 4.13 Plot of observed central frequency f_0 versus depth **76**

Figure 4.14 Plot of observed bandwidth Δf versus depth **77**

Figure A-1 (a) Impulse response for attenuating medium, (b) FM pulse generated by an ASYSTANT simulation program, (c) Backscattered RF signal & (d) Post processing crosscorrelation step result..... **97**

List of Tables

Table 2.1 Characteristic Impedance of various media.....	13
Table 4.1 Analysis of backscattered RF signal, and of envelope after post processing	74
Table B-1 Parameter evaluation chart.....	101
Table C-1 Evaluating FM pulse equation for f_0 and Δf	104
Table E.1 Transducer response chart.....	108
Table F-1 Calibration of the dual pre-amp.....	109

Chapter 1

Introduction

The importance of accurate investigation and diagnosis in the management of all disease is unquestionable. For this purpose, various imaging modalities and techniques have been studied and applied. Medical imaging is no longer restricted to a single hospital department, but on the contrary, it has become a team effort on the part of specialists in their individual field of expertise.

It is difficult today to imagine how diagnosis was carried out without images. There are few people alive whose experience pre-dates the use of x-rays to form images. There are however many people who can remember how things were done before ultrasound, radionuclide, nuclear magnetic resonance and other techniques became available. They have lived in a unique and exciting period in which the science of diagnostic medicine has matured and diversified [Webb88].

Ultrasound is thus only one of the modalities in use for diagnostic purposes. It has its advantages and disadvantages over other techniques, depending on the application. Since ultrasound is highly attenuated by bone structure, it is normally used for tissue characterization in areas where there is less presence of bone. Ultrasound is non-ionizing and is thus given preference for fetus detection and monitoring. Like x-ray radiation, ultrasound penetrates and interacts with the body. Information about the internal structures is encoded in the transmitted and scattered signals, which are detected by the imaging system, and decoded. Compared with light and x-rays, ultrasonic waves propagate sufficiently slowly so that for the distance travelled inside the body, transit times are easily measurable and radar like pulse echo methods may be used to create images. At the same time the waves propagate fast enough to allow real time imaging of moving objects such as the living heart. It takes about 80 ms for the data to be collected and constructed into an image, thus allowing for constant monitoring, and studying irregularities in the beating heart.

Ultrasound is also a coherent radiation, and thus pronounced interference effects tend to dominate the images. Ultrasound receivers are sensitive to amplitude and thus produce coherent interference-like fluctuations, in apparent received magnitude, due to integration over a non-planer received wave.

Ultrasound refers to frequencies of sound, above the bandwidth of human hearing. Typically the audible range of the human ear is 16 Hz - 20 KHz. Various frequency bands are applied in different areas of application. For SONAR applications it goes to about 300

KHz, for medical diagnosis and therapy 0.8 - 15 MHz, and for acoustic microscopy 12 MHz to above 1 GHz.

The area of interest for the purpose of this thesis lies in medical diagnostic imaging. A new technique is being studied for imaging purposes, which makes use of a *Frequency Modulated-pulse*, as opposed to the conventional *Short-pulse*. Compared to the short pulse, the frequency modulated(FM) pulse lasts over a longer period of time. Also the intensity associated with the FM pulse is much smaller than that of the short pulse. For comparison, a short pulse generally has amplitudes in the order of 100 W/cm^2 whereas the FM pulse has amplitudes in the order of 10 W/cm^2 . This reduces the amount of power subjected to the human body, without loosing out on any image resolution[Rao90]. Laboratory experiments were performed using *phantoms* which consist of several stationary scatterers, and a liquid medium which can be varied according to the requirement.

The experimental procedures and the results were recorded, and are categorically described in the chapters ahead. B-scan images were created for several sections of the phantom, also shown later.

Chapter 2

Background

The following sections will discuss the historical and theoretical background of ultrasound imaging. They will lay the foundation for all the physical principles of ultrasound that will be used as part of this thesis.

2.1 Historical Background of Ultrasound Imaging

Ultrasound, which has frequency beyond the audible range of the human ear, is used by bats for navigation. Over the last century, the use of ultrasound for imaging has been discovered and developed by man.

It was in 1880 that the Curie brothers discovered a means to produce and detect high-frequency sound waves [Hendee80]. It was not until 40 years later that the usefulness

of ultrasound was demonstrated in the detection of unseen underwater objects by Langevin, a former student of Pierre Curie. The Titanic disaster in 1912 and the threat of submarines to the Allied Powers in the First World War, made it essential to find means of detecting objects underwater. In the 1920s Sokolov suggested that the technique could be used to detect hidden flaws in metals. Since then the seeing power of ultrasound came into wide acceptance.

During the Second World War, it became evident that a faster and more effective technology had to be developed to detect, and to range, submarines which were a menace at sea. Improvisations evolved into the sophisticated Sound Navigation and Ranging (SONAR) systems so important in the Second World War. These were based on pulse-echo principles, like RADAR (Radio Detecting and Ranging), which for obvious military reasons were given much effort for development during the war. Sokolov's theory of metal flaw detection also gained importance, and Firestone devised a machine called the Reflectoscope to do this. Industry owes much to this technique.

The biological effects of ultrasound were noted at an early stage. At first it was valued as a heating agent, used therapeutically and destructively. Later, its applications for imaging and seeing inside the body were described by the Dussik brothers, in Austria in 1937. Their crude transmission technique, used to produce 'hyperphonograms' of the head was of little clinical value. In 1949, Ludwig and Stuthers at M.I.T. picked up from the success and experience of the US military, and successfully detected gallstones and foreign bodies in tissues using the pulse-echo techniques [Hendee80].

In Minneapolis, John J. Wild showed it was possible to detect tumors of the breast and brain by comparing their echo patterns with those of normal tissue. In Denver, Douglas Howry's group concentrate on using pulsed ultrasound to produce pictures of the human body, and in 1952 published two-dimensional ultrasonic tomograms using a prototype machine, shortly after Wild had done so [Rose79].

At the same time, work was proceeding in ultrasonics in Europe and Japan. Turner in London used an industrial flaw detector to recognize echoes from the head and heart. In Japan, Kikuchi and colleagues were studying brain tumors. In Sweden, Hertz described the principles of echocardiography. Leskell, a Swedish neurosurgeon, saved the life of a 16-month boy, by removing the blood clot responsible for a midline shift in the brain, detected by ultrasound. Echo-encephalography became established after publication of Leskell's work in 1956, and was automated in the 1960s. In 1958, Ian Donald and Tom Brown in Scotland, produced the first contact scanner, with applications being diversified to obstetrics and gynecology. Simultaneously in the USA, ultrasonic techniques were being applied in ophthalmology [Hendee80].

By the late 1950s, therefore, diagnostic ultrasound was of proven clinical value in the investigation of the eye, the brain, the heart, the abdomen and the pelvis. For the next decade several developments were made in recognition of large echoes from organ boundaries. In 1972, Wells and Mountford quantified small echoes from liver parenchyma and studied effects of disease upon them. The stage was set for tissue characterization by ultrasound and, in 1972, Kosoff in Australia described how this could be achieved by gray scale techniques, which for the first time made it possible to image not only the large

echoes from organ boundaries, but also the small ones from tissue infrastructure. Also in the early 1970s, real-time systems were designed to produce instantaneous moving images of moving structures. The pioneers in the field were Somer and Bom in the Netherlands.

By the 1980s, ultrasound was widely in use for diagnostic purposes. Several improvisations were made on instrumentations, and color Doppler imaging was also introduced. So after a long gestation and childhood, diagnostic ultrasound is now reaching adolescence with a potential of considerable further growth. For further insight into the history the reader is referred to Webb88 and Hendee80.

2.2 Fundamental Principles of Imaging by Ultrasound

The following section contains a description of the fundamental principles of ultrasonic imaging. The objective behind this description is to provide the reader with a basic knowledge of the physics involved in ultrasound. This section will thus be the basis of all the experimental and theoretical work performed as part of this thesis. Although the theory described here is for conventional short-pulse technique, it is also applicable to Frequency Modulated pulse imaging which is the subject of this thesis.

2.2.1 Propagation of Sound

Sound waves are mechanical waves that involve physical displacement of the material particles through which the sound propagates. The sound energy used in medical diagnostic equipment travels in the form of a longitudinal wave, that is, one in which the particle motion is in the same direction as the wave propagation. Transverse waves, in which the particle motion is perpendicular to the direction of wave propagation, have not been used for medical diagnosis because of the extremely high attenuation of such waves in biological media[Havlice79,Swenberg88].

A. Speed

The speed of propagation c of the longitudinal wave in a liquid medium is determined by the "elastic" properties of that medium, specifically its mean density ρ and the bulk modulus B , through the equation:

$$c = \sqrt{B/\rho} \quad (2.1)$$

Although the speed of sound is found to be frequency dependent (a phenomenon known as dispersion) [Hertzfeld59], the small dispersion that has been measured for biological materials is not important for most imaging instruments available today. A list of the range of speeds in some typical biological media is shown in figure 2.1. It should be

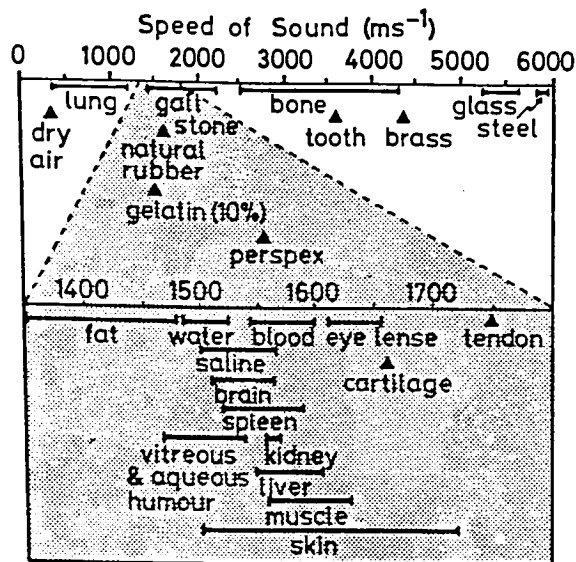


Figure 2.1 Ranges of measured values for speed of sound in various biological and non-biological media. The data for soft tissues and biological liquids, which falls within a narrow range are shown using an expanded scale in the shaded portion of the figure. (After Webb88, which also contains reference to the original source.)

noted that the speed of sound increases with the material density. In the intermediate density of soft tissue at 37 °C (normal body temperature), the sound speed is ~1540 m/sec. As soft tissue density varies little throughout the human body, one can take the speed of ultrasound in the body to be constant at 1540 m/sec.

B. Power

The amplitude or power of the ultrasound beam used in diagnostic imaging is relatively low. The amplitude is measured in units of the decibels, defined as

$$\text{dB} = 20\log\left(\frac{A_2}{A_1}\right) \quad (2.2)$$

where A_2 and A_1 are the respective amplitudes of the two different signals or echoes. In a typical pelvic ultrasound imaging device, the echoes received from the soft tissue vary in strength from 0 to 100 dB; this corresponds to a millionfold change in amplitude.

C. Attenuation

Another important aspect of sound waves is their attenuation as they propagate through a medium. As sound propagates, its intensity I generally diminishes with distance of propagation z , according to:

$$I = I_0 \exp(-2\alpha z). \quad (2.3)$$

I_0 is the intensity at $z = 0$ and α is the amplitude attenuation coefficient. Unlike the speed of sound, the attenuation coefficient is highly frequency dependent [Hertzfeld59,Webb88], a fact which has significant impact on equipment design and performance. For a tissue, the attenuation coefficient increases approximately linearly with frequency (see figure 2.2), giving rise to the ultrasonic instrument designer's rule for soft tissue:

$$\alpha = A \text{ dB/cm/MHz} \quad (2.4)$$

where, for a wide range of soft tissue, $A = 1$.

The convenient average value of the attenuation coefficient of soft tissue is $1 \text{ dBcm}^{-1}\text{MHz}^{-1}$. Hence, a 3-MHz sound beam which has travelled a 20-cm distance through soft tissue is 60 dB below its initial intensity level. Although this additional loss of

signal could be compensated for by increasing the transmitted power, this could raise the intensity to dangerous levels. Hence it is clear why 3-MHz rather than 10 MHz, is used for imaging structures deep in the body. However if the body structures of interest lie near the skin surface or if the body itself is very small (as in an infant), higher frequencies may be used. This limitation on frequency impacts equipment performance, because the frequency f , and sound speed c , determine the wavelength λ , of the sound beam through the equation

$$\lambda = \frac{c}{f} \quad (2.5)$$

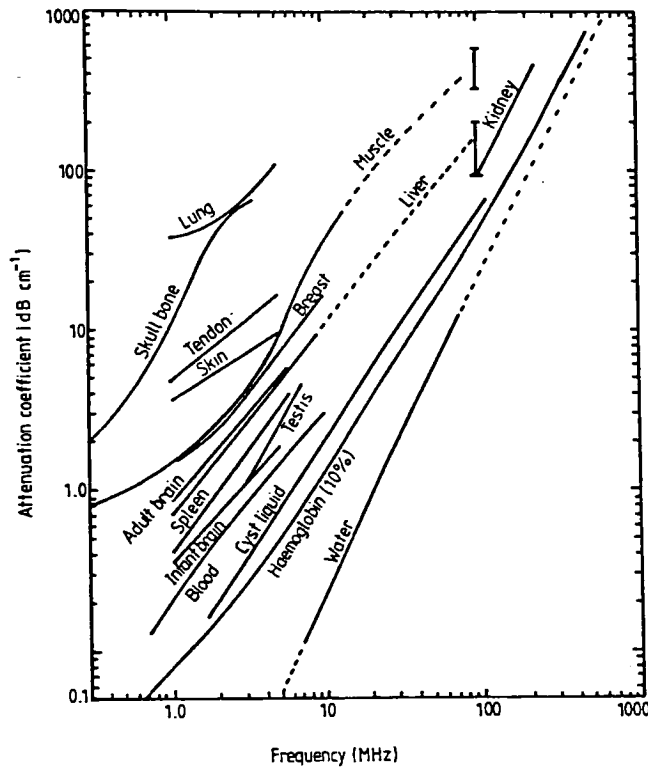


Figure 2.2 Illustration of the general trends observed for the variation of the ultrasonic attenuation coefficient (and its frequency dependence) over various biological tissues and solutions. (After Webb88, which also contains the reference to the original source of data.)

2.2.2 Contrast

In an optical image a structure distinguishes itself from surrounding structures by variations in reflectivity, attenuation, color (frequency dependence of perception), "texture" and index of refraction. In acoustics, exactly the same sources of contrast are available although only attenuation, reflectivity and texture are commonly employed in instrumentation. Attenuation differences between various body structures are most important for those instruments which provide transmission images of the body. Reflectivity, the most important contrast agent for those instruments which provide reflection images of the body, is used here in the narrow sense of an absolute reflection coefficient at a plane boundary between two different media. Reflectivity is determined, for structures larger than a few wavelengths, by the characteristic impedance of the two adjoining layers [Kinsler62]. The characteristic impedance of a material Z , an acoustic concept analogous to the concept of impedance in electricity, is defined as the product of material density ρ , and sound speed c :

$$Z = \rho c. \tag{2.6}$$

Listed in Table 2.1 are some values of characteristic impedance for a variety of biological media. The power reflection coefficient R for a normally incident sound beam traveling from a medium with impedance Z_1 into a medium with impedance Z_2 is given by[Wells69]:

Medium	Characteristic Impedance ($10^6 \text{ kgm}^{-2}\text{s}^{-1}$)
Water	1.48
Air	0.0004
Amniotic Fluid	1.5
Fat	1.34-1.39
Soft Tissue (average)	1.62
Liver	1.66
Kidney	1.63
Muscle	1.71
Spleen	1.65
Bone	7.8
Vitreous of eye	1.52

Table 2.1 Characteristic Impedance of various media

$$R = \left(\frac{Z_2 - Z_1}{Z_2 + Z_1} \right)^2 \quad (2.7)$$

The greater the impedances of the adjoining tissues, the greater the amount of energy reflected from the boundary. In soft tissues the reflection coefficient varies from -20 dB (between fat and muscle)¹ to -45 dB (between kidney and spleen). These are low level reflections (less than 0.5 percent) so that most of the acoustic energy is transmitted through the interface and is available for imaging deeper structures. In some cases, however, a very high level reflection may take place, as in a bone/muscle interface which has a reflection coefficient of -4 dB. In such a case considerably lower energy is transmitted, not very much is available for imaging deeper structures, and a "shadow" appears in a reflection mode image. This "shadowing", when it occurs in a region where

¹That is, the reflected signal is -20 dB from the incident signal.

there is no normal anatomical reason for it, is an important indicator of abnormality. It has been used, for example, to distinguish between soft and calcified atherosclerotic plaque in the carotid arteries [Evans79, Olinger78] and to identify stones in the gall bladder or kidney.

The amount of sound, and its spatial distribution reflected from an object, depends not only on the difference between the acoustic impedance of the object and its surroundings, but also on the physical size, orientation, and shape of the object. Objects much smaller than an acoustic wavelength reflect sound according to the Rayleigh scattering theory; hence, they exhibit a fourth power frequency dependence with a wide angular field distribution [Linzer76]. On the other hand, objects with dimensions larger than an acoustic wavelength (specular reflectors) reflect sound, independent of frequency, toward a direction which is dependent on the orientation of the object and with an angular field distribution which is dependent on the incident sound field, and the shape of the object. It is experimentally observed that some body structures produce spatial echo patterns that have a different textural appearance than others, and this difference acts as a contrast agent. For example, the wall of a blood vessel has a characteristic smooth specular appearance whereas a thyroid gland has a characteristic granular appearance[Havlice79].

2.2.3 B-Scan Imaging

B-Scanning, or brightness mode scanning, provides a two-dimensional, cross sectional reflection image of the object that is scanned [Reid52]. A *B-Scan* image is formed by sweeping a narrow acoustic beam through a plane and positioning the received echoes on a display such that there is a correspondence between the display scan lines and the direction of acoustic propagation in the tissue. Generally the same transducer is used to both send and receive the acoustic signals. A fundamental feature of a B-Scan image is that one of the dimensions is inferred from the arrival time of echoes of a short acoustic pulse as they reflect from structures along a (presumed) straight line path. Signals received from structures close to the transducer arrive earlier than from structures far from the transducer [Erikson74]. The other (transverse) dimension is obtained by moving the transducer (either physically by mechanical means, or apparently by electronic means) so that a different straight line path through the object is interrogated by another short acoustic pulse. This process is continued until the entire object region of interest is scanned. Some means of tracking the propagation path through the object is required in order to unambiguously define the image.

As shown in figure 2.3, there are typically three scan modalities: linear, sector, and arc. For illustrative purposes the transducer size indicated in the figure is exaggerated; typically, the transducer diameter is only a small fraction of the scanned dimension. In a linear scan the transducer moves in a straight line. Note that the field-of-view in this direction is limited by the length of travel of the transducer. However in the time (or depth) dimension, the field-of-view is limited only by the depth of penetration (i.e., the frequency

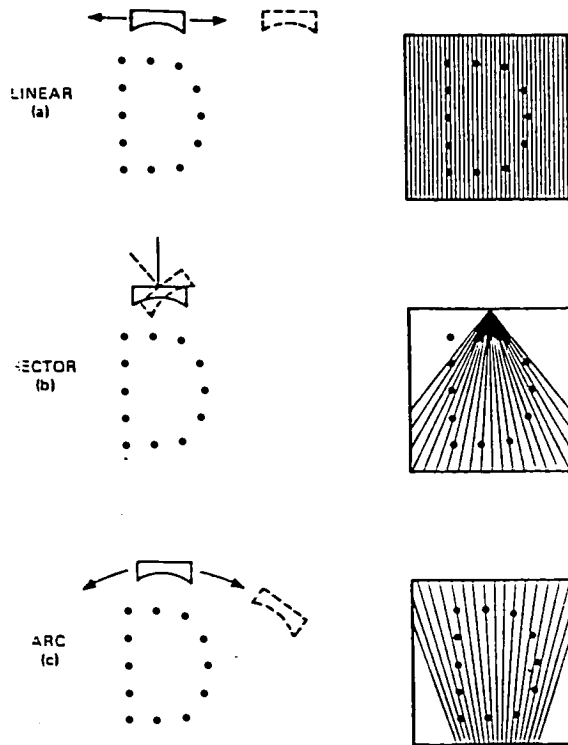


Figure 2.3 Mechanical motion and image format for (a) linear, (b) sector, and (c) arc B-scans. Adapted from Havlice79.

and attenuation) or the physical size of the object being scanned. One advantage of this technique is that the image may consist of a uniform line density which results in a constant spatial sampling rate of the object and a pleasing display on the monitor. In the sector scan the transducer position remains fixed at a point on or above the object but is swept through an angular sector [Tucker58]. Note that in this case the field-of-view increases with depth of penetration. However the line density diminishes as the field-of-view expands. This type of scan is particularly well suited to imaging through narrow apertures, such as imaging the

heart through the ribs. In an arc scan the transducer is moved along the arc of a circle, which gives rise to an image format that is the inverse of the sector scan [Baum78]. Note that the field-of-view is largest near the transducer and decreases with depth of penetration. The arc scan (or a close approximation to it) is most often encountered in manual scans of the abdomen, the surface of which resembles the arc of a circle.

In addition to the above described scanning modalities, compound scanning is also utilized. Compound scan is a combination of a sector scan either with a linear scan or an arc scan. The sector is usually much smaller here, but object points are imaged by more than one acoustic pulse along different ray paths. Compound scanning is used to overcome the problem of imaging specular reflectors, and objects lying behind specular reflectors. A specular reflector reflects sound toward a direction which is dependent on its orientation to the transducer. Hence, it is possible for an incident sound beam to reflect from a specular reflector in a direction such that the reflected sound beam does not return to the transducer. This causes a flaw in the image.

It should be pointed out that the present day electronic scanning systems are extremely fast and are capable of producing "real time"² images, i.e. they are capable of acquiring and displaying dynamic images of organs in motion. There are various techniques and parameters involved in B-Scan imaging, which are beyond the scope of this thesis. For further information on the subject one can refer to Baum78, Hykes85 and Fish90.

² Typically the images are obtained in a small fraction of a second.

2.2.4 Continuous-wave and Pulsed Excitation

The performance of an imaging system depends on various factors. The distribution of acoustic field parameters, as a function of both space and time, in front of a radiating source of ultrasound, and the corresponding spatial and temporal sensitivity pattern of a receiver, are some of these critical factors. Prediction of acoustic fields is often possible by calculation, particularly for many of the simple shapes of sources and detectors in practice.

The direct application of Huygens' principle to a distribution of elemental point sources of appropriate strength and phase, covering a source vibrating with a continuous sinusoidal displacement, leads to the Fresnel theory. Analytical solutions exist for the on-axis field variations, and for the field distribution far from the source, for a plane circular transducer (see figure 2.4) and other simple shapes such, as a line source. The model of a continuous-wave, plane, circular source helps in understanding the general features of a radiation field pattern. One of the main features is the (somewhat arbitrary) division of the radiation field into two regions. The first is the Fresnel zone or 'near field', which is near the transducer and where pronounced interference maxima and minima occur but where most of the energy is confined within a transducer radius of the central axis. The other is the Fraunhofer zone or 'far field', which is further away from the transducer and where the wave is more uniform but tends towards a spherically divergent wave whose amplitude is modulated as shown in the figure.

The on-axis variation is such that, starting with a value of zero at infinity, as one moves closer to the source, alternate maxima and minima occur at distances x_m given by :

$$x_m = (a^2/m\lambda) - (m\lambda/4) \quad (2.8)$$

where a is the radius of the transducer and m is an odd integer for maxima and an even integer for minima [Webb88]. The position of x_I , whose approximate value is a^2/λ for $a \gg \lambda$ (the so-called 'last axial maximum'), is usually regarded as the boundary between the two zones. In the far field most of the energy is contained within the main lobe, defined by the first off-axis minima, which occur at a divergence angle θ given by

$$\sin\theta \approx 0.61 \frac{\lambda}{a} \quad (2.9)$$

Note that the quantity x_I has no physical meaning if $a < \lambda/2$, in which case $x_I \leq 0$ and θ is 90° ; i.e. there is no near field and the transducer behaves much like a point source.

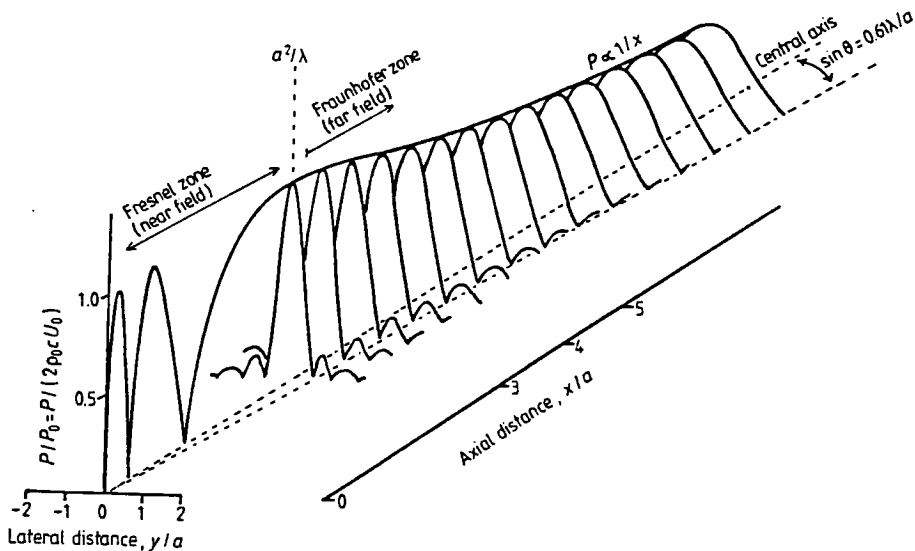


Figure 2.4 Fraunhofer and (on-axis) Fresnel solutions for the pressure amplitude in front of a plane circular source of radius a radiating a continuous sine wave. Adapted from Webb88.

An alternate interpretation of the diffraction field helps in understanding the nature of pulsed acoustic fields. According to this approach, formulated on Young's theory, one can consider the diffraction field to be the result of superimposing just two waves, rather than the infinite number of spherical Huygen's spherical wavelets. The diffraction field is then a result of interference of (i) a wave emerging with identical spatial extent and phase as the radiating aperture, and (ii) a wave spreading out in all directions from the edge of the transducer.

2.2.5 Resolution

Now that the general concepts of the B-Scan have been defined, it is appropriate to consider the question of spatial resolution. There can be no absolute definition of the resolution of ultrasonic imaging systems, since in practice too many variables affect the displayed resolution. Thus a resolution measure, such as the full width at half-maximum (FWHM), which is commonly used in other medical imaging systems, will produce a result that depends on the shape of the response function (system impulse response). Nevertheless, such variations are often ignored. The three-dimensional point spread function of ultrasonic imaging systems may be highly asymmetrical, the equivalent length of the sound pulse usually being smaller than the beam width. Hence it is common to talk about axial and lateral resolution of pulse-echo systems.

A. Axial Resolution

The term refers to resolution along the path of the beam. As the beam travels through the tissue, it encounters many interfaces. Resolution refers to how closely these interfaces can be spaced and still be distinguished as separate objects. Spatial resolution is expressed in terms of separation; the smaller the number, the larger is the resolution. In radiology, resolution is commonly expressed in terms of line pairs per unit distance. Axial resolution depends primarily on pulse length. Figure 2.5 illustrates the physical principle that axial resolution can be no better than half the pulse length. Pulse length is simply the duration of pulse times the speed of sound in the tissue. With an ultrasound speed of 1540 m/sec in tissue, and a pulse duration between 1.5 and 2 μ sec, the pulse length is about 2 mm.

It should be pointed out that, the limiting factor for the axial resolution is the duration of the pulse. This being in the depth (encoding time) direction, the shorter the pulse length, the better is the resolution. Another limit to decreasing pulse length is the broadening of the bandwidth. As the pulse length shortens, the bandwidth broadens.

B. Lateral Resolution

This refers to resolution normal to the axis of the beam (also called side-to-side resolution) i.e. in direction of transducer motion. As the beam sweeps across the tissue, it sees many interfaces located adjacent to each other, at the same depth. The question once again is, how close by can these interfaces be and still be distinguishable?. As illustrated in figure 2.6, lateral resolution depends on beamwidth. If two interfaces are positioned closer

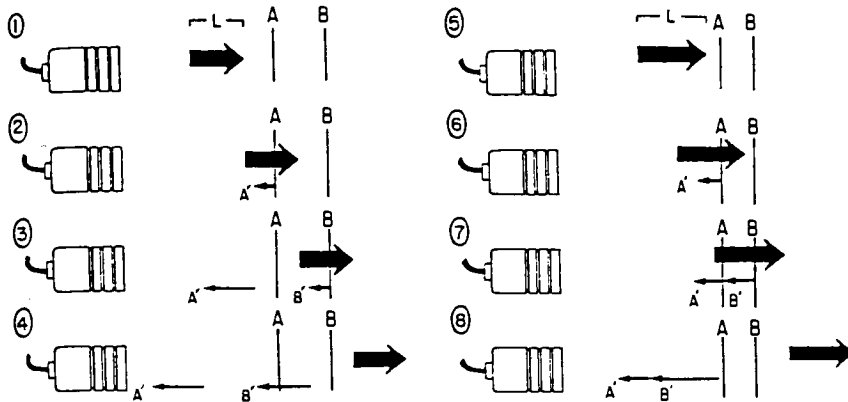


Figure 2.5 Diagram representing effect of pulse length on axial resolution. Lines 1 to 4 show situations in which two interfaces, A and B, are separated by more than half the pulse length, L . Echoes from A and B (A' and B') do not overlap, and transducer sees two separate echoes. Lines 5 to 8 show situations in which A and B are closer than one-half of L . In this case, echoes A' and B' overlap, and transducer sees only a single echo. Adapted from Bartum83.

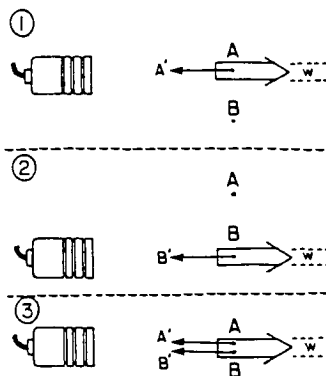


Figure 2.6 Dependence of lateral resolution on beamwidth. If interfaces A and B are separated by more than the beamwidth W , as the transducer is moved across them two separate echoes A' and B' will arrive at the transducer simultaneously and be recorded as a single echo (line 3). Adapted from Bartum83

than the beamwidth, they produce echoes simultaneously and only one echo is received by the transducer. The bandwidth is usually determined by the FWHM (full width at half maximum), but many other levels are in use, e.g. 3, 6 and 10 dB. So in comparing the bandwidths of two transducers, one must know how the beamwidth is defined.

2.2.6 Production of Ultrasound - Transducers

The transducer is probably the single most important component in an ultrasonic imaging system. It acts as the interface between the body being scanned and the instrument electronics used in producing an image. Its function is to convert applied electrical signals to pressure waves, which propagate through the medium, and to replicate the received acoustic waveforms into electrical signals. A good transducer will do this with high fidelity and good conversion efficiency, with minimum introduction of noise and other artefacts. In addition it is primarily through transducer design that one has control over the system resolution, and its spatial variation.

A conventional transducer makes use of the *piezoelectric effect* to generate a voltage, when a certain crystal is placed under compressive stress. Conversely, when an electric voltage is applied to a piezoelectric crystal, it results in a change of shape of the crystal. The tiny expansions and contractions thus caused result in small pressure waves that are transmitted as the ultrasound wave. Similarly the received waveforms cause deformations in the crystal, resulting in small voltages across the electrodes. Quartz, despite being a natural piezoelectric crystal does not perform very well. Thus in medical

ultrasound nearly all the transducers are made of synthetically produced *lead zirconate titanate* (PZT), which is a ceramic, or *polyvinylidene difluoride* (PVDF), a plastic.

A. Vibration and Frequency

In an ultrasonic transducer, the crystal is shocked by a very short pulse of electricity and vibrates or "resonates" at a frequency determined by its thickness. When the size of the transducer is one-half of the wavelength, a resonance is reached and the amplitude of the sound wave produced peaks sharply. The velocity of ultrasound propagation in PZT is 3780 m/sec, which gives a fundamental resonance ($\lambda/2$) at frequency f (MHz) and thickness T (mm) related by

$$T \approx 2/f. \quad (2.10)$$

A 5.0 MHz transducer would have a thickness of 0.38 mm with a wavelength of 0.76 mm in the transducer.

B. Bandwidth

Various factors within a transducer make it emit sound waves over a band of frequencies. Crystal imperfections, non-parallel facets, wave coupling and loading materials are some of these factors, which define the *bandwidth*, Δf , of the transducer. The frequencies are closely grouped around the central (peak) frequency, f_0 , which in the case of figure 2.6 is 2.4 MHz. In case of transducers with broad bandwidths, there may be considerable overlap in the output amplitude spectra and hence little difference in the images they produce. However this is exactly what allows us to pulse our system.

C. Focusing

Focusing of the beam is another important characteristic of a transducer. Non-focussed transducers suffer from a wide beamwidth, which results in poor lateral resolution (typically 2-3 cm). Furthermore, they display severe nonuniformity in the near field, which may extend a fairly long distance into the medium. Therefore most available ultrasound systems make use of focussed beams.

2.3 Principles and Theory of Image Generation

In the previous sections we laid the foundation of ultrasound imaging. So far the physics of ultrasound has been discussed, the knowledge of which is required to understand how the ultrasound pulses interact with the tissues within the human body. This section is for the purpose of highlighting those aspects of ultrasound imaging which distinguish it from other imaging methods.

2.3.1 Pulse-echo Scanning

The conventional technique of ultrasound imaging utilizes a short pulse, for interrogation of the object, thus forming a scan or an image. The echo received from the object is a convolution of the wave field incident on the tissue structure being imaged and an impulse response associated with the scattering properties of the tissue. A two-

dimensional representation of the convolution equation of the otherwise three-dimensional system is given by:

$$g(x,y) = h_1(y) * h_2(x) * f(x,y) \quad (2.11)$$

where $g(x,y)$ is the image before envelope detection, $h_1(y)$ is the axial pulse-echo impulse response of the system (RF pulse shape), $h_2(x)$ is the lateral pulse-echo impulse response (beam profile) and $f(x,y)$ is the backscattering impulse response of the tissue.

A considerable amount of signal processing may be applied to $g(x,y)$ before it is displayed, so that the point spread function (PSF) is the impulse response of the imaging system. Major differences with other areas of imaging occur in that [Webb88]:

- (a) the processing is non-linear;
- (b) the PSF is spatially variant (radiation field pattern);
- (c) the PSF depends upon the object (speed, attenuation and scattering);
- (d) the radiation is coherent and the detector is phase-sensitive
(results in interference between different parts of the image);
- (e) the PSF has, and therefore so will the image have, negative contributions;
- (f) the PSF is not circularly symmetric (in case of inhomogeneity); and
- (g) the PSF is not separable (especially in the near field), although it is often assumed to be.

Equation §2.11 makes many assumptions, including uniform speed of sound, no attenuation, no multiple scattering, no system noise, and PSF spatially invariant but separable into axial and lateral contributions.

If $f(x,y)$ is an impulse (i.e. a single point scatterer) then the image $g(x,y)$ recorded is the PSF of the system. The image is formed by a B-Scan (as previously described) of the impulse. Each scan line is formed as a convolution of the input pulse with the impulse (with a lateral and axial shift), which is then envelope detected and converted to a gray scale image on the monitor, as shown in figure 2.7 [adapted from Webb88]. More usually we have multiple scatterers, which could be positioned extremely close to each other. As shown in figure 2.8, these multiple scatterers interfere with each other, and the image hence formed does not resolve these points. This interference causes a speckle pattern to build up, which is discussed later.

The really difficult part in the model of ultrasonic image formation is that no one really knows exactly what the tissue backscattering impulse response should look like. Various models exist for this purpose, and the most common one models tissue as a random distribution of point scatterers of a given scatterer number density. Another alternative technique has been to consider that the density and elastic modulus vary continuously in the object.

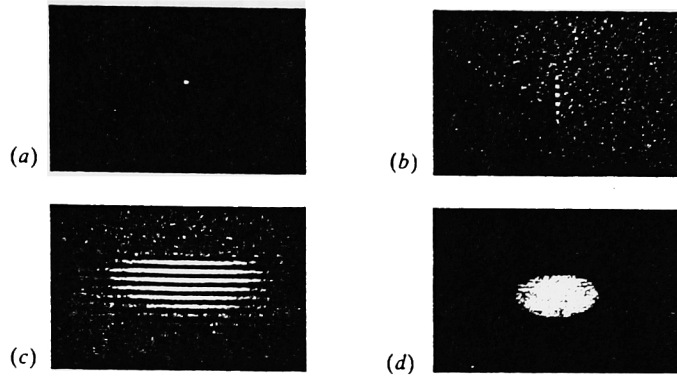


Figure 2.7 Use of a digital simulation (Bamber80) illustrate the two stages of convolution, first with the RF pulse (b) and then with the beam profile (c), followed by envelope detection, leading to an image (d) of a single point (a). Adapted from Webb88.

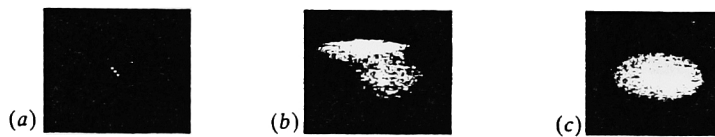


Figure 2.8 Use of the same imaging model as in figure 2.7 to illustrate the generation of artefactual detail, or speckle, (b) from coherent interference between waves from closely spaced scatterers (a) Image (c) simulates the blurring produced by an incoherent imaging system with the same PSF. It shows no artefactual fine detail. Adapted from Webb88.

2.3.2 Speckle

A speckle pattern is formed from the interference of a coherent source with a randomly distributed (rough) surface. The interaction of the wave with the random surface results in various constructive and destructive interference patterns, which form the speckle pattern, consisting of bright and dark spots. The appearance of speckle takes place in imagery with reflection as well as transmission. In the case of acoustic imagery, the interrogating ultrasound pulse interacts with the tissue (which consists of randomly distributed impulses), which leads to the characteristic speckled effect in ultrasound images and, contributes a form of visual noise or clutter. The topic of ultrasound speckle is a vast one, and interested readers can refer to Green⁷⁴, Wagner⁸³ and Burckhardt⁷⁸ for further detail.

The reduction of speckle noise in ultrasound images can be attained to a certain degree by compound scanning, which in effect is an averaging of the same object image with different parameters [Goodman⁷⁶]. The same object can be scanned with varying frequencies or position, and then averaged to improve image contrast, and hence decrease speckle noise.

Chapter 3

Experimental Approach

This chapter includes all the simulation work, experimental setups and procedures that were used during the research and data collection. Due to the large amount of equipment used, and the limitation of this thesis, it would not be possible to describe the intricate working of each electronic component. However all the black boxes will be briefly discussed in the Appendices.

3.1 Imaging Scheme with Frequency Modulated Pulse

Up until this point all the theory and principles behind ultrasound imaging have been discussed for the case of conventional short pulse. The reason for this simply being that, the physics of the frequency modulated (FM) pulse does not change from that of the short pulse. The interaction of the FM pulse with the internal structures remains the same,

the only difference being in the representation of the information. The post-processing step performed after the backscattered signal has been collected is of grave importance for the success of this technique.

The motivation for this study into a new technique for ultrasound imaging stems from the following dilemma. There is now increasing theoretical and experimental evidence that ultrasound used at intensities employed clinically, can produce effects which have characteristics of transient cavitation³. Prolonged cavitation is potentially damaging. It can destroy cells locally and induce chemical changes through free radical production [Riesz85]. Low temporal average intensity pulsed ultrasound, equivalent to that used in diagnosis, has been shown to cause deleterious effects in lower organisms [Cartestensen87]. Even though it is difficult to extrapolate these observations to human in-vivo studies, a hypothetical risk exists at the present time. For this reason the Frequency Modulated pulse was studied, and was applied to the experiments, in order to do imaging. The results obtained were fairly satisfactory.

Current diagnostic units use short (1-5 μ s) interrogating pulses for imaging. Often the peak intensities of these short pulses are 10 to 60 times higher than the calculated and observed threshold values for cavitation in aqueous media [Crum86, Flynn32 and Carson78]. Within the framework of short pulses, it is not possible to reduce the peak intensity without sacrificing signal to noise ratio. So, although bringing down the peak

³ Cavitation : In case there are micron-sized air bubbles present in the body during investigation the following problems could occur. Within one cycle of the short, high intensity pulse, the micron-sized bubble could adiabatically collapse, producing high temperatures in the order of 10^4 °K. This would result in chemical changes through free radical production, causing unnecessary side effects.

intensity below the threshold will reduce the risks of cavitation, it will lead to the reduction of diagnostic information, which in turn could lead to a possible risks of mis-diagnosis.

So with the intent of not losing out on diagnostic information, and at the same time reducing the possibility of cavitation, the FM pulse was studied. The usefulness of the technique stems from the fact that transient cavitation is characterized by sharply defined peak pressure or intensity thresholds. The cornerstone of this new system is a technique known as *pulse compression* [Klauder60]. By compressing a very long duration (20-50 μ s) frequency modulated pulse with low peak intensity into a short pulse with very high peak intensity, we can obtain backscattered signal comparable in strength to the signal obtained from conventional short pulse. Similar techniques using pseudo random code have been used in non-destructive testing [Elias80] and acoustic microscopy [Nikoonahad89].

3.1.1 Pulse Compression Processing

The real usefulness of this technique in medical imaging, comes from the fact that the process of pulse compression, which is carried out on the received backscattered signal (Figure 3.1 shows where the post-processing step is incorporated), eliminates the need of subjecting the body to high intensity pulses. Contrary to the conventional short pulse, which has high intensity and short duration, the FM has a much lower intensity and lasts over a longer period of time.

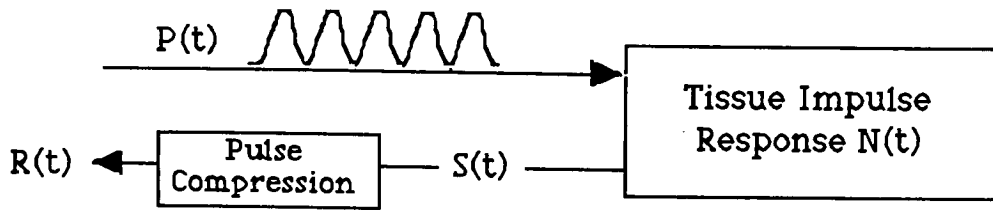


Figure 3.1 Post-processing step of pulse compression

$P(t)$ is the input FM pulse and $N(t)$ represents the tissue impulse response. For a non-attenuating medium, $N(t)$ is simply a sum of delta functions, $\sum_i A_i \delta(t-t_i)$ where A_i is the reflection coefficient of the i^{th} scatterer which is located at a distance $z_i = c \cdot t_i / 2$, c being the speed of sound in water (1540 m/sec) and t is the two-way travel time. Treating the pulse propagation and reflection as a linear process, the backscattered signal $S(t)$ can be expressed as a convolution of $P(t)$ with $N(t)$:

$$S(t) = P(t) * N(t) \quad (3.1)$$

$$R(t) = P(t) * S(t) = P(t) * P(t) * N(t) = [\text{Autocorrelation of } P(t)] * N(t) \quad (3.2)$$

The process of pulse compression is carried out by correlating the input FM pulse $P(t)$ with the backscattered signal $S(t)$ as shown in the equation §3.2. This post-processing step results in an effective autocorrelation of the input FM pulse $P(t)$, which is a compressed short pulse whose peak amplitude is greater than the peak amplitude of the FM pulse by a factor K . This gain factor K is the product of the time duration and the effective

bandwidth⁴ of the FM pulse. Also known as the time-bandwidth product, this factor K is the theoretically attainable signal-to-noise enhancement. Utilization of this technique can result in a real reduction in the peak amplitude of the FM pulse by a factor of \sqrt{K} compared to the short conventional pulse, under the constraint that the signal-to-noise after the pulse compression process be the same in the two cases.

3.1.2 The Three-dimensional Point Spread Function

(A) Non-Attenuating Medium

The process described above in the Pulse Compression section, would produce a single A-line signal which is one-dimensional in nature. Time t encodes the depth coordinate z . By moving the transducer to an adjacent location, and displaying all A-lines together, one generates a two dimensional image. Although the A-line signal represents a one-dimensional image of the object, it should not be forgotten that physical phenomenon take place in "real space", known to be three-dimensional. The tissues and their echo generating structures have a spatial extent and no transducer can exactly focus the ultrasound beam on a line or a plane. This is why the impulse response characterizing an echo graphing system should have a 3-D spatial dependence on the target position. The 3-D point spread function is defined as follows: any point in space is referenced in a Cartesian system of coordinates (O_x, O_y, O_z) ; a transducer can be moved in a plane

⁴ The width at 50% location in the transfer function (bell shaped) of FM pulse .

(O_x, O_y) while keeping its axis parallel to the O_z axis which also the same as the transducer beam axis (and measures the depth, and time in medium); a target location is determined by coordinates (x_0, y_0, z_0) . The contribution of this target to the 3-D image is the value of the target response at time $2z_0/c$ when the transducer is located at $(x=0, y=0, z=0)$.

For a circularly symmetric transducer, similar to the one used in the experiments for this thesis, the backscattered RF signal from a target at (x_0, y_0, z_0) can be written as

$$A(r, t) = C \bullet P(t) * B(r, t, z_0) ; t = 2z_0/c \quad (3.3)$$

where r is the radial distance of the target from the central axis of the beam $[r = \sqrt{(X-x_0)^2 + (Y-y_0)^2 + z_0^2}]$, $P(t)$ is the FM pulse response at $r = 0$, and C is a constant that depends on scattering strength. $B(r, t, z_0)$ describes the beam response of the system at depth z_0 . Clearly $B(r, t, z_0)$ is not shift-invariant since it depends on the position of the reflector. But if we assume that $B(r, t, z_0)$ does not change appreciably in a small range around z_0 then the effect of the beam can be modelled as a convolution process, with respect to time t . The PSF of the FM pulse imaging scheme is determined after pulse compression processing i.e. after cross correlation of $A(r, t)$ with $P(t)$;

$$PSF(r, t) = C \cdot P(t) \bullet P(t) * B(r, t, z_0) \quad (3.4)$$

where \bullet stands for crosscorrelation process. For two-dimensional B-scan imaging, scanning is done along a plane, say x - z plane. The two-dimensional point spread function PSFN for a scatterer at z_0 in a non-attenuating medium can be written as:

$$\text{PSFN}(x,t,z_0) = C \cdot \{P(t) \bullet P(t)\} * B(x,t,z_0) \quad (3.5)$$

where time t encodes the z dependence. The only difference here from the conventional imaging scheme is that the short pulse has been replaced by the autocorrelation of the FM pulse $P(t)$. The advantages of such an imaging scheme are two fold: (i) for a given total energy of the input interrogating pulse, a higher signal-to-noise ratio can be achieved [Rao88,Rao90]; and (ii) the point spread function can be changed easily by changing the pulse parameters of the FM pulse. From equation §3.5, the resolution in the axial (i.e. z) direction depends on the pulse width of the compressed (autocorrelated) FM pulse. This can be controlled by the bandwidth Δf of the frequency sweep. For a narrow bandwidth excitation, $B(x,t,z_0)$ can be approximated by $\delta(t-2z_0/c) \cdot B(x,z_0)$, where $B(x,z_0)$ is simply the diffraction pattern at depth z_0 due to a circular transducer. At least in the far field approximation, $B(x,z_0)$ depends on the center frequency of excitation, f_0 , which can also be controlled easily in the input FM pulse [Arditi81]. A Fourier approach can be used to exactly calculate the diffraction impulse response $B(x,t,z_0)$ [Guyomar87]. The ability to vary the point spread function may prove to be of practical value in problems dealing with (a) speckle reduction via averaging of independent speckle patterns [Melton84] and (b) tissue characterization using random RF signal or envelope detected data [Rao89, Rao91], both of which have been discussed in the chapter dealing with applications of FM pulse.

(B) Attenuating Medium

In order to image in a frequency dependent attenuating medium, such as soft tissue, the point spread function described in equation §3.5 is further modified. Assuming attenuation coefficient is linear with frequency, $\alpha(f) = \alpha_0 \cdot f$, and medium is non-dispersive, so that phase and group velocities c become equal and independent of frequency f , impulse response for round trip travel to a reflector at depth z_0 can be evaluated as follows.

The transfer function for round trip propagation to a reflector at depth z_0 is given by [Kak78].

$$H(f) = A \cdot \exp[-\alpha(f) \cdot 2z_0] \cdot \exp[-i2\pi f 2z_0/c] \quad (3.6)$$

where A is the reflection coefficient. By taking the Inverse Fourier Transform of $H(f)$, we obtain the impulse response $h(t)$ (See Appendix A for solution).

$$h(t, z_0, \alpha_0) = \frac{A}{\pi} \frac{(\alpha_0 z_0 / \pi)}{[(\alpha_0 z_0 / \pi)^2 + (t - 2z_0/c)^2]} \quad (3.7)$$

Assuming linearity and shift invariant property in a small region around z_0 , effect of attenuation can be incorporated as a convolution process. The point spread function in an attenuating medium, PSFA, then becomes

$$\text{PSFA}(x, t, z_0, \alpha_0) = C \cdot \{P(t) \bullet P(t)\} * B(x, t, z_0) * h(t, z_0, \alpha_0) \quad (3.8)$$

The point spread functions described by equations §3.5 and §3.8 for non-attenuating and attenuating medium respectively, refer to the backscattered RF signal and not the usual envelope detected B-mode imaging. The envelope detection process is non-linear, and therefore cannot be represented as a convolution process. However, we can approximately write the envelope detected PSF as a product of two functions, one is the envelope detected compressed pulse describing the shape of the PSF along the axial or z direction and the other is the beam profile function describing the PSF along the lateral or x direction.

3.2 Effects of Attenuation : A Computer Simulation

As it has already been reiterated several times in this thesis, ultrasonic attenuation is frequency dependent. Therefore the spectrum of the FM pulse reflected from an interface at a certain depth will be different from the spectrum of the input interrogating FM pulse with which it will be correlated. A reduction in correlation can lead to a reduction in the time-bandwidth product (K). This reduction was studied by performing a simulation of the propagation effects in an attenuating medium. A discussion of this study is provided in this section. Simulations were carried out on the ASYSTANT® software package on a PC.

Earlier sections have established the impulse response $h(t)$ of the system in an attenuating medium, given by equation §3.8. It should be pointed out that even though $h(t)$ is non causal, it correctly accounts for the modification of the amplitude spectrum of the input pulse due to propagation. $h(t)$ replaces a delta function, $\delta(t-2z_0/c)$ in the case of non-

attenuating model. The signal $S(t)$, backscattered from an attenuating medium with reflectors at various depths z_i can be modeled as:

$$S(t) = [P(t) * \sum_i hz_i(t)] \quad (3.9)$$

where $P(t)$ is the input FM pulse. If so desired a time gain correction (TGC) function can be incorporated to this equation by multiplying $S(t)$ with $G(t) = \exp(\alpha_0 g t)$ where g is an adjustable parameter. However, for the purpose of this thesis, it was not required to perform a TGC since we were interested in actually observing how the attenuating medium effected the backscattered signal. TGC is useful in applications where one is interested in gaining information equally, from all objects sitting within the field-of-view. Also, the exact function for TGC is required to obtain an accurate representation of the hidden objects.

Simulations were performed with FM pulse of 12.8 μ s duration. The center frequency and bandwidth could be varied (For details see Appendix B). Figure 3.2(a) shows 5 reflectors located at 2,4,6,8 & 10 cm depth in a medium with $\alpha_0 = 0.15$ dB/cm/MHz (0.01725 Np/cm/MHz)⁵. This attenuation coefficient was chosen, since it was the same α_0 as that for the attenuating medium on which experiments would be performed. The input FM pulse had a central frequency $f_0 = 4.00$ MHz and a gaussian modulated FWHM bandwidth $\Delta f = 2.12$ MHz, this pulse is shown in figure 3.2(b). Figure 3.2(c) is

⁵ Note that 1 Np/cm/MHz = 8.686 dB/cm/MHz

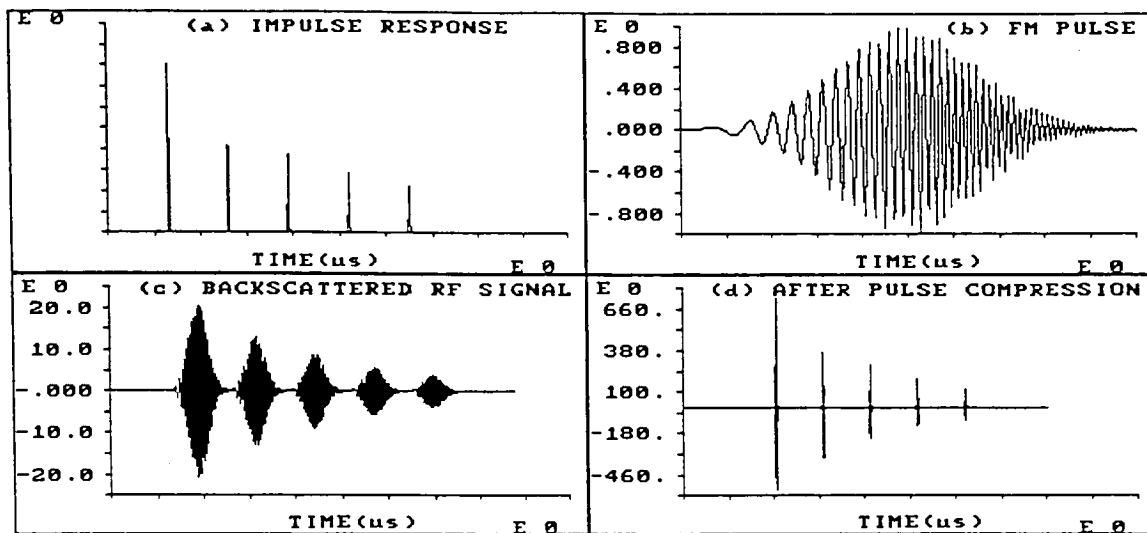


Figure 3.2 (a)-(d) Simulation of frequency dependent attenuation of the medium in the FM pulse imaging process.

the backscattered RF signal. The process of cross-correlation with the input pulse is carried out on this backscattered signal and the result is shown in figure 3.2(d).

As it can be clearly interpreted from the figures above, the intensity of the signal is considerably reduced as we move deeper into the attenuating medium. The factor to be compared in these cases, as we move deeper into the medium is the time-bandwidth product K . It can be calculated, by evaluating the energy in the Fourier Transform of the autocorrelation of the FM pulse with maximum amplitude normalized to unity. For example, the input FM pulse is shown in figure 3.2(b) and its time-bandwidth product K is estimated to be 16.134. Figure 3.3(a) and (b) below show the comparisons of the backscattered RF signals from depths of 2, 6 and 10 cm for a medium of $\alpha_0 = 0.15$ dB/cm/MHz (0.01725 Np/cm/MHz) at $\Delta f = 0.5$ and 2.0 MHz respectively.

For these figures, appropriate gain correction was applied to normalize the peak amplitude to 1 cm in each case. We can clearly observe the loss of high frequencies as we go deeper into the medium from 2 to 10 cm. This loss can also be seen in figure 3.4(a) and (b) which are the amplitude spectrum of the pulse in figure 3.3(a) and (c) respectively. Further, the effective time-bandwidth product for a pulse reflected from a certain depth was calculated from the energy in the Fourier transform of the function obtained by crosscorrelating the input FM pulse with the reflected pulse from that depth. The results are shown in figure 3.3(d). As expected, for 2 cm depth K is close to 16, the value we expect for non-attenuating case. This is because the change in the spectrum of the reflected FM pulse from the spectrum of the input FM pulse is small (figure 3.4(a)). But for reflectors at increasing depths, we notice a gradual decrease in the time-bandwidth product, dropping down to 13.7 for 10 cm depth.

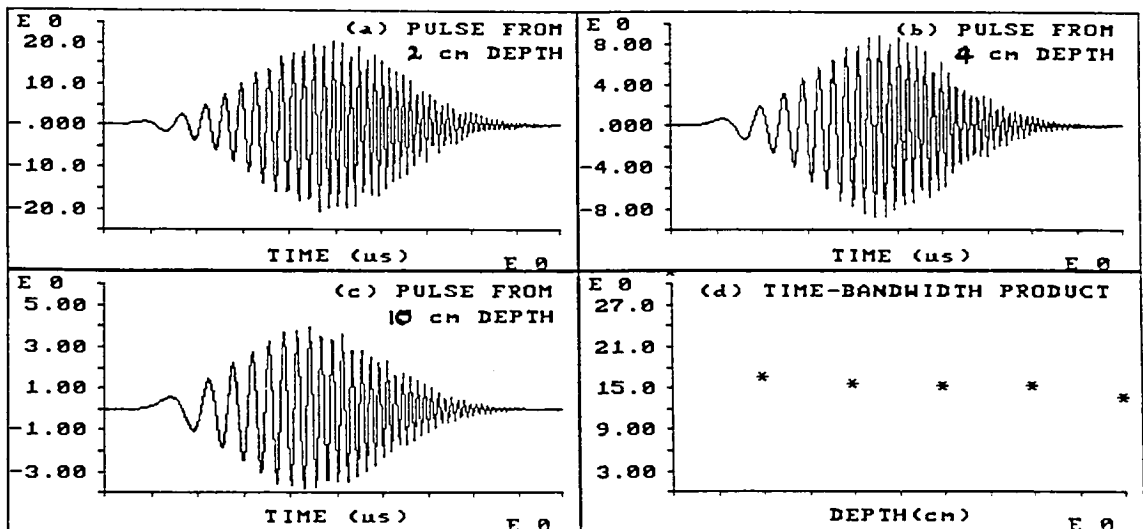


Figure 3.3 shows the backscattered RF signals from various depths (a) 2 cm, (b) 6 cm, (c) 10 cm. (d) is a plot of the time-bandwidth product as a factor of depth.

Additional simulation work was performed, to show the variation in the time-bandwidth product, as we went deeper into the medium. This was done for several central frequencies f_0 and for bandwidths Δf of 0.5 and 2.0 MHz. The results are shown in figure 3.5 (a) and (b). In these figures the y-axis represents \sqrt{K}

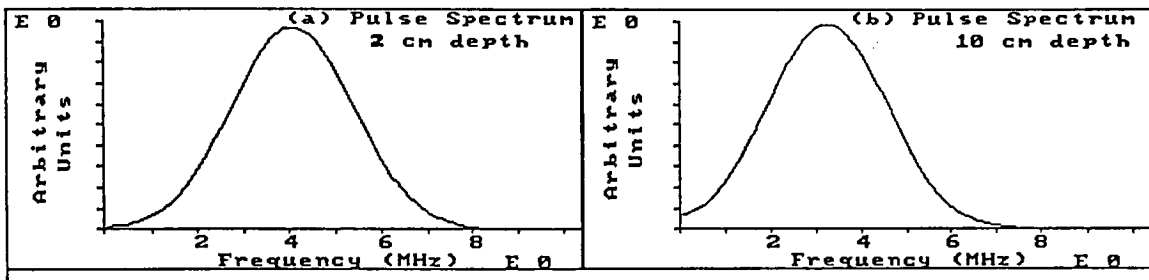


Figure 3.4 (a)-(b) shows the pulse spectrum for signal reflected from 2cm and 10cm respectively.

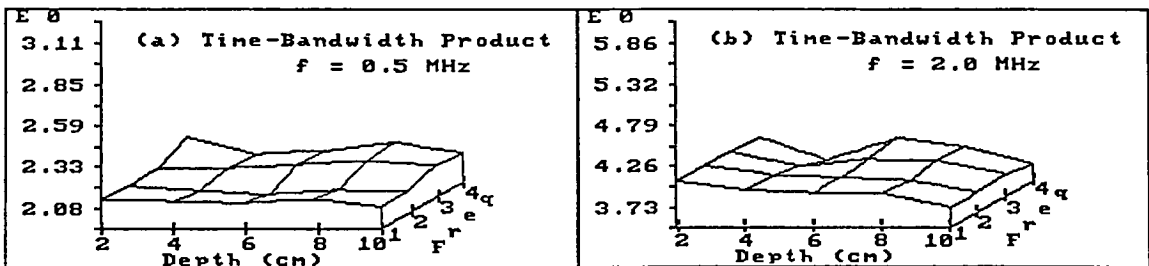


Figure 3.5 Time-bandwidth product as a function of center frequency f_0 and depth z , for attenuating medium of $\alpha_0 = 0.01725$ Np/cm/MHz (a) $\Delta f = 0.5$ MHz, (b) $\Delta f = 2.0$ MHz.

3.3 Experimental Setu

Once the simulations were complete and satisfactory results were obtained, we were ready to implement the theory into experiments. These experiments would give us an insight as to what actually takes place when the FM pulse interacts with soft tissue. For this purpose we used two types of phantoms[Milne83]. Both had exactly the same structure, and their steel wire targets were placed at exactly the same positions within them. The only difference was the medium within the phantoms, one being filled with water (non-attenuating) and the other with a gelatinous material of attenuation coefficient $\alpha_0 = 0.15$ dB/cm/MHz (0.01727 Np/cm/MHz). The details of the material used are beyond the scope of this thesis. This chapter describes all the procedures that were followed in order to obtain the final B-scan images.

Since all the equipment used in the experimental setup was opened by the author fresh from all its packing, it needed to be closely examined and calibrated where necessary. Some of the pre-experimental work has been captured into the Appendices, and will be referenced when need be.

The experimental setup used for this thesis is depicted in figure 3.6 as a flow chart, and figure 3.7 shows a photograph of the laboratory setup of all the instrumentation. An Analogic Corporation *Polynomial Waveform Generator* (PWG) was programmed to generate a linearly swept frequency modulated pulse (see Appendix C), $P(t)$:

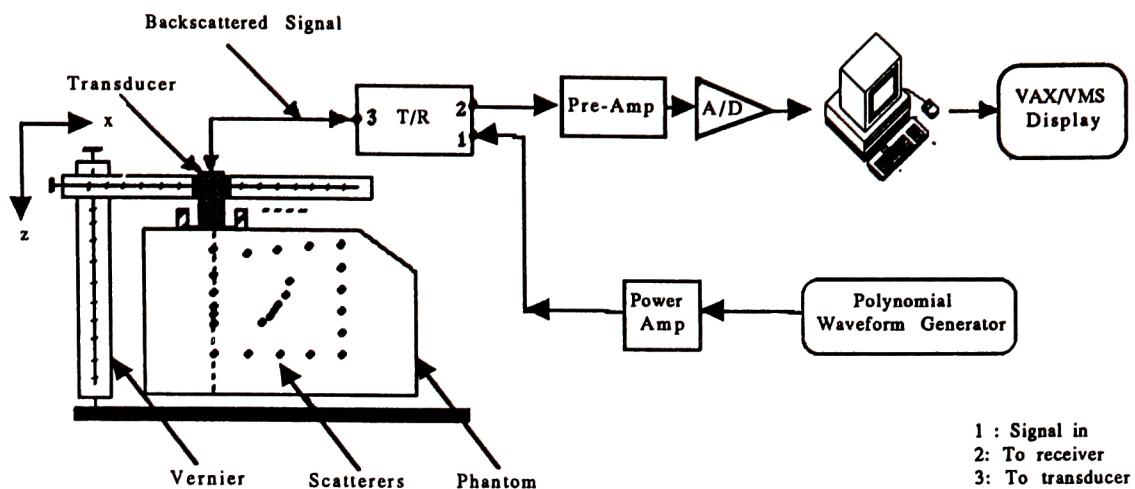


Figure 3.6 Block diagram of experimental setup used.

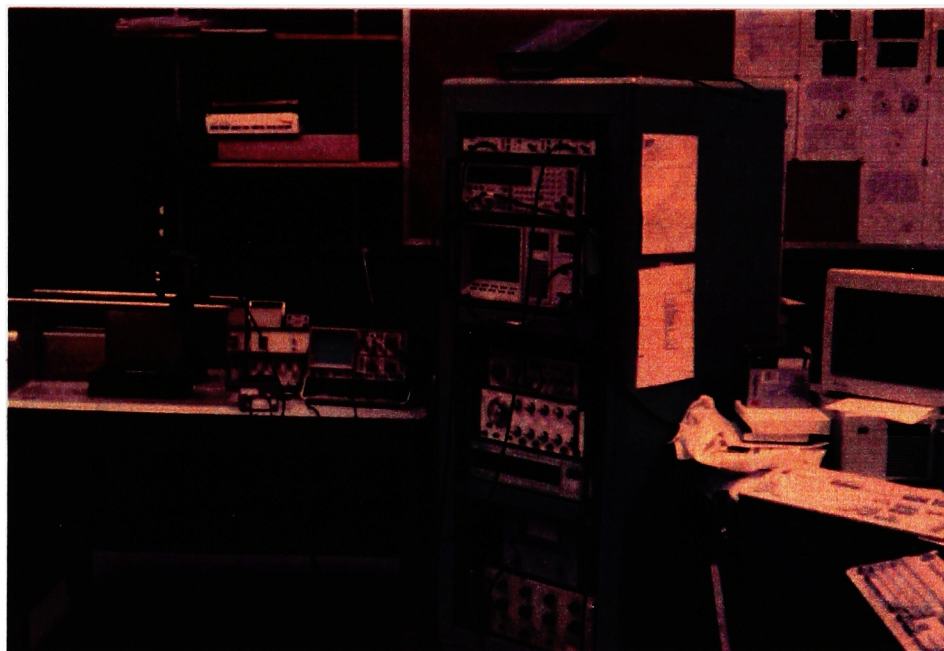


Figure 3.7 Instruments used in the experimental setup

$$P(t) = \frac{1}{2} \cdot \left[1 - \cos\left(\frac{t}{T_0}\right) \right] \times \left[\sin\left\{ \underbrace{f_0 - (1.042 \cdot (\Delta f + 0.068))}_{A} \cdot t + \underbrace{\frac{(f_0 - 0.068)}{0.982 \cdot T_0}}_{K} \cdot t^2 \right\} \right] \quad (3.10)$$

where T_0 is the time duration of the pulse which was kept constant at 20 μ s. f_0 and Δf are the center frequency and 6 dB bandwidth in MHz. These two parameters can be set independently. The first term of the right hand side of the equation is the Hanning weighting applied to the pulse amplitude, in order to give it a modulated envelope. The argument of the sinusoid has two terms, the first one "A" defines the starting frequency and the second term "K" increases the frequency linearly with time. The constants of the equation were determined empirically so as to match the expected spectrum of the pulse for several values of f_0 and Δf (for details see Appendix C). This equation is stored as F204 in the PWG memory.

Once the output from the PWG was satisfactory, it was sent to a *power amplifier* to increase the strength of the interrogation signal. The instrument, functioning at 50 dB for signals ranging from 20 KHz - 10 MHz, gave an amplification factor of 316.2 to the input signal. This amplified signal, which had considerable strength, was sent to the transducer via a *T/R* (Transmitter-Receiver) circuit [Follett 76]. The T/R circuit is a device that was built (i) to act as a switch for the transducer to perform in the transmitter or the receiver mode, and (ii) to protect the instruments from any damage due to high intensity transmitter pulse (see Appendix D for modified circuit). As shown in figure 3.6 the T/R circuit has three connectors, 1: signal in, 2: to receiver and 3: to transducer. The signal from the power amplifier enters the circuit from connector 1. It is then forwarded to the transducer through

connector 3, which in turn transmits the pulse and receives the backscattered signal. This backscattered signal, or *echo* enters the circuit from 3 and leaves through connector 2 which carries it to the receiver.

The *transducer* used here was a *Panametric* unfocussed piezoelectric circular disk transducer. It had a diameter of 1.27 cm, a center frequency of 2.4 MHz and a 6dB bandwidth of ~ 2 MHz. To calculate the above figures, the transfer function of the transducer was evaluated using a hydrophone⁶, by measuring its response to sinusoidal waves of a range of frequencies. Figure 3.8 shows the transducer transfer function (for table refer to Appendix E).

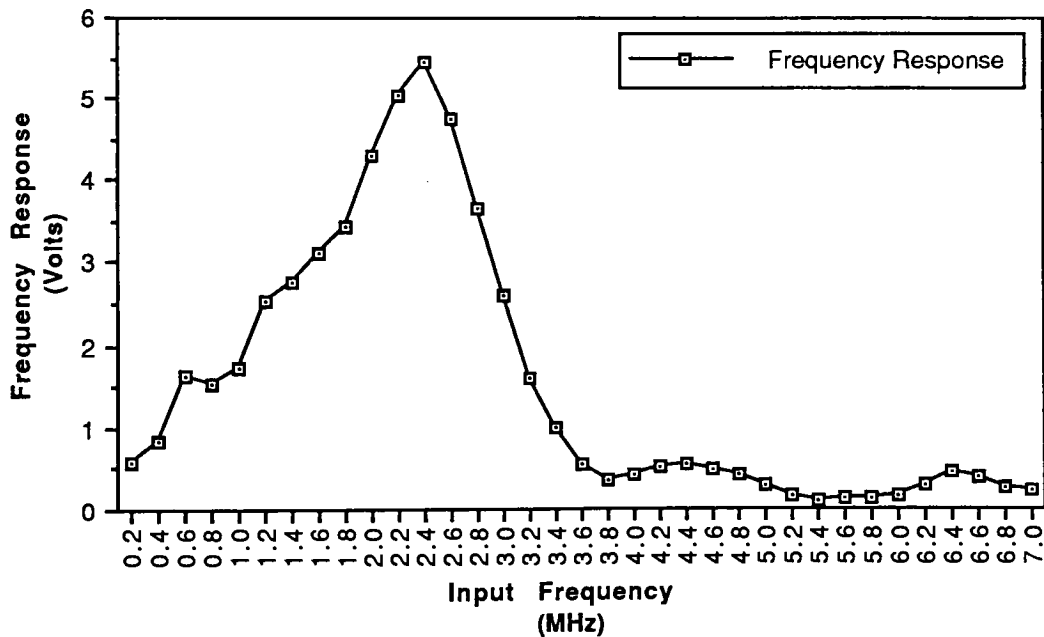


Figure 3.8 Transducer transfer function, evaluated using a hydrophone.

⁶ A device that converts acoustic signals to electronic pulses.

The echo from the phantom is received by a *pulse receiver* connected at junction 2 of the T/R circuit. Here we pass the signal through a high-pass filter of 0.3 MHz, in order to get rid of some low frequency signal over which the entire backscattered signal seemed to be riding. This was probably due to the impedance mismatching of the various instruments used, in conjunction with the transducer.

Next we go to a *pre-amplifier* in order to boost our backscattered signal, which is quite small as compared to the input pulse. The pre-amp is another one of the instruments that had to be calibrated. Appendix F shows a table which was generated to determine the amplification that each scale in the Analogic Corporation Dual Pre-Amp corresponded to. This was once again done by using a constant input and recording the value of the output signal, for every scale. Typical amplification factor used during the data collection was 19.

Now that the signal had attained a considerable amount of amplitude, which was enough to be distinguished by the oscilloscope, we needed to record it. We also required to digitize this analog signal, to be able to generate gray scale B-scan images. At this stage we introduced a Analogic Corporation Data 6000 waveform processor (see Appendix G for details). This device was used to display, digitize, record and post-process the backscattered signal. Figure 3.9 and 3.10 show the single A-line RF(radio frequency) signal that was seen on the display window of Data 6000 for attenuating medium. The horizontal axis is time t which encodes the depth z . The phantom used, had 5 targets, the distance between them decreasing from left to right as 15mm, 10mm, 5mm and 3mm. The top trace is the recorded RF signal from the phantom targets in response to the transmitted FM pulse which is shown in the middle. The bottom trace is the signal after

crosscorrelation processing. The ordinate trace is not the same for all three traces, but instead has been adjusted for the observer. The longer duration reflected pulse is compressed into a short pulse after crosscorrelation, and all the scatterers can be resolved. Of course this only demonstrates resolution in the axial direction. Although not shown here the resolution for the attenuating case is slightly worse than that for the non-attenuating. This is because of the loss of higher frequencies as the pulse propagates in the frequency dependent attenuating medium. Not all of the digitized points have been displayed due to display size limitations. Therefore any apparent aliasing effect is only due to display limitation and is not a real effect.

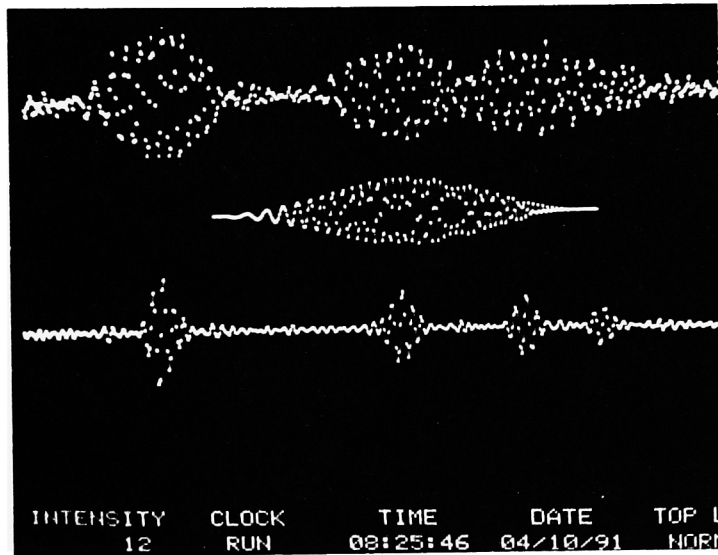


Figure 3.9 Data6000 processing in Attenuating Medium

3.5 Procedure

Now that the basis of data collection has been described we can move onto the description of the procedure that was used. This section will describe how the data collection was conducted, and what data was recorded in order to do the analysis of the FM pulse imaging in attenuating medium.

The PWG was used to generate the FM pulse F204.(Appendix C) The parameters of this equation were set at $f_o = 2.4$ MHz (to correspond to the maximum response of the transducer) and $\Delta f = 1$ & 2MHz. The time duration T_o of the FM pulse was fixed at 20 μ s. This pulse was used to drive an unfocused PZT transducer with a maximum response at 2.4MHz frequency (figure 3.8). The diameter of the transducer was 1.27cm. The interrogation was carried out for non-attenuating as well as attenuating medium, using a phantom. The region of the phantom that was studied had 6 targets in the z direction (depth encoding time) with a separation of 2cm between each one of them. In the x direction the transducer was moved over 28mm (14 on right and 13 on left of center), with iterations of 1mm. The setup used for moving the transducer, comprised of a vernier with 3 degrees of freedom (x, y and z axis) and a rod with the transducer tightly clamped on it. Figure 3.10 shows the phantom used for imaging and specifies the axis.

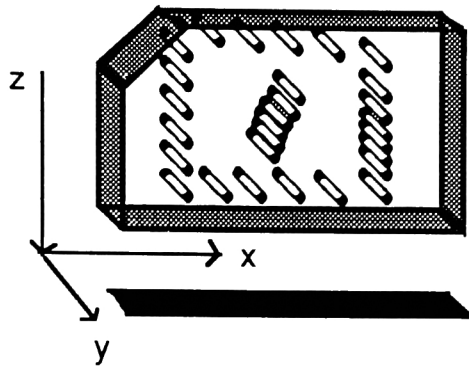


Figure 3.10 The phantom with targets and axis shown.

Due to this crude setup of the transducer, its motion in the x direction was not smooth. A coupling gel was used between the surface of the transducer and the phantom. This made sure of the contact but did little to reduce the drag in the transverse motion. For most part, it was impossible to get an exact perpendicular scan (using the above setup). Therefore the images shown later in the results do not have their peaks for the scatterers along the central scan line, but are shifted of-axis to the right. It should be pointed out that this of-axis shift increased as we went deeper into the medium. However it could not be concluded whether this shift was only due to the drag in the transducer motion, or maybe because the diaphragm of the transducer was at a slight angle. This artefact was unavoidable and was therefore ignored.

The backscattered signal from the phantom was recorded on the Data 6000 waveform processor. As mentioned earlier we took 28 A-line scans, each one of which

comprised of 8192 data points at a sampling rate of 50 MHz (period = 20 ns)⁷. This allowed us to look at 163.84 μ s length of data. A delay of 37 μ s was incorporated, in order to cut off the input FM pulse; also the first scatterer echo, which got scrambled with the input signal, due to its closeness to the surface of the phantom (1.1cm) had to be eliminated. By doing this we also reduced the dynamic range, thus giving us a better look at the much smaller amplitude RF signal (which was in mVolts as compared to the amplitude of the input FM pulse which was in Volts). Using the speed of sound through the medium as 1540 m/s, we could see that it travels 1cm into the medium in 13 μ s (two-way). This means that we could see approximately 12.6 cm deep into the phantom.

For the benefit of the reader, if sampling rate is T, then $1/T = 2f_c$, where $2f_c$ is the Nyquist window. In our case $T = 20$ ns, therefore $2f_c = 50$ MHz. Aliasing occurs if $T > 1/2f_c$. Our maximum frequency never exceeds 7 MHz, thus $1/2f_c = 0.071 \mu$ s, which is > 20 ns (T). And therefore our signal is well sampled.

Each A-line RF signal of 8192 points was stored in a separate file (thus we had 28 files, for each set). For the purpose of display, and that of post-processing we needed to shorten the size of our scan lines. This was done in order to make the system more efficient (8192 point scans took a lot of computation time on the Data6000, and during conversion; along with that we did not have display capabilities for a 8192 point scan.). So, it was decided that we would pick out blocks of 512 points (10.24 μ s) where the scatterer was positioned in the RF signal. Further instead of looking at all 5 scatterers (leaving out the

⁷ Much higher than the minimum requirement from the sampling theorem.

first, which was cut out using a delay), we decided to observe only three. We chose to evaluate scatterers at 3.1cm(2nd), 5.1cm(3rd) and 9.1cm(5th) depths, because they would include the near field (3.1cm), the far field (9.1cm) and the transition (5.1cm) stages of the wave propagation. Figure 3.11 shows the A-line signals, as were seen and recorded, for (a) non-attenuating medium and (b) attenuating medium.

Digressing a bit, it should be pointed out that the input FM pulse was being fed into the Data6000, in parallel with the rest of the circuit (Power-amp, followed by T/R etc.). Thus the FM pulse was also digitized and stored, to perform the post-processing step of crosscorrelation later on. This signal was also sampled at 50MHz, but only for a length of 1024 (20.48 μ s).

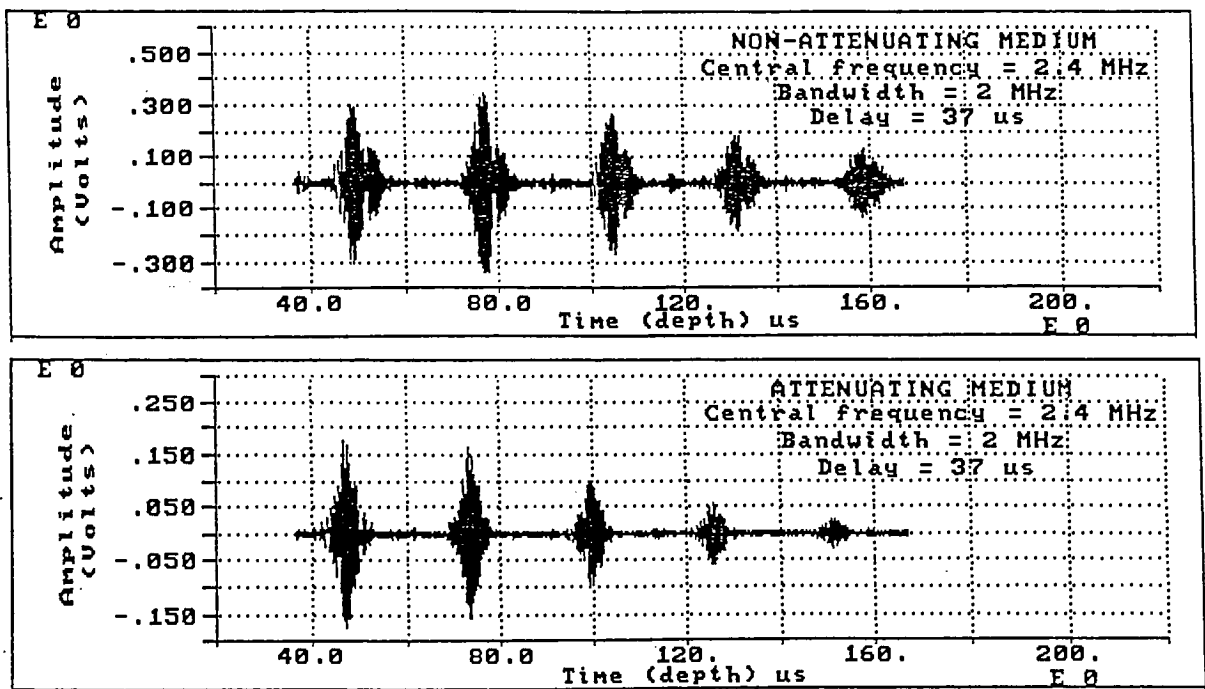


Figure 3.11 RF signal along center scan for (a) non-attenuating and (b) attenuating medium.

The way that the size reduction from 8192 points was carried out was somewhat complicated. Due to the limitations of Data6000, we could not simply pull out one desired chunk of 512 points from the entire signal. This was incorporated in the crosscorrelation step. In order to crosscorrelate the RF signal with the input FM pulse, the order was very important. The former one had to be placed in Trace 1 (top) and the latter in Trace 2. Then while the correlation parameters were being entered, one had to put the *evaluation length* as 512, and the *offset*⁸ as -256. Thus during the step of crosscorrelation, we further reduced the size of each block to 512 points (evaluation length).

The crosscorrelation was also carried out with the 5th scatterer RF signal (in place of the FM pulse) to observe differences. For this purpose, the RF signal that had been stored from the central scan, was recalled into the Data6000 buffer memory. A section of 1024 points (20.48 μ s) was chosen, which consisted of the signal from the 5th scatterer, and was put in Trace 2. The steps, and programs that were used for performing crosscorrelation with FM pulse were carried out using this alternate signal.

Next, the crosscorrelated data was envelope detected using a triangular convolution kernel of width 32 points. This smooth signal was then stored onto floppy disks, and later transferred on to an IBM-PC. So, at this stage we stored all 28 scans of A-line data (crosscorrelated and envelope detected), for the various parameters, into different floppy disks. For the purpose of file management, each B-scan data (consisting of 28 A-line data

⁸ If $M(x)$ is first signal of length 512 ($-255 < x < 256$), and $N(y)$ second of 1024 ($-511 < y < 512$), and if resultant of crosscorrelation is to be $R(z)$ of length 512 ($-255 < z < 255$), then: If we had '0' offset, the value of $\sum M(x)*N(y-0)$ would go to $R(-255)$, and that of $\sum M(x)*N(y+255)$ would go $R(0)$, so on. If we want the crosscorrelation to be symmetric about $R(0)$, we need to give an offset of -256 to as the parameter.

files) was stored on a different floppy disk. Figure 3.12 shows a flow chart of how these files were stored.

The most tedious but necessary step in the procedure of obtaining a gray scale image was that of conversion of all the data. Firstly we had to convert the data from Data 6000 format to ASCII format, and then we had to transfer it onto VAXIMG. After this, certain programs were run to combine the various one-dimensional A-scans into a two-dimensional B-scan, and then to convert them into a gray scale image, which could be displayed on the Gould-Deanza System on VAXIMG. So the description that follows, was carried out on each floppy drive data.

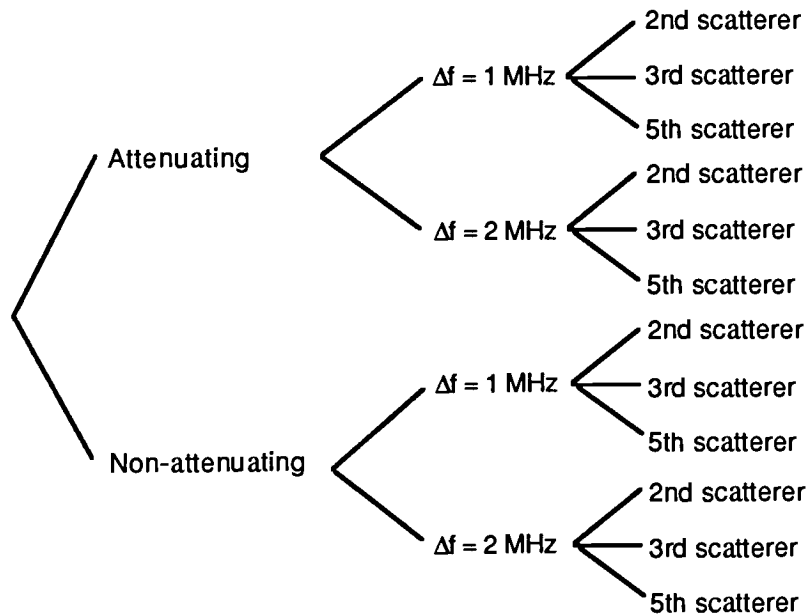
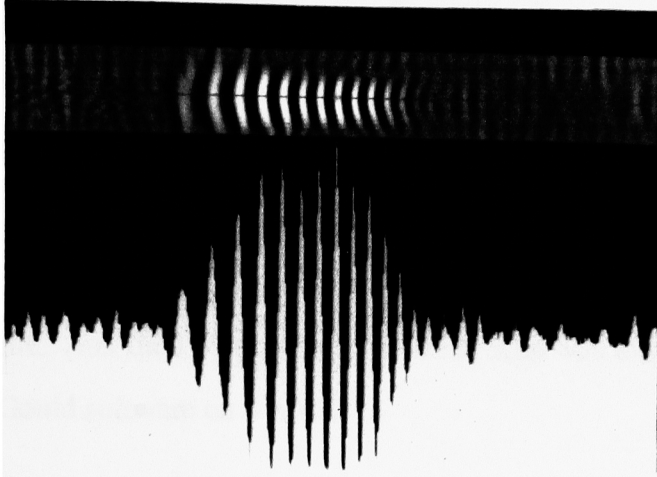
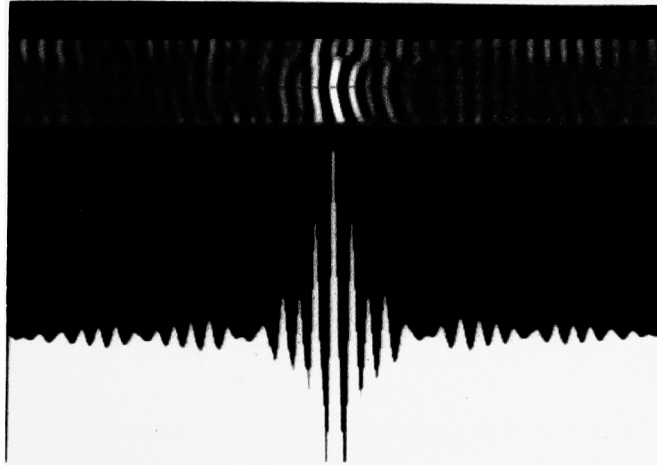


Figure 3.12 Flow chart of all the data recorded, for various parameters.

(a)



(b)



(c)

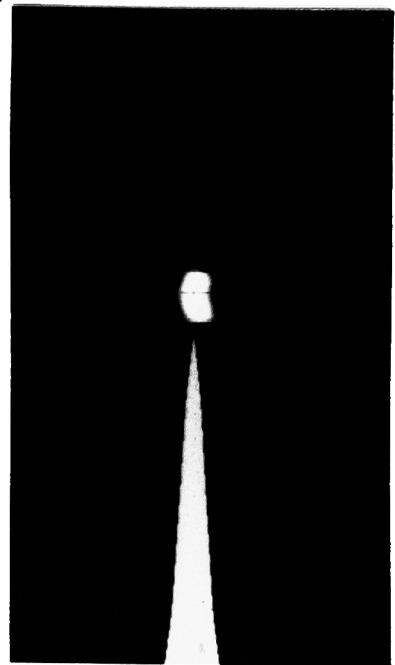


Figure 3.13 (a) Gray scale Backscattered RF signal, (b) post processed (after crosscorrelation) signal and (c) signal after envelope detection.

The data stored on the disks was of a generic Data6000 format, and was thus unreadable. A GWBASIC program (see Appendix H) was used to read the header from these files, and to convert them into ASCII files. This data was then transferred onto the VAX/VMS system using the 'Kermit' file transfer program. Once on the VAX, the data which was in different files for each scan line was collected together into one data file. For this purpose a "C" program (see Appendix I) was used. This program had the ability to combine all the 28 scan lines (for each B-scan set), and to convert them into an 8-bit image file. This final output, a gray scale B-scan was displayed on a monitor using the Deanza Gould software on VAXIMG.

Figure 3.13 on the previous page, shows an example of what the gray scale B-scan images looked like once they were finally displayed on the monitor. (a) shows the backscattered signal. (b) shows the crosscorrelated signal, and (c) shows the signal after envelope detection.

Chapter 4

Results, Analysis and Discussions

This chapter will include all the results that were obtained from the experimental work performed. It will also give a discussion of these results, and will include an analysis of all the data. The intent here is to give the reader an insight into what was going on with the pulse, when it interacted with the medium and the scatterers within. It is my hope that I succeed in doing so.

4.1 Results

The results shown in the figures that will follow, are all for envelope detected data. The experiment was carried out for both non-attenuating and attenuating medium. Further, for both media, data was recorded for two different bandwidths of 1MHz and 2MHz. The intent was to keep the central frequency fixed at 2.4MHz, and to study the variation in the

output images, with bandwidths only. But as it so happened, the empirically solved formula, that was used to generate the FM pulse from the PWG, was not error free and the central frequency for $\Delta f = 1$ MHz was 2.5MHz and for $\Delta f = 2$ MHz, it was 2.6MHz. However, for our purpose of evaluation, we will ignore this slight change in f_0 .

Once the B-scan image was created on the display, the parameter evaluated was the FWHM, both in the axial direction (along the beam path) and the lateral direction (across the beam). This was done by taking the profile of the image, in either directions, and then measuring the FWHM by looking at the values.

All the figures are for input FM pulse of $f_0 = 2.4$ MHz. The Δf in the figures(as shown in Plate 4-1) represents the bandwidth associated with the input FM pulse for each of the cases.

Axial Direction:

The following figures show the profile of the scan in the axial direction, i.e. along the direction of the beam propagation.(z) The shape here is governed by the envelope of the FM pulse, the envelope in turn depends on the bandwidth of the backscattered FM pulse. Further their are two more classifications in this direction that are to be considered:

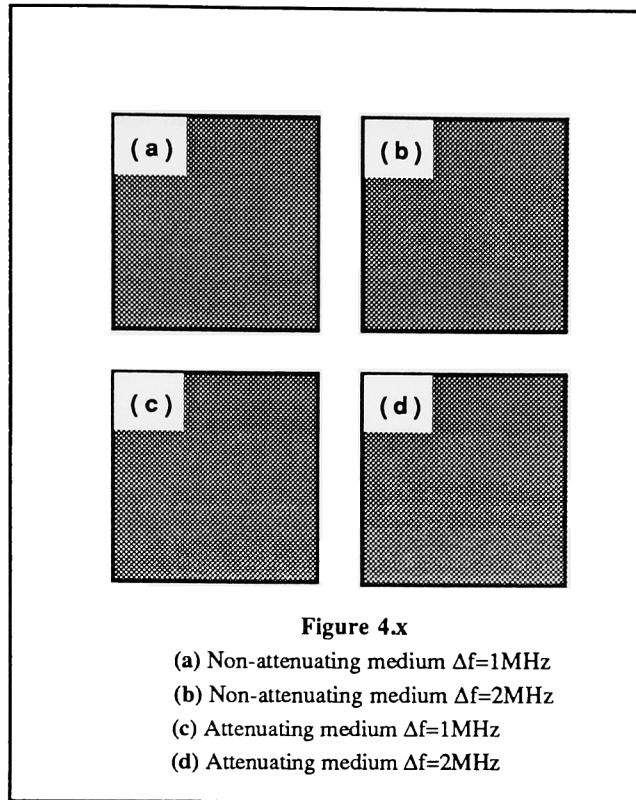


Plate 4-1 Block diagram of settings of the pictures in the templates shown later on in this section.

Crosscorrelation done using input FM pulse:

The following figures are all showing the axial direction profile of the B-scan images for envelope detected data, and have been generated by crosscorrelating the backscattered signal with the input FM pulse.

Figure 4.1 is for the 2nd scatterer (depth of 3.1cm)

Figure 4.2 is for the 3rd scatterer (depth of 5.1cm)

Figure 4.3 is for the 5th scatterer (depth of 9.1cm)

Figure 4.4 shows all three scatterers together (profile taken through the peaks of each on of them).

Crosscorrelation done using RF from 5th scatterer (central scan)

The following figures are all showing the axial direction profile of the B-scan images for envelope detected data, and have been generated by crosscorrelating the backscattered signal with the RF signal from the 5th scatterer(9.1cm, far-field). It should be pointed out that; this alternate crosscorrelation was performed just as a comparison to the FM pulse correlation. Results obtained showed similar trends in both axial and lateral direction. Thus analysis was eventually performed only for the case of FM pulse crosscorrelation.

Figure 4.5 is for the 2nd scatterer (depth of 3.1cm)

Figure 4.6 is for the 3rd scatterer (depth of 5.1cm)

Figure 4.7 is for the 5th scatterer (depth of 9.1cm)

Figure 4.4 shows all three scatterers together (profile taken through the peaks of each on of them).

Lateral Direction:

The following show the profile of the scan, in the lateral direction, i.e. across the beam (x). Thus as we go from the 2nd to the 5th scatterer, we are moving from near-field zone to far-field zone.

Crosscorrelation done using input FM pulse:

The following figures are all showing the axial direction profile of the B-scan images for envelope detected data, and have been generated by crosscorrelating the backscattered signal with the input FM pulse.

Figure 4.9 is for the 2nd scatterer (depth of 3.1cm)

Figure 4.10 is for the 3rd scatterer (depth of 5.1cm)

Figure 4.11 is for the 5th scatterer (depth of 9.1cm)

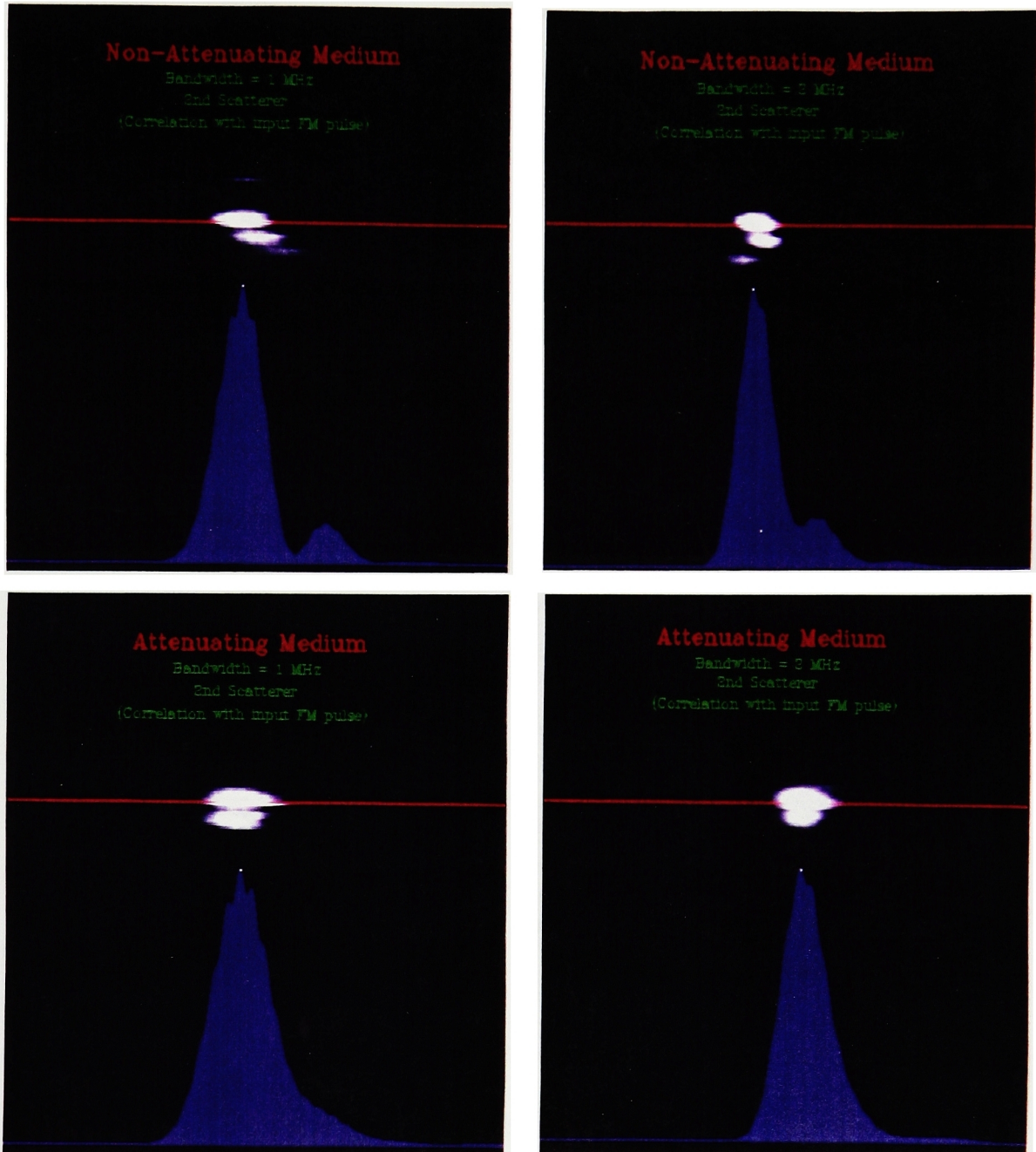


Figure 4.1 Envelope detected data of 2nd scatterer (a)-(b) Non Attenuating Medium (c)-(d) Attenuating Medium for 1MHz and 2MHz bandwidth, $f_0 = 2.4$ MHz. Crosscorrelation done with input FM pulse.

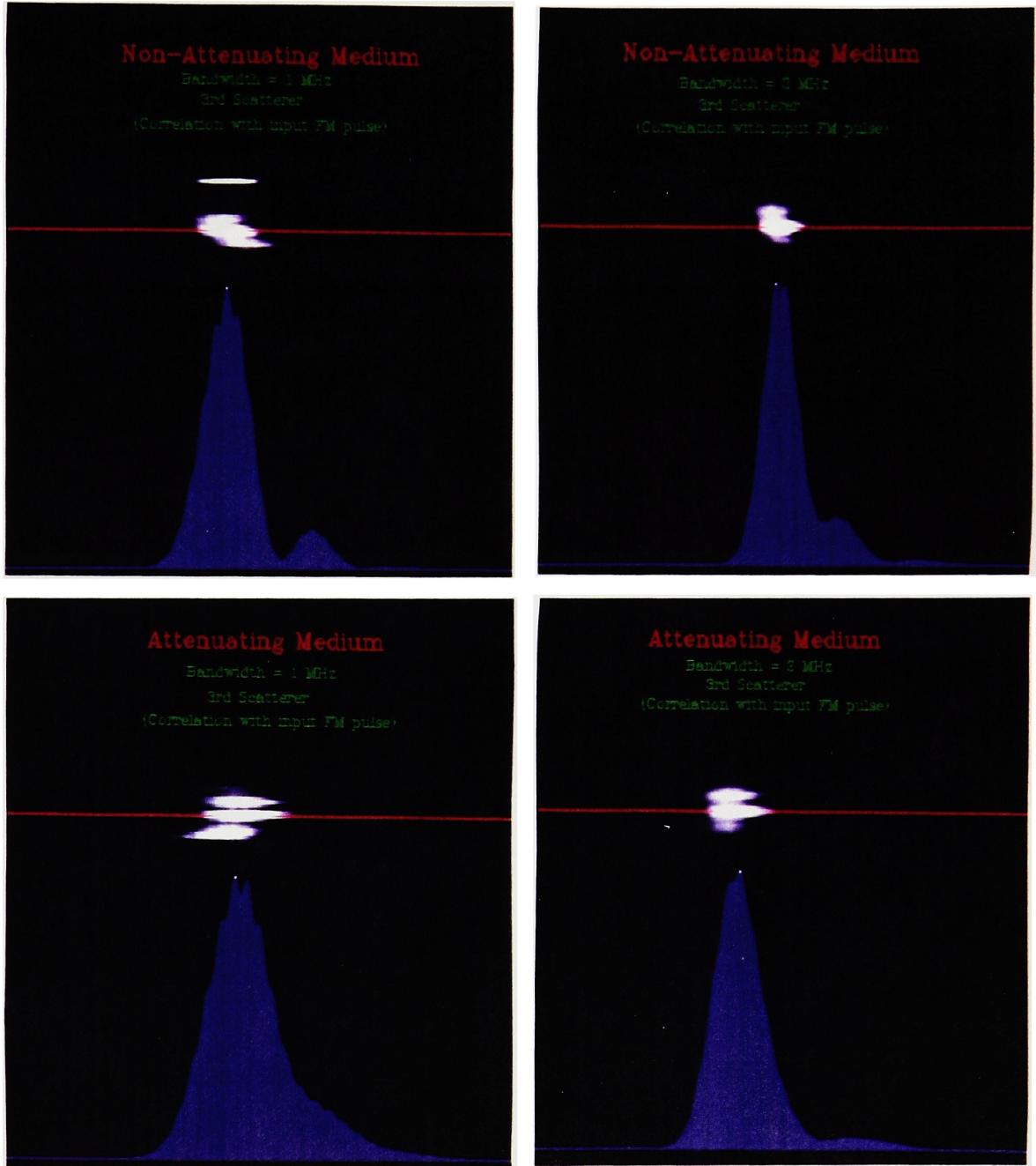


Figure 4.2 Envelope detected data of 3rd scatterer (a)-(b) Non Attenuating Medium (c)-(d) Attenuating Medium for 1MHz and 2MHz bandwidth, $f_0 = 2.4$ MHz. Crosscorrelation done with input FM pulse.

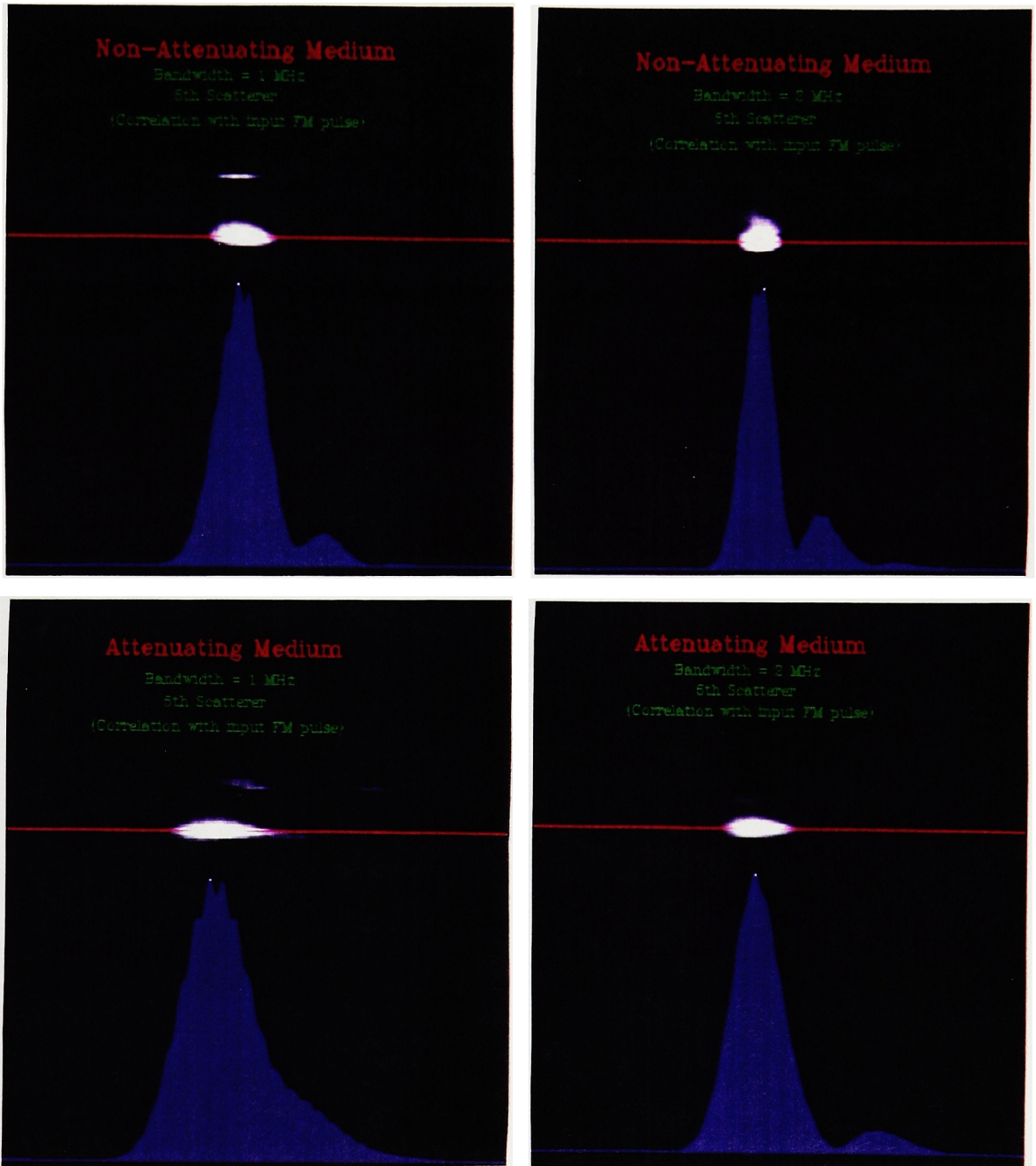


Figure 4.3 Envelope detected data of 5th scatterer (a)-(b) Non Attenuating Medium (c)-(d) Attenuating Medium for 1MHz and 2MHz bandwidth, $f_o = 2.4$ MHz. Crosscorrelation done with input FM pulse.

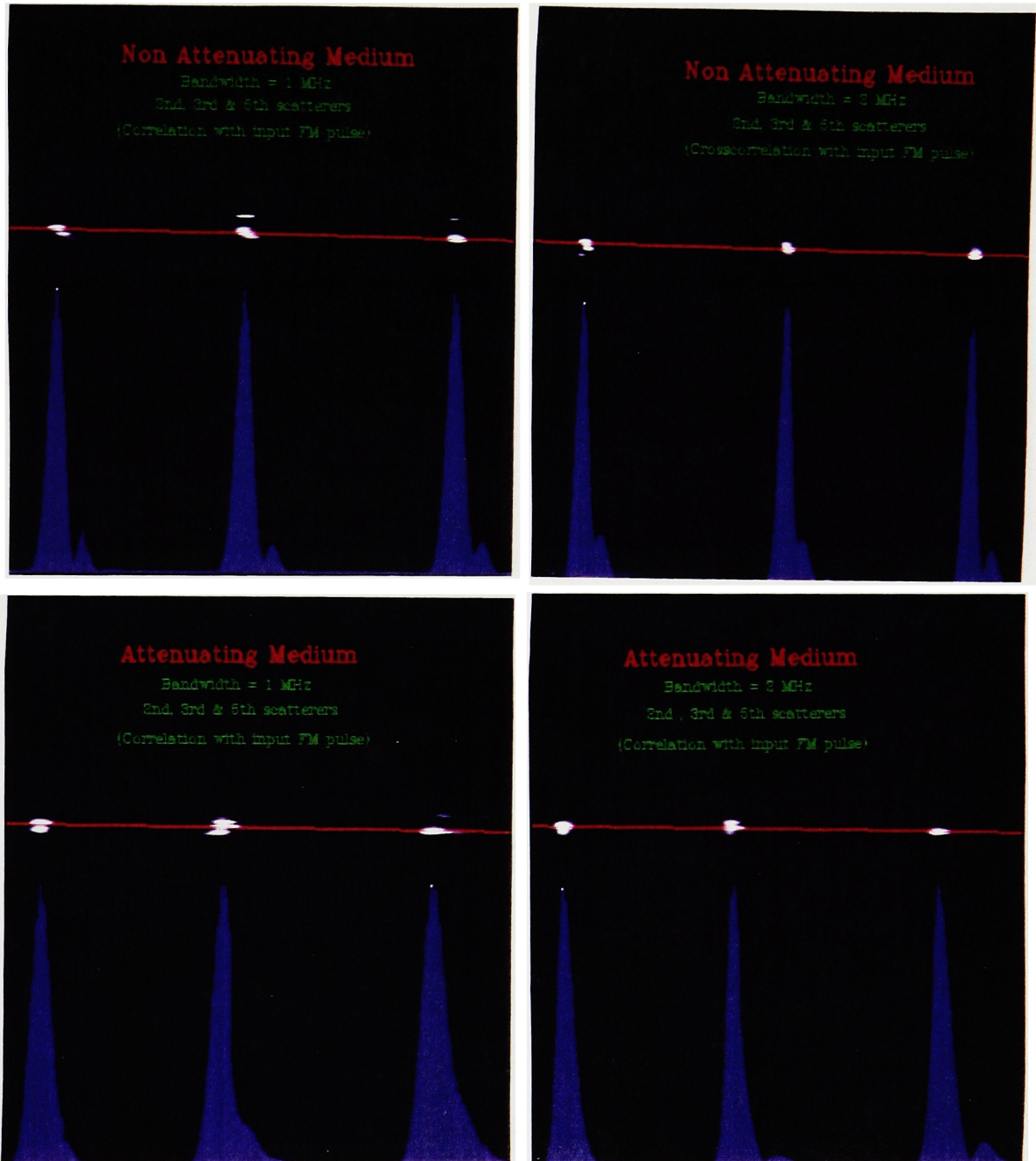


Figure 4.4 Envelope detected data of 2nd, 3rd & 5th scatterers (a)-(b) Non Attenuating Medium (c)-(d) Attenuating Medium for 1MHz and 2MHz bandwidth, $f_0 = 2.4$ MHz. Crosscorrelation done with input FM pulse.

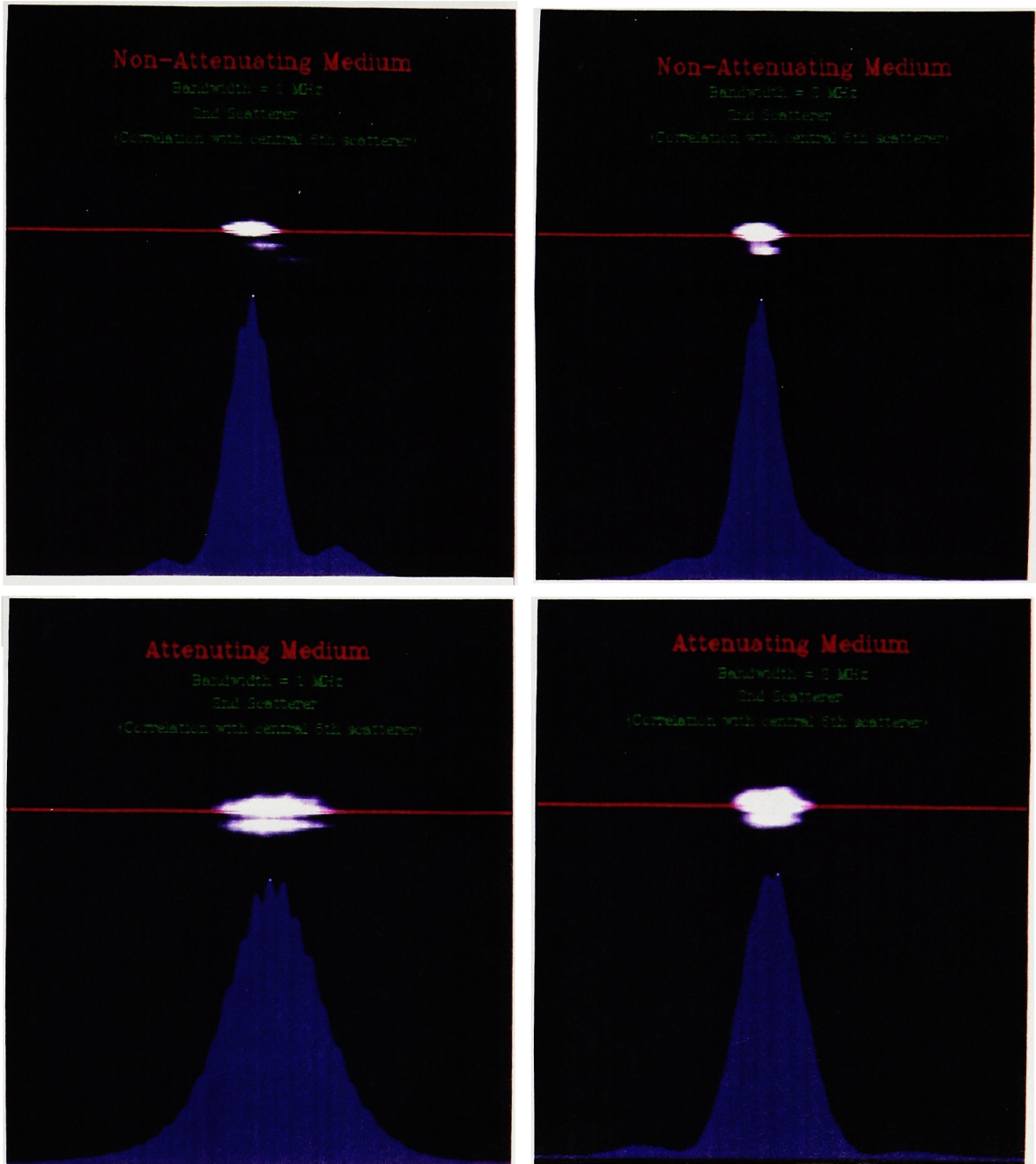


Figure 4.5 Envelope detected data of 2nd scatterer (a)-(b) Non Attenuating Medium (c)-(d) Attenuating Medium for 1MHz and 2MHz bandwidth, $f_0 = 2.4$ MHz. Crosscorrelation done with 5th scatterer (central scan).

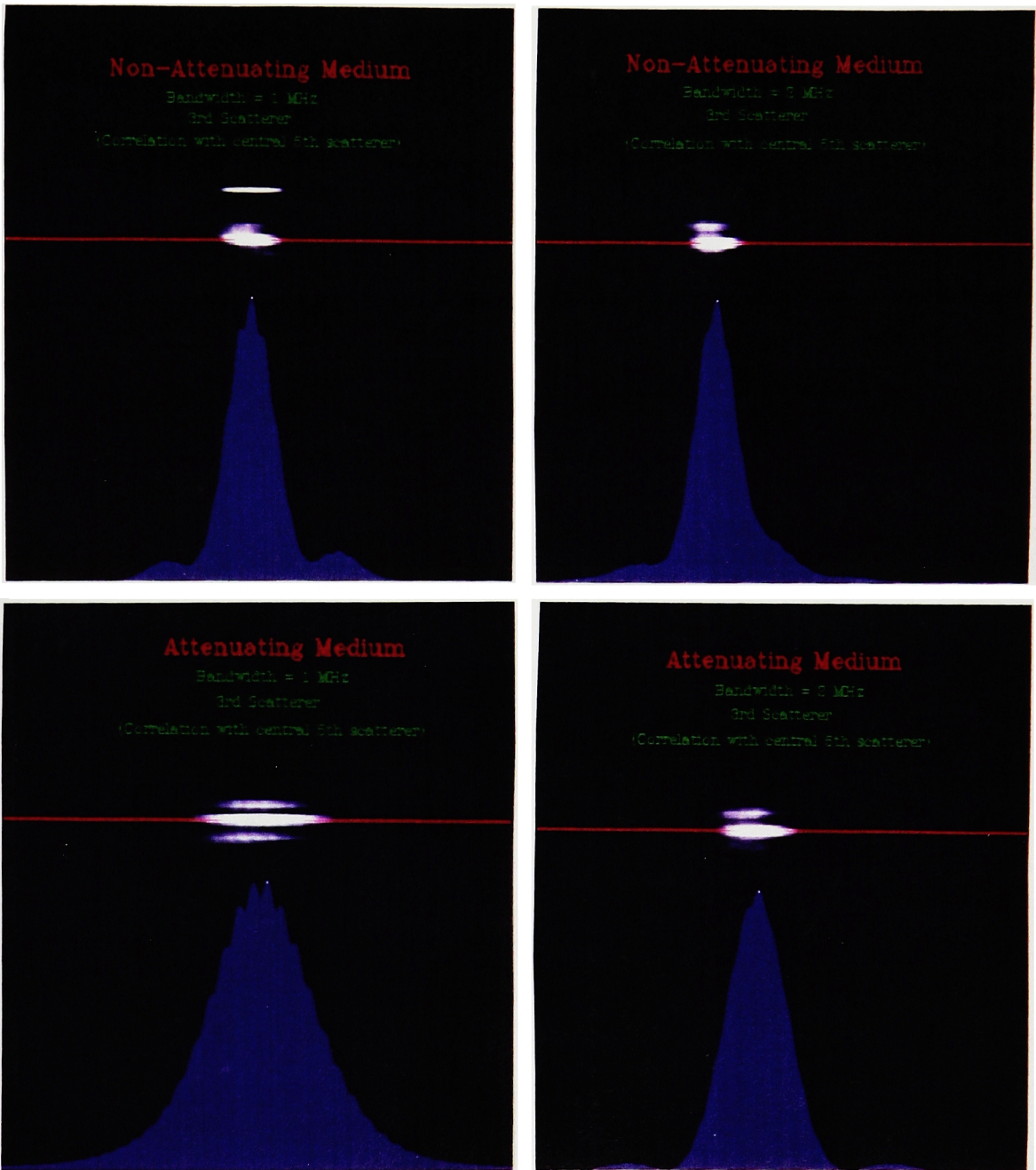


Figure 4.6 Envelope detected data of 3rd scatterer (a)-(b) Non Attenuating Medium (c)-(d) Attenuating Medium for 1MHz and 2MHz bandwidth, $f_0 = 2.4$ MHz. Crosscorrelation done with 5th scatterer (central scan).

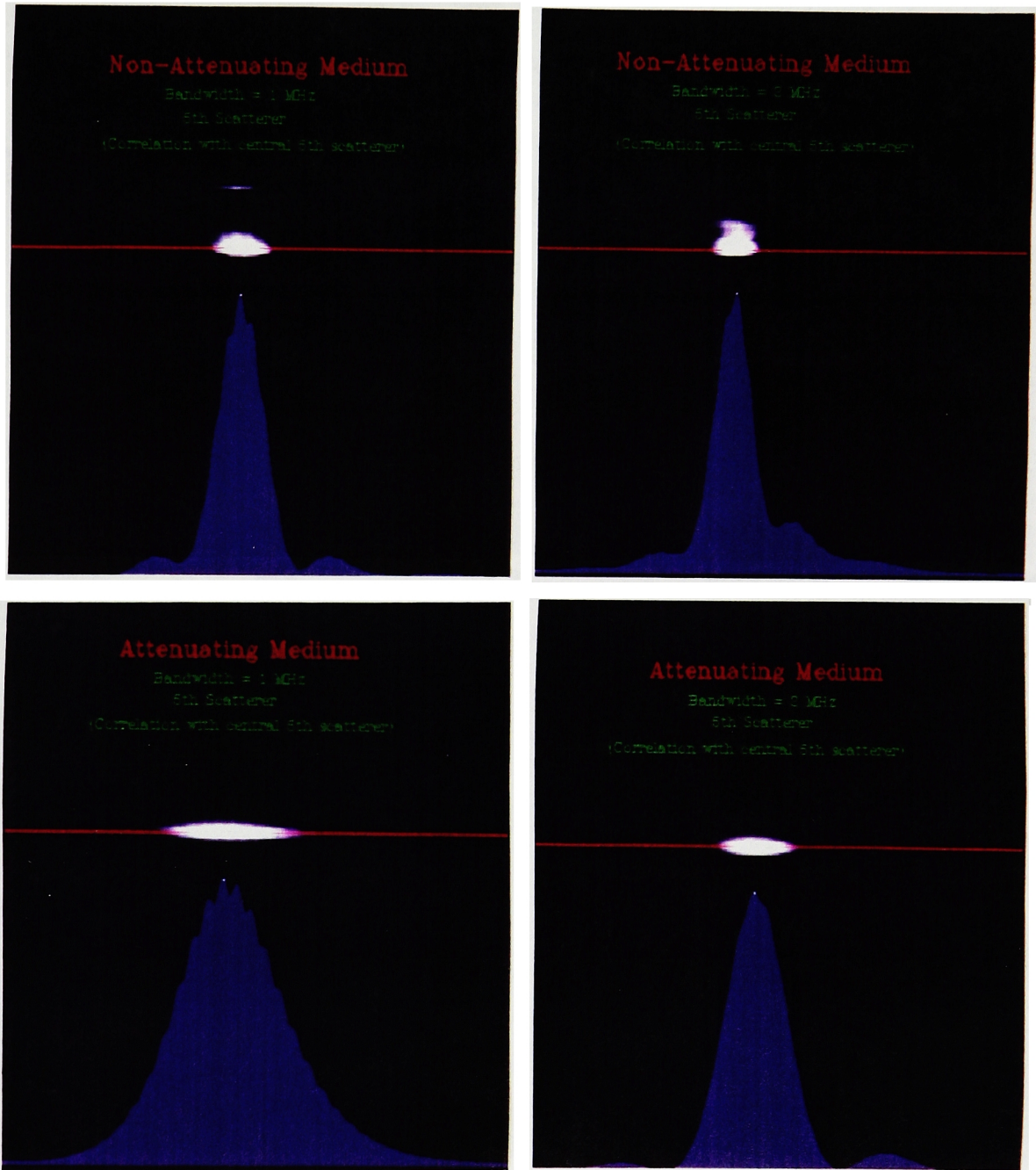


Figure 4.7 Envelope detected data of 5th scatterer (a)-(b) Non Attenuating Medium (c)-(d) Attenuating Medium for 1MHz and 2MHz bandwidth, $f_0 = 2.4$ MHz. Crosscorrelation done with 5th scatterer (central scan).

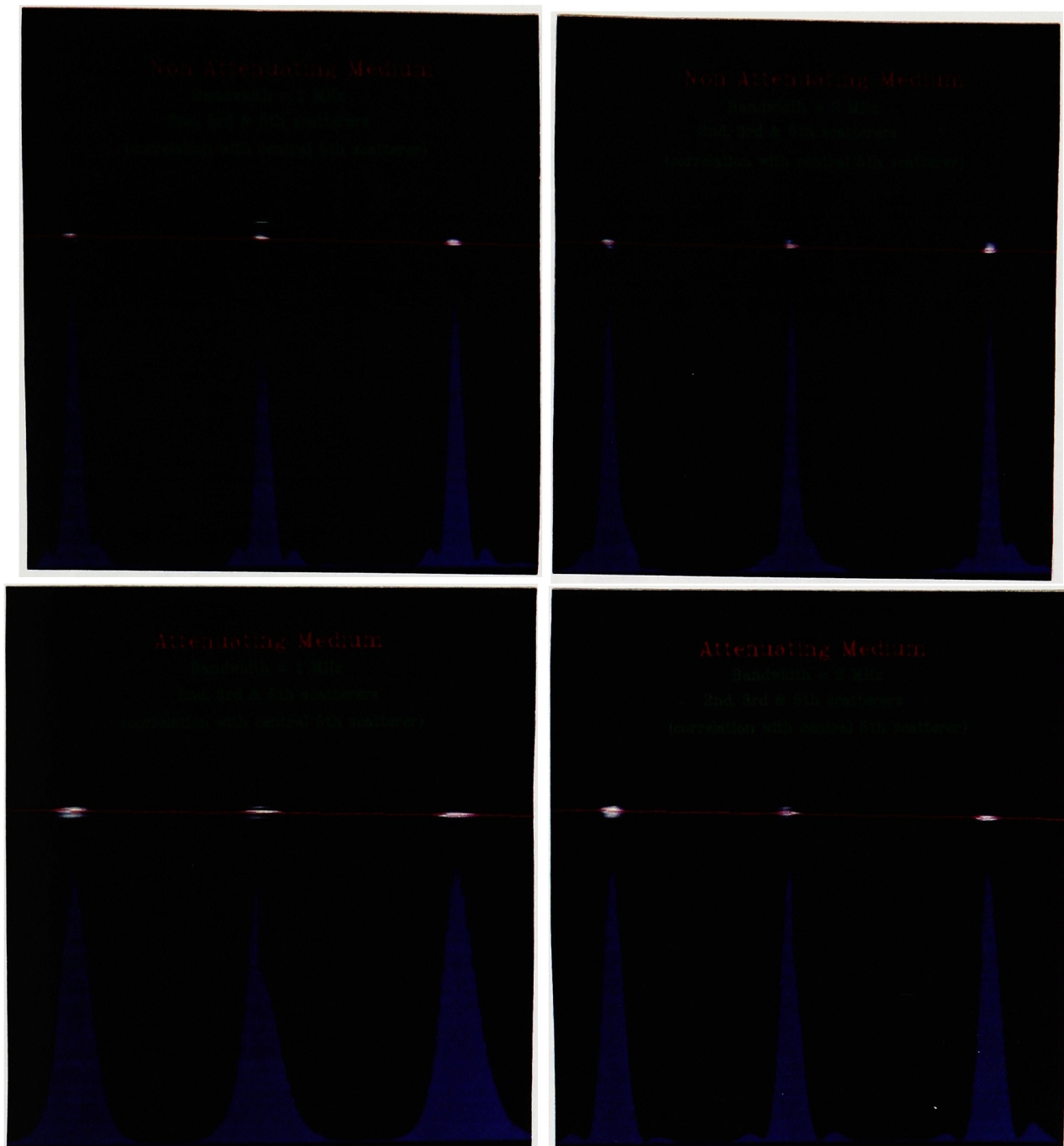


Figure 4.8 Envelope detected data of 2nd, 3rd & 5th scatterers (a)-(b) Non Attenuating Medium (c)-(d) Attenuating Medium for 1MHz and 2MHz bandwidth, $f_0 = 2.4$ MHz. Crosscorrelation done with 5th scatterer (central scan).

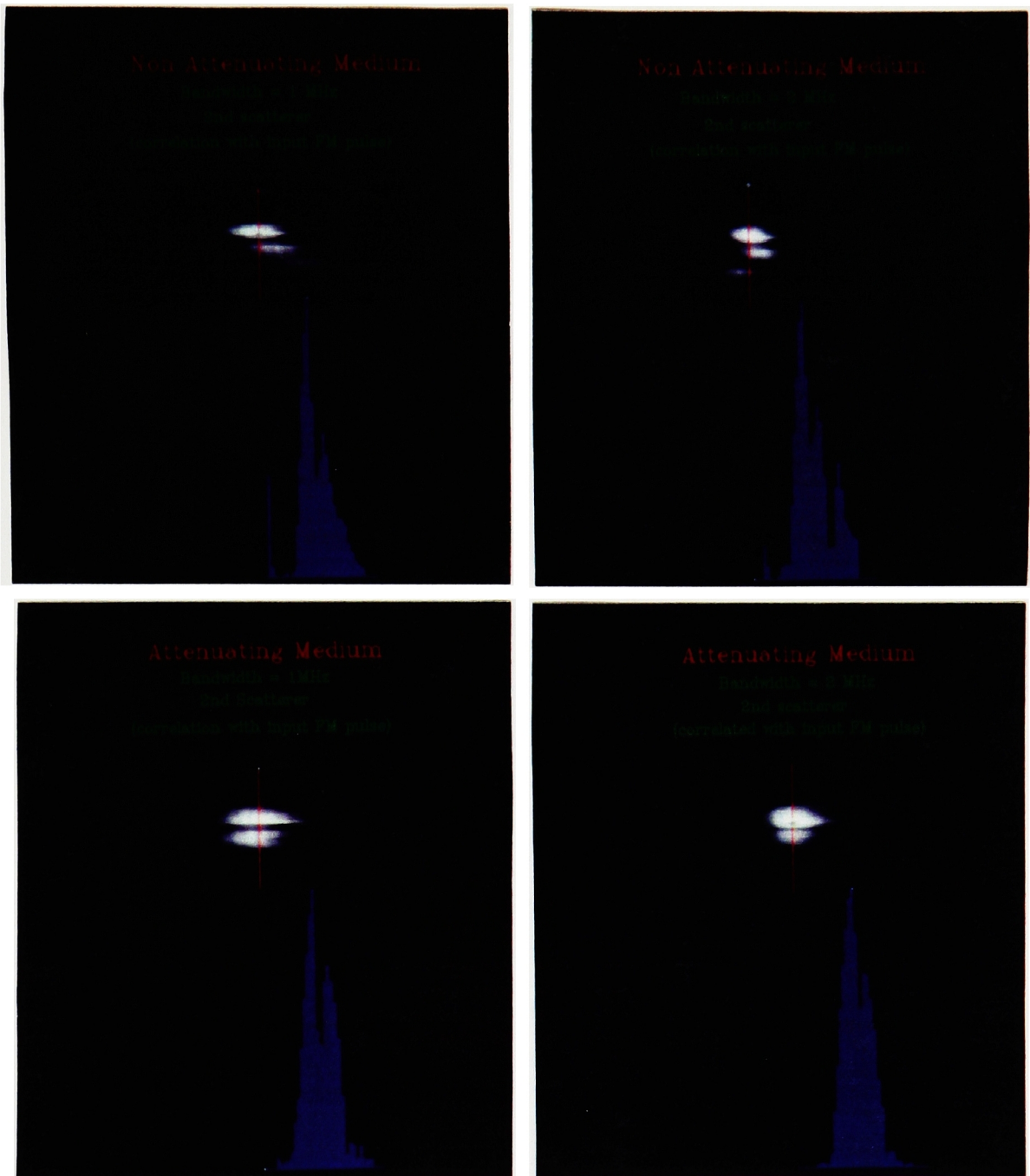


Figure 4.9 Envelope detected data of 2nd scatterer (a)-(b) Non Attenuating Medium (c)-(d) Attenuating Medium for 1MHz and 2MHz bandwidth, $f_0 = 2.4$ MHz. Crosscorrelation done with input FM pulse.

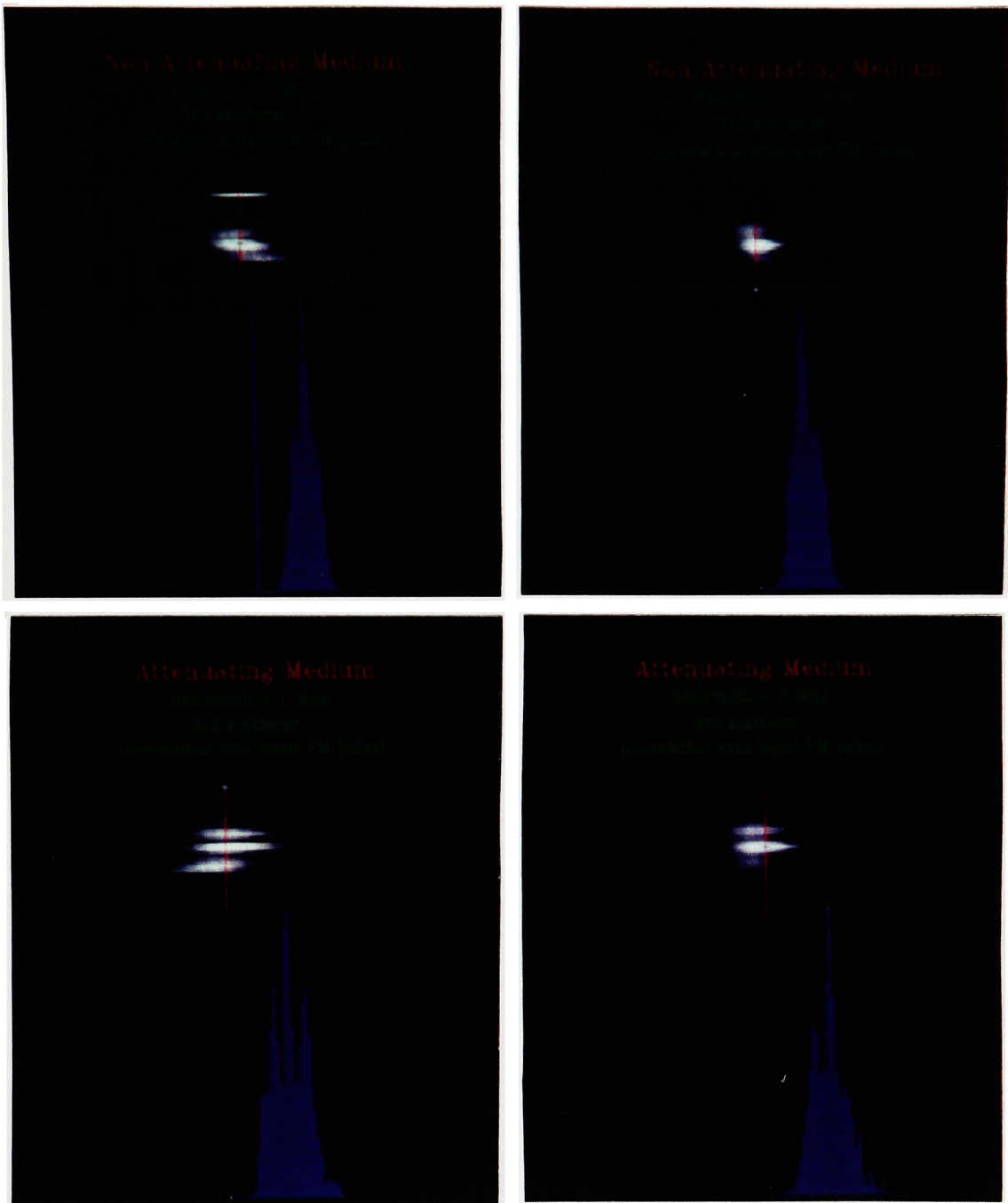


Figure 4.10 Envelope detected data of 3rd scatterer (a)-(b) Non Attenuating Medium (c)-(d) Attenuating Medium for 1MHz and 2MHz bandwidth, $f_0 = 2.4$ MHz. Crosscorrelation done with input FM pulse.

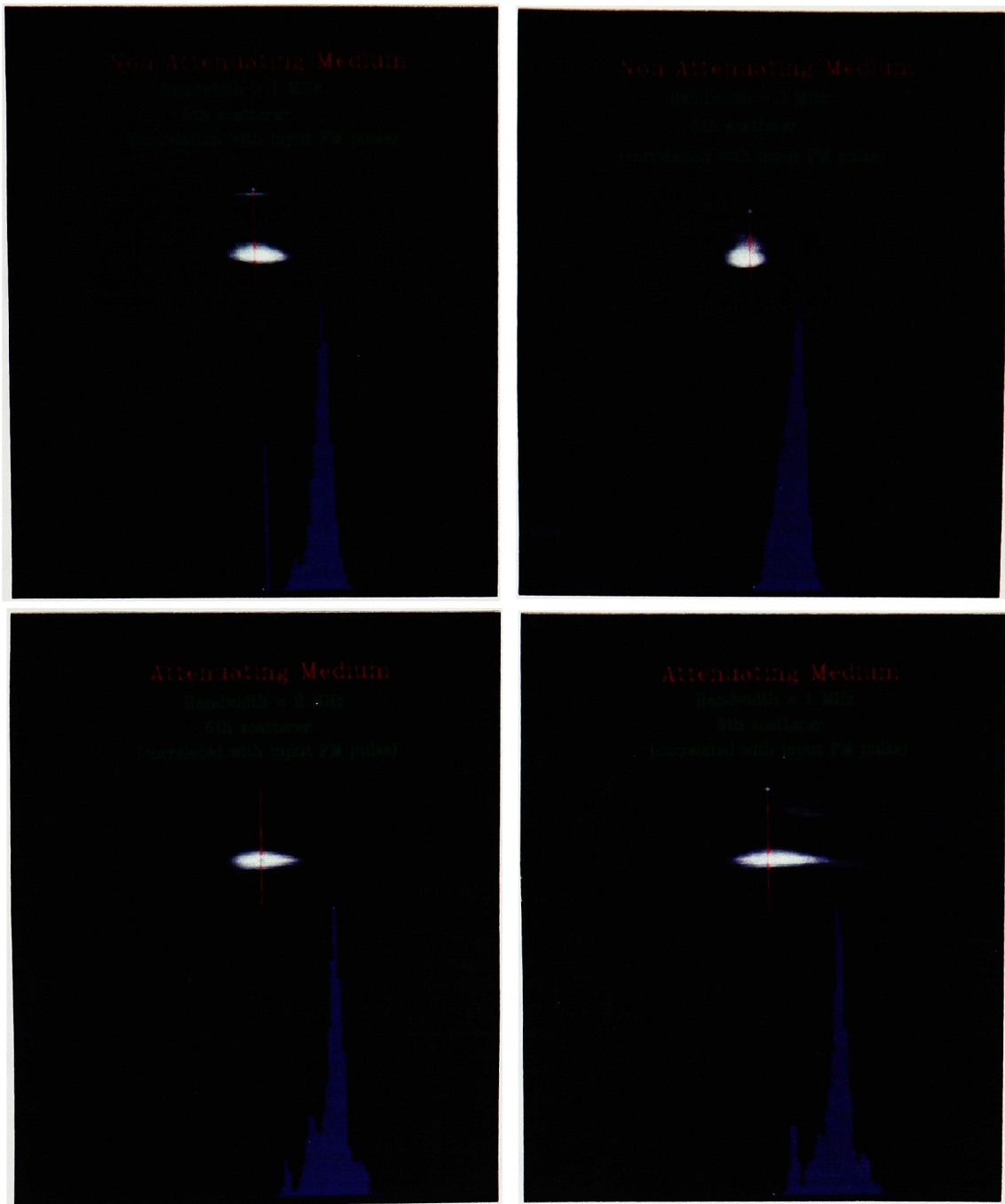


Figure 4.11 Envelope detected data of **5th scatterer** (a)-(b) Non Attenuating Medium (c)-(d) Attenuating Medium for 1MHz and 2MHz bandwidth, $f_0 = 2.4$ MHz. Crosscorrelation done with input FM pulse.

4.2 Analysis

Here, details of the analysis that was carried out on the experimental data are provided. References will be made to the figures shown earlier in Section 4.1, where needed. The parameters used for analysis and comparisons are discussed. Table 4.1 gives a quantitative description of the backscattered RF signal and of the envelopes detected B-scans.

For the analysis of envelope detected data, we evaluated the *Full Width at Half Maximum* (FWHM), both in the axial and lateral direction, for all cases. This was done by using the gray scale values, from the profile. First, the value at the peak was observed (typically 255), then the x-axis (along z-depth) value where gray scale went to 128 on either side of the peak, was recorded. This difference in the x-axis values gave us the FWHM. In the axial direction, each point depicted 20ns (sampling rate used by Data6000 for digitization), therefore a value of 54 in this direction would amount to a time lapse of 1.14 μ s. However, in the lateral direction, the measurement was in terms of the shift in the transducer across the phantom. The vernier used for doing so had a minimum resolution of 1mm, which was the distance between two A-scans. Therefore, a value of 10.5 (obtained by doing interpolation) in this direction corresponds to 10.5mm, as the lateral FWHM.

The backscattered data was analyzed by looking at the power spectrum of each scatterer from the central RF scan. An array of 1024 was selected from the entire 8192 RF signal, and its Fourier Transform was taken. Once in the frequency space, we could analyze the frequency content of the array, for each scatterer. For the purpose of

Medium	Bandwidth (MHz)	Scatterer (#)	Envelope Detected Data Analysis		Backscattered Data Analysis			
			Axial FWHM (μ s)	Lateral FWHM (mm)	f_H (MHz)	f_L (MHz)	f_0 (MHz)	Δf_{H-L} (MHz)
Attenuating	1	2nd (3.1cm)	1.14	10.50	2.78	1.60	2.190	1.18
		3rd (5.1cm)	1.30	11.50	2.59	1.60	2.095	0.99
		5th (9.1cm)	1.40	4.25	2.49	1.60	2.045	0.89
		2nd	0.92	10.20	2.78	1.03	1.900	1.75
		3rd	1.00	7.50	2.49	1.12	1.810	1.37
Non Attenuating	1	5th	1.02	4.40	2.39	1.07	1.730	1.32
		2nd	0.94	7.00	2.98	1.60	2.290	1.38
		3rd	0.94	7.20	2.98	1.66	2.320	1.32
		5th	0.94	5.40	2.98	1.66	2.320	1.32
		2nd	0.72	8.50	2.98	1.03	2.005	1.95
Attenuating	2	3rd	0.74	8.40	2.93	1.22	2.070	1.71
		5th	0.70	7.90	3.07	1.17	2.120	1.90

Table 4.1
 Analysis of backscattered RF signal, and of envelope after post processing
 (correlation with input FM pulse).

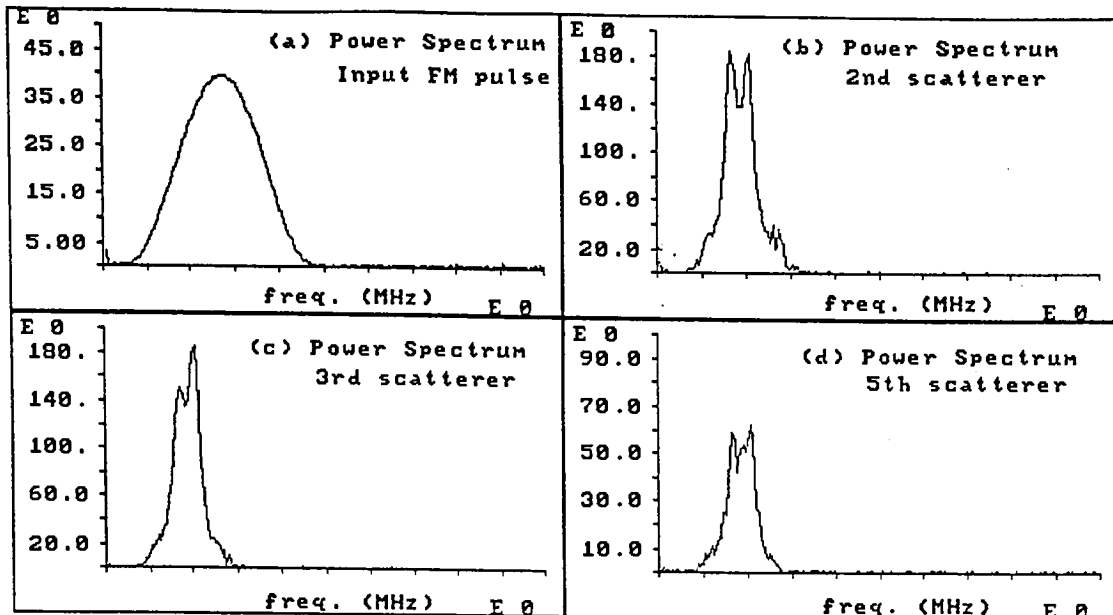


Figure 4.12 Comparison of power spectrums for (a) input FM pulse, (b) 2nd scatterer, (c) 3rd scatterer and (d) 5th scatterer.

quantitative analysis, certain numbers had to be obtained from this power spectrum. We chose to look at the width of the spectrum, at the 10% value. This was done by first evaluating the peak of the curve, and then going to the 10% point of this value at the higher (f_H) and lower (f_L) ends of the spectrum. This width was termed as the bandwidth Δf_{H-L} , and from this the central frequency f_0 was evaluated as $(\Delta f_{H-L}/2)$. The reason for choosing such a number for evaluation was simple. Qualitatively one can look at figure 4.12 and compare power spectrums of (a) input FM pulse, (b) 2nd scatterer, (c) 3rd scatterer and the (d) 5th scatterer. As can be seen the higher frequencies get attenuated more and more as we go deeper into the medium. However, to depict this qualitatively, required a number which would correctly show this drop. The FWHM was not a good parameter to quantify this change. As can be seen from figure 4.12, the width at the 50% value does not vary too much from one power spectrum to the other. But if we look at the 10% values, there is a considerable drop. Thus the reason for choosing this parameter. For the input FM pulse, these numbers were as follows:

Input Δf (MHz)	Power Spectrum		Output Δf_{H-L} (MHz)
	f_H (MHz)	f_L (MHz)	
1	3.26	1.64	1.62
2	4.20	0.88	3.32

Once the observations have been quantified, we can go ahead and make some comparisons. Figures 4.13 and 4.14 show plots of f_o and Δf_{H-L} versus depth. Plots were made for all four cases i.e. Non-attenuating and Attenuating medium, with input pulse bandwidths of 1 and 2MHz each., as shown in the legend The observations made here have been discussed in the section following this one.

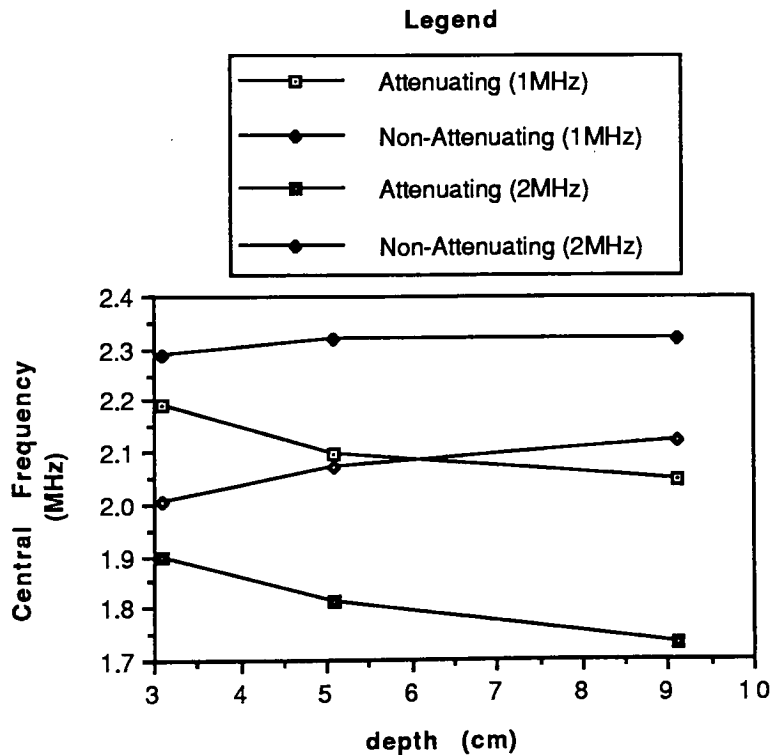


Figure 4.13 Plot of observed central frequency f_o versus depth.

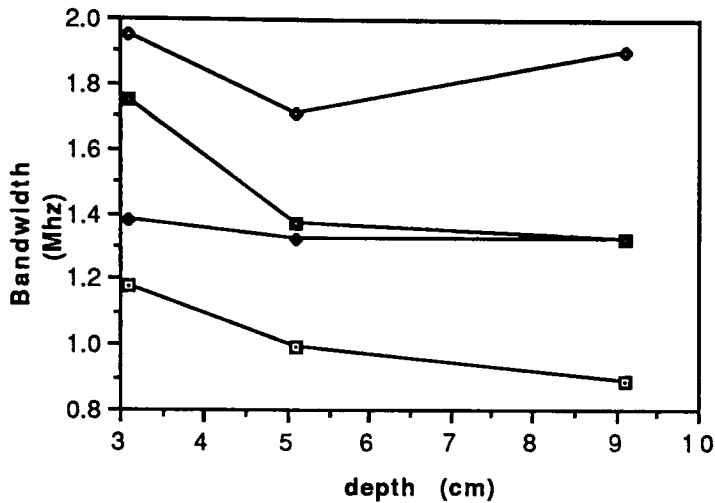


Figure 4.14 Plot of observed bandwidth Δf versus depth.

4.3 Discussion

The imaging performance of ultrasound imaging system is greatly dependent on the characteristics of the ultrasound transducer. The performance is specified by the two-dimensional point spread function (PSF) of the transmitted sound field. The analysis is further simplified by measuring the width of the envelope detected PSF in the lateral and axial direction. This has been measured and reported in Table 4.1. In the axial direction this PSF is fixed by the bandwidth Δf of the transducer. In the lateral direction the PSF to the first order, is determined by the central frequency f_0 of the interrogating pulse, and the

diffraction pattern produced by the transducer at that frequency. Because the diffraction pattern changes as a function of distance from transducer, the PSF is not spatially invariant, even in a non-attenuating medium. In a frequency dependent attenuating medium, the analysis of the PSF becomes even more complex. Theoretical simulation techniques, described in Section 3.1 can be used to predict the PSF exactly. However in the far-field, certain simple assumptions can be made in order to approximate the theoretical results and compare them to the experimental observations.

4.3.1 Spectrum of the Backscattered Signal

This thesis describes the use of frequency modulated interrogating pulse. For a fixed central frequency of 2.4MHz, two different bandwidths, 1MHz and 2MHz were used. These are the FWHM bandwidths of the input voltage signal that drives the transducer. The spectrum of the backscattered RF signal can be different from the input spectrum due to four factors. Those are: (1) The shape and the spectrum of the FM pulse transmitted by the transducer is dictated by the transducer transfer function shown in figure 3.8 earlier. The spectrum is again modified by the same transducer transfer function upon reception. (2) In an attenuating medium, the pulse spectrum can change as the pulse propagates. This is because the attenuation in the medium is frequency dependent, higher frequencies are attenuated more than the lower than the lower frequencies. This effect has been demonstrated through simulation in Section 3.2. (3) The spectrum can also change due to diffraction effects, because several different frequencies are present in the pulse and each one has a different diffraction pattern. However, this effect will be observed only for

reflectors that are located off the main axis of the transducer. Since the spectrum analysis has been carried out along the main axis of the transducer, this factor can be disregarded.

(4) Frequency dependent reflection coefficient or resonance scattering effects can also alter the spectrum.

Even though the excitation signal input to the transducer had a symmetric spectrum, the experimental backscattered data did not. This could be due to any of the reasons mentioned in the preceding paragraph. Therefore, as mentioned earlier, it was decided to perform the spectrum analysis where 10% of the peak value on the low and high frequency side was measured, instead of FWHM. The bandwidth Δf_{H-L} is the difference between these two values, and the center frequency f_0 is the mid point of this bandwidth. The results of the analysis are shown in Table 4.1, and are also plotted in figure 4.13 and 4.14, as a function of the depth (or distance z) of the scatterer from the transducer. In the analysis section, the transition zone to the far-field was estimated at about 6.4 cm. Therefore only the 5th scatterer (9.1cm depth) is in the far-field, the 2nd (3.1cm depth) is in the near-field and the 3rd (5.1cm depth) is approximately in the transition zone. For the purpose of comparison, Δf_{H-L} was also calculated as the input FM pulse spectrum. It was found to be 1.62MHz for the 1MHz case and 3.32MHz for the 2MHz case.

4.3.2 Axial Resolution

The FWHM of the envelope detected signal, in the axial direction is reported in Table 4.1. It is measured in μs , but for a nominal speed of sound of 1520 m/s, these

numbers can be converted to resolution in mm ($1\mu\text{s} = 0.76\text{mm}$). As expected, a clear correlation is observed between the axial resolution and the bandwidth of the backscattered signal. This is found to be true for both attenuating and non-attenuating medium and scatterers in different zones. This change in the bandwidth was effected by controlling the bandwidth of the input FM pulse.

Shown in figure 4.14 are the plots for bandwidth as a function of depth. In our experimental setup, the pulse has a hanning weighted window, which results in a non-gaussian spectrum. If our spectrum of the input was gaussian, then in that case we would not observe any deviations in the bandwidth as a function of depth [Kuc76, Ferrari85]. However there would be a downshift in the center frequency for greater depths (see figure 4.13). Once again, since our pulse does not have an exact gaussian shape, and in addition it is not known if the attenuating medium was exactly linear with frequency, we observe a change in bandwidth as we go deeper into the phantom (see figure 4.14).

4.3.3 Frequency Downshift

The nominal linear attenuation coefficient of the attenuating medium (phantom) was stated by the manufacturer to be $\alpha_0 = 0.15 \text{ dB/cm/MHz}$. Computer simulations were performed (Section 3.2) to study the propagation affects on a broadband FM pulse. α_0 of the medium and f_0 and Δf of the FM pulse were varied over values that are reasonable for soft tissue imaging. In all cases a down shift in f_0 and a fractional increase in Δf was observed. This effect has also been observed in the simulation work of several others

[Nikoonahad89]. It should be pointed out that the work in the references above was related to broadband short pulse.

Qualitatively similar affects are also observed in the experimental data presented in this thesis. Figure 4.13 shows the down shift in the central frequency in the attenuating medium. The center frequency of the FM pulse input to the transducer was 2.46MHz and 2.62MHz respectively for 1 & 2MHz bandwidth cases. The exact center frequency value for the pulse input to the medium is not known. There is a possibility that some downshift may have occurred as pulse propagates through a 4mm thick plexiglass cover. Nevertheless, a decrease in f_0 can be clearly seen, in both 1 & 2MHz bandwidth case. In the non-attenuating case, frequency shift should be very small. That is indeed the case for 1MHz bandwidth. But for the 2MHz bandwidth a slight increase in f_0 is observed, as the pulse propagates throughout the medium. The reason for this is not clear. It may have something to do with the multiple scattering effects. The spectrum of the backscattered signal in non-attenuating case had 2 prominent peaks. Calculating center frequency in such a spectrum can be misleading.

4.3.4 Lateral Resolution in Far-Field

The FWHM of the envelope detected signal, in the lateral direction is reported in Table 4.1. This number, in general can be used to denote the lateral resolution of the signal. It essentially depends on the beam profile of the transducer, and therefore, is diffraction limited. Because of the very nature of diffraction phenomenon, lateral resolution of the

system can vary significantly at different points in the image field. It is also the most difficult to calculate exactly, because of the broadband nature of the transducer excitation. Various techniques to calculate the beam profile under pulsed (broadband) conditions by different researchers were mentioned in Section 3.1.2. Only an approximate analysis is considered here, which applies to the far-field data. Assuming that the pulse spectrum is sufficiently narrowband so that we can approximate the far-field diffraction pattern by a *Sombbrero* function for a circular transducer of diameter “d”:

$$\text{Far-field diffraction pattern} = (\text{constant}) \frac{J_1\left(\frac{\pi \cdot d \cdot r}{\lambda \cdot z}\right)}{\left(\frac{\pi \cdot d \cdot r}{\lambda \cdot z}\right)} = (\text{constant}) \frac{J_1(\pi \cdot \theta)}{(\pi \cdot \theta)} \quad \dots(4.1)$$

...with $\theta = \left(\frac{d \cdot r}{\lambda \cdot z}\right)$

where r is the radial distance from the central axis, λ is the wavelength calculated at the center frequency f_0 of a narrow bandwidth pulse, and z is the distance of the scatterer from the transducer. While this expression is correct for a single frequency excitation, question remains whether it can be used for pulsed or bandwidth excitation. Some experiments [Kossoff79] and simulations [Nikoonahad89, Verhoef84] indicate that this is allowed in the far-field (or focal plane) to a fair approximation.

The lateral PSF for the pulse-echo imaging is given by $\left[\frac{J(\pi \cdot \theta)}{(\pi \cdot \theta)}\right]^2$. The first power is due to the receiving directivity of the transducer and the other power is due to the strength of the insonification. What has been measured on the experimental data is the

FWHM in the lateral direction. We should compare it to the FWHM of this theoretical PSF approximation. From the behaviour of the Bessel function [Gaskill88] we can approximate theoretically expected lateral FWHM:

$$\text{Lateral FWHM} \approx 0.98 \frac{\lambda \cdot z}{d} = 0.98 \cdot \frac{c}{f_0} \cdot \frac{z}{d}$$

Assuming speed of sound c , in water (non-attenuating medium) to be 1500 m/s, the wavelength $\lambda \approx 0.065$ cm @ $f_0 = 2.32$ MHz. The transducer diameter $d = 1.27$ cm. Therefore for the scatterer in far-field ($z \approx 9.1$ cm), we get a value of lateral FWHM ≈ 4.56 mm. From Table 4.1, our measured value is about 5.4 mm. Similarly if we account for the down-shift in central frequency to $f_0 = 2.12$ MHz for wider bandwidth (2 MHz) case, and calculate the expected FWHM value, we get approximately 5 mm. But the observed FWHM is much worse, about 7.9 mm. This degradation is perhaps due to the wider bandwidth operation. Such an effect has been predicted by Nikoonahad89 based on their simulation results.

In the attenuating medium, the speed was estimated to be 1520 m/s. Similar calculation of the expected lateral FWHM gives values 5.2 mm and 6.1 mm for 1 & 2 MHz bandwidth case. The observed values are 4.25 mm and 4.4 mm. As bandwidth increases, the observed lateral resolution decreases, but it is nowhere near what is seen in the non-attenuating case. While this is a good sign for the FM pulse imaging scheme, the reason is not clear at the present time. The degree of degradation in the lateral resolution predicted by

Nikoonahad89 is not observed here, perhaps because the bandwidth is lower in this case ($\Delta f_{H-L} = 1.32\text{MHz}$ in attenuating case as opposed to 1.9MHz in the non-attenuating case).

4.3.5 Lateral Resolution in the Near-Field

There can be no absolute simple definition of the lateral resolution in the near-field. This is because the diffraction pattern for a broadband source can be very complex. Multiple maxima and minima can occur in the beam profile [Halliwell76,Woodcock79,Madsen81]. From figure 4.9 and 4.10 the lateral PSF for the scatterer at 3.1cm and 5.1cm appear to be in qualitative agreement with other experiments performed with short pulse excitation. More quantitative comparison will require simulation and comparison of the beam profiles. Nevertheless, the FWHM was measured for these scatterers and is reported in Table 4.1.

Chapter 5

Applications

This chapter will briefly discuss some of the applications of Frequency Modulated pulse in the area of medical diagnostic imaging. Some of these evaluations were carried out quantitatively and others are simply described but have not been performed as part of this thesis.

5.1 Reduction of Speckle Noise

The very first application that comes to mind for the Frequency Modulated pulse is in the area of speckle noise reduction (Speckle noise has been discussed earlier in chapter 2). From the fundamental result of probability theory the sum of K identically distributed, real-valued, uncorrelated random variables have a mean which is K times the mean of any one component, and a standard deviation which is \sqrt{K} times the standard deviation of one

component. Thus if we add K uncorrelated speckle patterns on an irradiance basis, the contrast is reduced by $1/\sqrt{K}$ [Goodman76].

An FM pulse can be used for imaging a randomly distributed pattern in any given medium. Speckle patterns in imaging systems such as ultrasound B-scans are classically interpreted as a result of coherent summation of responses from a large number of scattering targets. For instance if we are imaging a phantom, like the one described in earlier chapters, then the parts that we are truly interested in are the scatterers (steel wires), which are embedded in the phantom. The medium inside the phantom is made up of randomly distributed particles, which from a diagnostic point of view behaves like speckle noise. The argument here is that the FM pulse can be used to reduce the amount of background noise, by doing an averaging over several scans of the same area, each time using a different parameter for imaging. By this we mean that a scan of the same A-line can be obtained for different central frequencies of the input pulse. This would give us several backscattered signals, each one of them uncorrelated to the other. Now we could do an averaging over all the scans to obtain a signal which would have much lower contrast than what we would have got from a single scan.

It should be pointed out that the type of transducer which would be used for such a scheme would have to have a similar response over a wide range of frequencies. Once setup, the B-scan images can be obtained in a similar fashion, as obtained for this thesis. In the conventional short pulse imaging it is not possible to change the pulse and beam width without changing the transducer.

5.2 Tissue Characterization using Speckle Statistics

The area of tissue characterization is of interest to a gamut of people in the area of diagnostic imaging. In order to be able to distinguish between good and malignant tissue, images need to be generated which would depict such a variation clearly, for the pathologist. The FM pulse can be used to generate backscattered signals, which would carry such information. However this information is embedded in the signal and needs to be extracted. Some work has been done to study the speckle statistics variations with imaging system impulse response in these soft tissues.

It has been suggested in various publications that signal-to-noise ratio (SNR) be used as a tissue characterization parameter. Envelope detected signal is known to possess a Rayleigh distribution and a SNR of 1.91, whereas the intensity signal has a limiting SNR of 1. Departure from this value has been reported in previous publications by Rao⁸⁹. Some more work was carried out in this area, by studying deviation from the above stated value, for a variation in the resolution cell volume, for a fixed scatterer density. Its usefulness has been demonstrated in tissue characterization. For details of this work refer to Appendix J, where a copy of this work has been included.

5.3 Reduction of Cavitation Possibilities

Ultrasound imaging is a non-ionizing imaging process, and possesses less danger of side effects than certain other imaging modalities. However using a conventional short

pulse for diagnosis seems to have sparked some concern in the minds of people in the ultrasonic imaging community. And it has been shown in laboratory experiments, that using such a scheme could have a danger of transient cavitation in the body, if there were any micron size bubbles present in the medium Crum⁸⁶, Flynn³², Carson⁷⁸.

Transient cavitation occurs when a micron size bubble suddenly collapses, within one cycle of a high intensity short pulse. This collapse results in the production of free radicals, which in turn produce chemical changes in the tissue. In order to get over this possible effect, one has to either reduce the intensity of the short pulse with in this framework or come up with another pulse. Reducing the intensity, would result in a degradation of the image, as the signal to noise will go down, this could lead to misdiagnosis. Thus the only other way, is to use an FM pulse scheme. The intensity of the FM pulse is to the order of 10 shorter than the short pulse.

Chapter 6

Conclusions and Recommendations

Although the study conducted as part of this thesis, of the Frequency Modulated pulse was very complex, and provided some unusual results, it was in no way the complete analysis of this technique. Due to the constraints of time, and the bounds of a Master's thesis, it was not possible to carry out certain objectives. However a student could take up from where this work has concluded, and carry on with further research into this technique. I have drawn the following conclusions from, and have provided some suggestions regarding future research in this area:

- (1) The usefulness of the Frequency Modulated pulse has been demonstrated, as an interrogating modality for the purpose of medical diagnostic imaging.
- (2) The variations in signal obtained as we went deeper into the medium were as expected, attenuated in the frequency domain.
- (3) Far-field and Near-field observations were also as expected.

- (4) Dispersion effects, which were not accounted for in the simulations, need to be studied.
- (5) Variations were made only in the bandwidth of the interrogating pulse. The results were satisfactory. However, work remains to be done for studying the variations in the observed backscattered signal, as a function of central frequency of the FM pulse.
- (6) The duration of the pulse in this thesis was kept constant at $20\mu\text{s}$, one could vary this length, and observe changes in the B-scan images obtained.

Appendices

Appendix A

Solving for Impulse Response in Attenuating Medium

To solve for the impulse response of attenuation, we need to take the Inverse Fourier Transform (IFT) of the *transfer function* of the system. From work done by Kak and Dines [78] we obtain the transfer function $H(f)$ as:

$$H(f) = A \cdot e^{-\alpha(f) \cdot d} \cdot e^{-i \cdot 2\pi \cdot f \cdot \frac{d}{c}}$$

Here A is the reflection coefficient, the first exponential term is the amplitude term $|H(f)|$ and the second one is the phase term $\phi(f)$. $\alpha(f) = \alpha_0 f$ is the attenuation coefficient, which has been discussed in Chapter 2. d is the two-way travel distance, and d/c is the transit time where c is the speed of sound in medium (~ 1540 cm/ μ s).

For the moment, if we disregard the phase term and take the IFT of $|H(f)|$ we have:

$$\begin{aligned} \text{From Fourier pairs} \quad \frac{1}{2}\alpha \cdot e^{-\alpha \cdot |f|} &\Leftrightarrow \frac{\alpha^2}{\alpha^2 + 4\pi^2 t^2} \\ \therefore F^{-1}\{e^{-\alpha \cdot |f|}\} &\Rightarrow \frac{2 \cdot \alpha}{\alpha^2 + 4\pi^2 t^2} \\ \therefore F^{-1}\{A \cdot e^{-\alpha_0 d \cdot |f|}\} &\Rightarrow A \cdot \frac{2 \cdot \alpha_0 \cdot d}{[(\alpha_0 d)^2 + (2\pi)^2 \cdot t^2]} \end{aligned}$$

$\dots \alpha = \alpha_0 \cdot d$

$$\Rightarrow A \cdot \frac{2 \cdot \frac{\alpha_0 d}{2\pi}}{\left[\left(\frac{\alpha_0 d}{2\pi}\right)^2 + t^2\right]}$$

$$\Rightarrow \frac{A}{\pi} \cdot \frac{\left(\frac{\alpha_0 d}{2\pi}\right)}{\left[\left(\frac{\alpha_0 d}{2\pi}\right)^2 + t^2\right]}$$

Now, incorporating the phase shift, we have

$$F^{-1} \left\{ e^{-\alpha_0 d |f|} \cdot e^{-2\pi f \frac{d}{c}} \right\} \Rightarrow \frac{A}{\pi} \cdot \frac{\left(\frac{\alpha_0 d}{2\pi}\right)}{\left[\left(\frac{\alpha_0 d}{2\pi}\right)^2 + \left(t - \frac{d}{c}\right)^2\right]}$$

This is the equation for the *Impulse Response* $h(t)$. And if we further write $d = 2 \cdot z_0$, where z_0 is the one-way travel time (or depth), then we have :

$$h(\alpha_0, z_0, t) \Rightarrow \frac{A}{\pi} \cdot \frac{\left(\frac{\alpha_0 z_0}{\pi}\right)}{\left[\left(\frac{\alpha_0 z_0}{\pi}\right)^2 + \left(t - \frac{2 \cdot z_0}{c}\right)^2\right]}$$

Appendix B

Discussion of Program for FM Pulse Scheme Simulation

The simulation work for the FM pulse imaging scheme was carried out on an IBM-PC/XT, using a scientific software known as ASYSTANT. The most important part of the simulation was to generate a frequency modulated pulse, which could have varying central frequency and bandwidth. Along with the FM pulse, the program had to fairly accurately simulate the attenuating medium. The equation for the impulse response in attenuating medium has already been discussed. Due to limitations of memory availability on the software, the depth of the medium could not be simulated beyond 6cm. However, by adjusting the equation for attenuation the effective depth could be increased.

1. Frequency Modulated Pulse

The equation for the FM pulse consists of two parts, namely:

- (i) the Quadratic chirp; and
- (ii) the Exponential envelope.

The quadratic chirp, or the FM pulse is written as:

$$\text{Sin}[2\pi(f_b t + bt)^2] \quad (\text{A.1})$$

where f_b is the starting frequency of the pulse which controls the central frequency and b is the sweep rate which affects the bandwidth of the pulse generated. This equation generates

a linear with phase chirp function. The non-linearity of this pulse could make a subject of study, which could have certain advantages for the imaging scheme.

The discrete form of equation §A.1 needs to be evaluated in order to program it. We know that time period $T_o = \frac{1}{f_b}$, where f_b is the frequency. T_o can also be expressed in the discrete form as $T_o = n \cdot \Delta t$ where Δt is the time duration (in μs) between two consecutive points in the signal, and n is the number of points in one cycle. Thus from the two relations for T_o we have:

$$f_b = \frac{1}{n} \cdot \frac{1}{\Delta t} \quad (A.2)$$

Substituting for the discrete terms in equation §A.1 we get:

$$\begin{aligned} & \text{Sin} \left[2\pi \left(\frac{1}{n \cdot \Delta t} \cdot R \cdot \Delta t + b \cdot (R \cdot \Delta t)^2 \right) \right] \\ \Rightarrow & \text{Sin} \left[2\pi \left(\frac{1}{n} \cdot R + b \cdot (R \cdot \Delta t)^2 \right) \right] \end{aligned}$$

Here R is a variable from $1 \rightarrow N$, N (256) being the size of the array to be generated.

So far we have discussed only the first part of the FM pulse equation. The second part consists of the Exponential envelope which is used to modulate the quadratic chirp into the FM pulse. This is done in order to provide more emphasis on the central frequencies of the pulse and less emphasis on the lower and higher end of frequencies. The transducer used to transmit the pulse has its own transfer function, and the one used for the

experiments in this thesis had its driving (peak) frequency around 2.4 MHz. The exponential envelope represents this modulation fairly accurately. For future research purposes the envelope can be varied to any specification as required, to put more stress on a different range of frequencies. The equation used for the exponential envelope is as follows:

$$\exp\left(-\frac{(R-127)^2}{2 \cdot G^2}\right) \quad (\text{A.3})$$

Here also R is variable from 1 → N, N (256) being the size of the array generated. The figure 127 controls the position of the envelope, that being the center of the array in this case. G is a constant which controls the pulse width of the bell-shaped envelope. For our simulations G = 40.0.

To obtain the complete FM pulse we need to take the product of the two parts discussed above, namely the quadratic chirp and the exponential envelope.

The program in ASYSTANT was in a function call F1, and was written as shown below :

```
F1    1> RAD 256 N:RAMP STORE R R
      2> \ SIN(2*PI*((F*0.05E-06)+B*R)*R)
      3> STORE S
      4> \ EXP(-((R-127)^2)/(2*G^2))
      5> STORE T DROP S T * STORE U
```

Here, F is the starting frequency f_b , B represents the sweep rate b , G is the factor controlling the pulse width of the bell-shaped envelope, and R is the variable discussed earlier. The output from this program, was stored in array U , a plot of which is shown below in figure A-1(b).

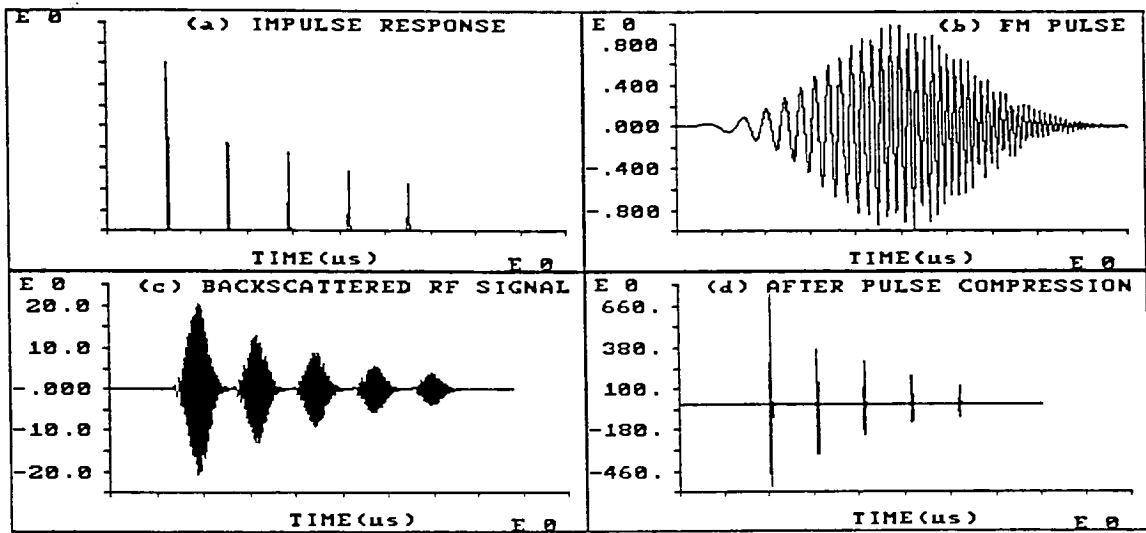


Figure A-1 (a) Impulse response for attenuating medium, (b) FM pulse generated by an ASYSTANT simulation program, (c) Backscattered RF signal & (d) Post processing crosscorrelation step result.

2. Attenuating Medium Impulse Response.

The impulse response of a reflector in the attenuating medium is different from that of one in a non-attenuating medium. For the non-attenuating medium, the impulse response at each reflector is simply a delta function, and as we go deeper into the medium, this

response remains the same, the height of the response depending on the strength of the reflector. But for the attenuating medium case, the impulse response is more complicated. As already discussed in Chapter 3, the response from a reflector will depend on the attenuation coefficient α_0 (which is frequency dependent) of the medium, and the depth z_0 of the reflector in the medium.

The ASYSTANT program used for simulating the attenuating medium impulse response from a reflector was stored in function calls F2 followed by F3, as show below:

```

F2    1> RAD 1500 N:RAMP STORE V V
      2> \ (A*D/PI)
      3> STORE I
      4> \ I/(PI*I^2+(V*.05 - 2*D)/C)^2)
      5> STORE W DROP

F3    1> \ W+X
      2> STORE X

```

Here A represents the attenuation coefficient α_0 , D is the one-way depth (in cm) and V is an array $1 \rightarrow N$. The output is stored in array W. The function F3 is used to add up several impulse responses, from different depths, and store the entire array in X. So finally when both F2 and F3 are run for various depths, the output array X consists of the simulated impulse response of the phantom (or body to be imaged). The output array X is shown above in figure A-1(a).

Now that the FM pulse and the system impulse response have been generated, we can go ahead and convolve the two of them to obtain the backscattered RF signal, which is shown figure A-1(c). If we go one step further and crosscorrelate this RF signal with the input FM pulse, we obtain the final output, which depicts the reflectors in the medium, in their accurate locations in the medium. This result from the post-processing step of crosscorrelation is shown in figure A-1(d). The ASYSTANT program used to perform this last step was stored in function F4 and is shown below:

```
F4    1> U X CONVOLVE STORE Y  
      2> Y U CROSSCORR STORE Z
```

In this function, the result of the convolution of FM pulse (U) and impulse response (X) was stored in array Y. The result of the crosscorrelation was stored in array Z.

In this simulation work, we could vary the parameters of the program to suite our requirements. The attenuation coefficient could be changed by changing the value of 'A', in the program parameters (value was in Np/cm/MHz). The sweep rate b was in 'B' (in MHz) and the starting frequency b was in parameter 'F'. The velocity of sound c was stored in parameter 'C', and the depth of the reflector z_0 was given in cm by the parameter 'D'.

Table B-1 shows the parameter changes required in order to vary the central frequency f_o and bandwidth Δf . The formula used to calculate the central frequency for given b and B is as follows:

$$f_o = B + 2bt$$

So, for instance if we have $B=0.025\text{MHz}$ and $b=0.0002\text{MHz}$ then we get:

$$f_o = 0.025 + \left(\frac{2 \cdot 0.0002 \cdot 128}{0.05} \right)$$

$$f_o = 0.025 + 1.024$$

$$f_o = 1.049$$

and

$$\Delta f = \left(\frac{2 \cdot 0.0002 \cdot 256}{0.05} \right)$$

$$\Delta f = 2.048 \text{ (without cosine envelope)}$$

Tabular values of Δf were evaluated from the power spectrum of the FM pulse (with envelope). Thus, in order to change the value of Δf we only need to change the sweep rate b . And to change f_o we need to vary both starting frequency B and sweep rate b .

Table B-1 Parameter evaluation chart

B (MHz)	b (MHz)	f_o (MHz)	Δf (MHz)
0.025	0.0002	1.049	0.500
	0.0004	2.073	1.020
	0.0006	3.097	1.570
	0.0008	4.121	2.120
1.000	0.0002	2.024	0.500
	0.0004	3.048	1.020
	0.0006	4.072	1.570
	0.0008	5.096	2.120
1.976	0.0002	3.000	0.500
	0.0004	4.024	1.020
	0.0006	5.048	1.570
	0.0008	6.072	2.120
2.976	0.0002	4.000	0.500
	0.0004	5.024	1.020
	0.0006	6.048	1.570
	0.0008	7.072	2.120

Appendix C

Polynomial Waveform Generator

MODEL 2020 (Analogic)

The Polynomial Waveform Synthesizer is used to generate any arbitrary waveform utilizing waveform descriptor language that is arbitrary, universal, and inherently understandable. That language is Algebra. In the ARB (Arbitrary Waveform Generator) mode, "2020" can be linked to a Video Calculator on which the time domain expression in the form $Y = f(t)$ is evaluated and generated as a voltage function of time $V = f(t)$. This mode provides a very powerful method for the generation of essentially any waveform. In order to program the instrument to generate the FM pulse that would be used to drive the transducer, we need to take the following steps:

Step 1: The first step in the process of programming the waveform generator, is to make sure that all the system parameters are set to our requirement. To do this we need enter the OP 2020 mode. In this mode we need to change the setting for the number of solution points. For our purpose, where we require an FM pulse of 20.48 μ s duration, and utilizing a rate of 0.01 μ s per sample point, we require a minimum of 2048 sample points to be generated. We need to set the MAX MEMORY to 2500, in order to generate at least 2048 points, the other parameters can be used with default values, such as CLK SOURCE (clock source) with INTERNAL, and TRIG LEVEL (trigger level) with 1V. In order to do this we use the keypad to type in 2500 <cr> and then hit the RESTORE key.

Step 2 : The next step in our procedure for programming is to input the FM pulse desired. The equation for is adapted from Luke 87, and modified for our purpose. The original equation is as follows:

$$\text{FOR } 20\mu 5*(0.5 - 0.5*\text{COS}(t/20\mu)) * \text{SIN}(A*t + K*t*t/20\mu)$$

$$\text{FOR } 180\mu 0 \text{ FILT } 15\text{M}$$

Using this equation gives us an FM pulse for 20 μ s duration, and then a waiting period of 180 μ s, to record the backscattered signal (echo). It also uses a low pass filter of 15 MHz cutoff. This equation is controlled by two parameters, those being the starting frequency A and the sweep rate K, which can be set to desired specifications. For our experimental purpose, we would like to be able to control the FM pulse equation by varying the central frequency and bandwidth. In order to do this we modify the above equation as follows.

$$\text{CHIRP} = \text{SIN}[2\pi(At + \frac{Kt^2}{2})]$$

is the equation for the FM pulse, where

$$\Phi = 2\pi(At + \frac{Kt^2}{2})$$

is the phase term. In order to obtain the instantaneous frequency we need to differentiate Φ with respect to t. This gives us

$$f_i = \left(\frac{1}{2\pi}\right) \cdot \frac{d\Phi}{dt} = A + K \cdot t$$

In order to evaluate the equation in terms of central frequency f_0 and bandwidth Δf we keep A constant at 1 MHz, and vary K. This way we will get a different FM pulse for each K, of which we will then obtain the f_0 and Δf , by evaluating the amplitude part of Fourier Transform. The results obtained are quantified in Table C-1.

Table C-1 Evaluating FM pulse equation for f_0 and Δf

A=1MHz	K(Mhz)	f_0 (MHz)	Δf (MHz)
	1.0	2.0264	0.9765
	1.5	2.4658	1.4648
	2.0	2.8809	1.9287
	2.5	3.4424	2.4424
	3.0	3.9551	2.8076

On plotting (1) f_0 against K and (2) Δf against K , and doing a linear goodness of fit for both cases we get the following two equations:

$$f_0 = (0.9668)K + 1.02052 \quad (C.1)$$

$$\Delta f = (0.92776)K + 0.0680 \quad (C.2)$$

where 0.9668 and 0.92776 are the slopes for equations §C.1 and §C.2 respectively, and 1.02052 and 0.0680 are the y-intercepts. From C.2 we have

$$\boxed{K = \left(\frac{\Delta f - 0.0680}{0.92776} \right)} \quad (C.3)$$

and substituting for K in C.1 gives us

$$f_o = (0.9668) \cdot \left(\frac{\Delta f - 0.0680}{0.92776} \right) + 1.02052$$

On comparing this with the equation for instantaneous frequency $f_i = A + Kt$, we have $A = 1.02052$ ($\approx 1\text{MHz}$). Rearranging the equation gives us

$$\boxed{A = f_o - (1.04208) \cdot (\Delta f - 0.068)} \quad (C.4)$$

Now we can use equations §C.3 and §C.4 to replace the terms A and K in the original FM pulse equation, to come up with our own version.

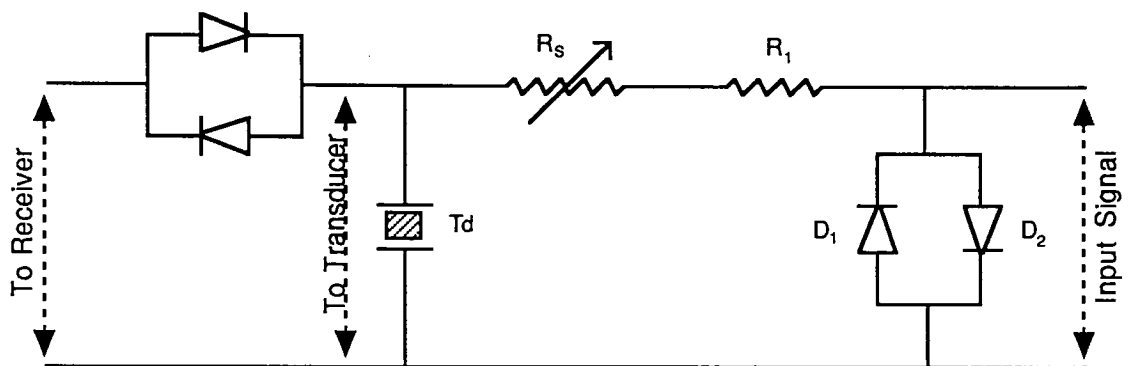
$$\begin{aligned} & \text{F204 =FOR } 20\mu \text{ (} 0.5 - 0.5 \cdot (\text{COS}(t/20\mu)) \text{) } * \\ & \quad \text{SIN}(\text{((} f_o - (1.04208 * (\Delta f - 0.068)) + (((\Delta f - 0.068)/0.92776) * (t * t)/20\mu))) \\ & \text{FOR } 180\mu \text{ 0 FILT } 15\text{M} \end{aligned}$$

This is the equation which was programmed into the waveform synthesizer, in order to generate an FM pulse, used to drive the transducer.

Once the above two steps have been followed, we need to put the instrument in RUN mode, and this computes the signal for us. The output can be observed on an analog oscilloscope, or sent to a digital oscilloscope (such as the Data 6000, discussed in Appendix G), which has the ability to perform certain digital signal processing algorithms, such as an FFT on the signal. Here we can obtain the power spectrum of the FM pulse, and can make sure that the central frequency and bandwidth of the signal are as desired (same as the input to the FM pulse equation).

Appendix D

Transmitter-Receiver Circuit



Td : Transducer
D1, D2 : Cutoff diodes
R1 : 270 Ω resistance
Rs : Variable resistance

Appendix E
Table for Transducer Transfer Function Measured
with a Hydrophone

Transducer Type : Panametrics unfocussed immersion.

Hydrophone Position : 9.1 cm from transducer (Far field) in water.

Input Signal : Sinusoidal wave.

Input Amplitude (constant) : 0.2V (peak-to-peak).

Table E.1 Transducer response chart

Input Frequency (MHz)	Output Amplitude (Volts)
0.2	0.568
0.4	0.837
0.6	1.644
0.8	1.554
1.0	1.734
1.2	2.542
1.4	2.751
1.6	3.109
1.8	3.439
2.0	4.306
2.2	5.023
2.4	5.442
2.6	4.754
2.8	3.644
3.0	2.599
3.2	1.613
3.4	0.985

Input Frequency (MHz)	Output Amplitude (Volts)
3.6	0.538
3.8	0.358
4.0	0.418
4.2	0.508
4.4	0.538
4.6	0.478
4.8	0.418
5.0	0.299
5.2	0.149
5.4	0.090
5.6	0.120
5.8	0.120
6.0	0.150
6.2	0.299
6.4	0.448
6.6	0.388
6.8	0.269

Appendix F

Analogic Corporation Dual Pre-Amp

The calibration of the pre-amp was done using a sinusoidal input of constant amplitude. The scales were varied one by one and the following table was generated.

Table F-1 Calibration of the dual pre-amp

Scale	Input voltage (constant) Volt	Output voltage Volts	Amplification factor
0.05	0.2	7.600	x 38.00
0.10	0.2	3.800	19.00
0.20	0.2	2.000	10.00
0.50	0.2	0.760	3.80
1.00	0.2	0.380	1.90
2.00	0.2	0.200	1.00
5.00	0.2	0.075	0.38
10.00	0.2	0.040	0.20
20.00	0.2	0.020	0.10

Appendix G

Analogic Corporation Data 6000

In order to obtain an image from any analog signal, we need to be able to digitize it. To do this we need an analog-to-digital (A/D) device, which would store our signal, and give us the flexibility to perform various signal processing algorithms on this digitized signal. The Data 6000 is an instrument which includes a digital oscilloscope, an A/D convertor and has the ability to perform DSP (Digital Signal Processing) on the analog input, from our backscattered RF signal. It is a very powerful tool for performing analysis in any signal processing application.

The Data 6000 was extensively used as part of the experimental work for this thesis. The object of this appendix is to briefly give an overview as to how to get started on the instrument, and some of the programming that was utilized, to make life much easier for the user.

The Data 6000, in conjunction with the Floppy Disk Drive (Model 681) have a total of 5 keypads, namely

- (1) Display keypad
- (2) Function keypad
- (3) Mainframe keypad
- (4) Plug-in keypad
- (5) Disk Drive keypad

we will briefly discuss each one of them here.

(1) The Display Keypad : This keypad consists of 5 fields with 4 soft keys each. Each field corresponds to a certain parameter on the display. It is very much interactive, as the display parameter shows up right above the field keys, and the user can easily change the desired parameters.

(2) The Function Keypad : This keypad consists of 45 softkeys, each one of which has either 1, 2 or 3 functions. The labels in black are the ones that are directly operable by depressing the softkey. In order to use the blue label of a softkey, one has to first press the blue function (f) key, which changes the mode of the softkey from the one in black label to the one in blue label. Similarly the green label is operable when the green alpha (α) key is first used. So by using various combinations, one can use this keyboard as a typewriter keypad, or use the editor mode functions, or the signal processing functions available which give scalar (example mean, pulsewidth, etc.) as well as vector (example FTT, correlation etc.) outputs.

(3) The Mainframe keypad : This keypad consists of functions which effect the display of the digital oscilloscope. Changing parameters within these functions does not effect the stored arrays in any way.

X : This key sets up the display softkeys to change parameters in the x-axis of the input signal. Among other things, it can be used to scale the display. It can also be used to scroll through the array.

Y : This key has the same usefulness as the X key, except for the fact that it effects the display in the Y direction instead of the X.

DISP : Display format menu. This key allows us to choose the number of traces we want to display at one time (1 to 4). It allows us to overlap two or four arrays, to compare them on the same scale. The softkeys on the display keypad allow us to change the array being displayed on the screen.

MARK : Controls for the cursor, baseline, grid and crosshair.

DIR : This key allows us to go into the directory of either the system, drive A or B and get information about each file by switching the Expand ON. Out here we can also delete files from the directory. Pressing this key twice lets the user create control, program and dataset files.

PROG : This mode is used to create, edit and execute a program. In this mode we have the ability to program any desirable function, or instruct the system to run a given key (which could include any key from all 5 keypads), by simply entering the keys mnemonic code (For mnemonic codes please refer to the Data 6000 manual pg. F6-89).

OPT : This key consists of various sub-functions, for controlling the configuration of the Input/Output devices (RS232, GPIB, etc.), and the plotter commands.

I/O : This key provides on-line help on all the keys in the 5 keypads.

X & Y : Pressing the two keys together allows us the flexibility to change the scale in the X and Y directions on the same display keypad.

DISP & MARK : Panel control menu. These keys, pressed together allow us to vary the intensity level of the display screen, and use the clock to set the time and date.

DIR & PROG : Remote control parameter menu.

OPT & I/O : This menu gives the user the ability to define soft key actions from a remote controller. It can also be used to label the display from a program.

(4) **Plug-in Keypad** : This keypad consists of keys which control the plug-in parameters, which directly effect the array that is being digitized.

BUFR : Buffer control menu. Sets up the input channels associated with Timebase A or B.

PROC : Processing menu. This mode allows per-acquisition averaging on the collected data.

TMB : Time base menu. Allows user to control such parameters as the sampling rate of the signal, the array size to be computed and the delay in the signal.

TRIG : Trigger menu. Allows the user to define the type of trigger the signal should use, and the source of the trigger (external, line, channel 1 or 2).

INP : Input menu. It controls such parameters as the range of the input signal (example $\pm 1.2\text{V}$ or $\pm 3.6\text{V}$).

FLTR : Filter menu. Uses a fixed filter of -3dB at 20 MHz.

ARM : Arm plug-in. It enables the plug-in to look for the trigger condition.

DARM : Disarm key. Disables plug-in acquisitions.

(5) Disk Drive Keypad: This keypad consists of keys which act on the floppy disks.

DISK : Disk specific controls, such as formatting.

XFER : Transfer setup menu. This allows the user to transfer files in either direction (System \rightarrow Drive or Drive \rightarrow System).

DIR : Same as main keypad "DIR" function.

Once the FM pulse has been generated, and the backscattered signal from the phantom is coming back into the Data 6000, we need to store this entire raw data, as well

as perform the post-processing step of crosscorrelation with the input FM pulse. In addition we also need to perform envelope detection of this crosscorrelated data, in order to convert it into a gray scale image later on.

The input FM pulse loaded onto Timebase A, was used with a length of 1024 points, at a time period of 20 ns (sampling rate of 50 MHz), which gave it a time duration of 20.48 μ s. The backscattered signal which consisted of one A-scan through the phantom was stored for 8192 points at a time period of 20 ns ($8192 \times 20\text{ns} = 163 \mu\text{s}$), with a time delay of 37 μ s, in order to avoid the high voltage echo from the input pulse. This enabled us to view about 12.60 cm (two-way travel time = 13 $\mu\text{s}/\text{cm}$ @ $c = 1540 \text{ m/s}$) deep into the phantom.

The D.C. term was removed from this backscattered signal, and then it was cross-correlated with the original input FM pulse. This was done for an evaluation length of 512 points about each scatterer (2nd, 3rd and 5th) separately, to make the processing faster. The result of cross-correlation was then envelope detected using a convolution triangular kernel of width 32 points. The process of correlation was fairly complicated. If one gives the offset to be 0 and evaluation length 512, then the instrument evaluates the cross-correlation with the peak as the first point, and then the 511 points, by shifting the correlator FM pulse one point at a time to the right. In order to get a symmetric correlation output, we need to give a shift of -256 to the correlator, so that the peak would lie in the center of the 512 array.

First of all, all the backscattered raw data was stored onto floppy drives, in order to save a hard copy of the experimental data. Then the correlation and envelope detection was performed on these backscattered signals which had to be transferred back onto the Data 6000 one by one. Certain prerequisites were required in order to run the program which would do the correlation and envelope detection. First of all the FM pulse had to be stored in array BUF.X0. Then the backscattered signals were transferred one by one into array BUF.X1. Once these prerequisites were met, the program was run in the RUN/STOP mode.

The program PRG.X1 to perform the entire stage of post-processing is shown below here :

```
10 NEW.X0 = BUF.X0
20 NEW.X1 = BUF.X1 - MEAN(BUF.X1)
                                     ...removes DC term
30 CCORX1 = CORR(NEW.X1,NEW.X0,1,-256,512,0)
                                     ...crosscorrelation step
40 SQ.X1 = SQ(CCORX1)
                                     ...square correlated data
                                     ...enables envelope detection
50 FLTRX1 = CONV(SQ.X1,,0,1,32,0)
                                     ...triangular convolution kernel used
60 DISP
70 TRCSRC(1) = CCORX1
                                     ...puts correlated array in 'Trace 1'
```

80 TRCSRC(2) = FLTRX1

...puts enveloped array in 'Trace 2'

90 KEY = 5004

...activates 'XFER' key

100 KEY = 1016

...activates 'Direction' top-left key

...sets arrow (system→ drive)

110 KEY = 1034

...activates 'Volume' bottom-left key

...sets it to 'B:' for floppy drive B

120 KEY = 1058

...activates 'File' top-bottom-left keys

...creates new file in disk B:

130 KEY = 1066

...activates 'Enter' top-left key

...transfers file from system to drive

140 KEY = 1002

...activates 'Sys-file' top-left key

...scrolls up to different file name

150 KEY = 1002

160 KEY = 1058

170 KEY = 1066

180 KEY = 1004

...activates 'Sys-file' bottom-left key

...scrolls down to different file name

190 KEY = 1004

200 KEY = 1004

210 KEY = 1017

...activates 'Direction' top-right key

...sets arrow (system ← drive)

220 KEY = 1033

...activates 'Volume' top-left key

...sets it to 'A:' for floppy drive A

...at this stage the user has to input a different file name (one of scan 1-28)

and run the program again (the loop is followed 28 times)

Appendix H

Program for Converting Data6000 Format to ASCII

```

10  *UNPLI.DMS
20  '
30  'CONVERTS .VAR FILES CREATED BY D6000 INTO REAL NO. FILES AND PLOTS ON THE
SCREEN
40  '
50  'ORIGINALLY WRITTEN BY DOUGH ESTRICH 7/23/05 @ DATA PRECISION
55  'MODIFIED BY SUMAT MEHRA 10/25/90 @ R.I.T.
60  '
70  'READS REV. 4.0 FILES FROM D6000
80  'USES PCDOS 2.0 OR LATER AND IBM PERSONAL COMPUTER BASIC VERSION D2.00
90  '
100  KEY OFF:KEY 10, "SYSTEM"+CHR$(13):PS$=" +###.#####"
110  DIM XYNAME$(4):XYNAME$(1)="X PER POINT = ":XYNAME$(2)="X OFFSET ="
120  XYNAME$(3)="Y FS RANGE = ":XYNAME$(4)="Y OFFSET ="
130  DIM UNIT$(4):UNIT$(0)=" NONE":UNIT$(1)=" SEC":UNIT$(2)=" VOLTS"
140  DEFINT A-Z
150  DEFDBL M:DEFSNG F
160  '
170  INPUT "WHAT DRIVE ARE THE FILES IN";D$:FILES D$+":"
180  INPUT "WHAT .VAR FILE DO YOU WANT TO SEE "; FLNAME$
190  '
200  ' READ THE FIRST BLOCK OF 126 BYTES FROM DISK
210  OPEN D$+"."+FLNAME$+".VAR" AS #1
220  GET #1:FC=VARPTR(#1):XUNIT=PEEK(FC+202):YUNIT=PEEK(FC+203)
230  '
240  'CALCULATE FILE SIZE AND X AND Y UNITS - PRINT THEM OUT
250  FLSIZE=LOF(1)-36:IRMAX=FLSIZE/128
260  NPTS=FLSIZE/2:DIM C(NPTS):CIMN=32767:CMAX=-32768!
270  DIM FARRAY(NPTS)
280  MMIN=100:MMAX=-100
290  PRINT "TOTAL # OF DATA POINTS=";NPTS:IC=0
300  PRINT "X UNITS      =";XUNIT;:PRINT UNIT$(XUNIT)
310  PRINT "Y UNITS      =";YUNIT;:PRINT UNIT$(YUNIT)
320  '
330  'READ THE HEADER INFORMATION AND TRANSLATE IEEE FP TO REAL NUMBERS
340  FOR I=0 TO 3
350  X=I*4
360  A=PEEK(FC+204+X):B=PEEK(FC+205+X):C=PEEK(FC+207+X)
370  IF A=0 AND B=0 AND C=0 AND D=0 THEN FP=0:GOTO 420
380  S=A AND 128
390  E=(A AND 127)*2+(B AND 128)/128-127
400  M=((B AND 127)+128)*2^16+C*2^8+D)/2^23
410  FP=(-1)^S*2^E*M:IF I=2 THEN FSR=FP
420  PRINT XYNAME$(I+1);FP
430  NEXT I
440  '
450  'READ DATA AND TRANSLATE TO REAL NUMBERS - LOAD INTEGERS INTO C FOR PLOT
460  ' AND INTO FARRAY FOR USE AS DESIRED
470  PRINT "GETTING THE DATA - PLEASE WAIT"
480  ICOUNT=0
490  FSF=FSR/2^16
500  FOR IR=1 TO IRMAX+1
510  IF IR=1 THEN IMIN=36:GOTO 530
520  GET #1,IR:FC=VARPTR(#1):IMIN=0
530  FOR I=IMIN TO 126 STEP 2
540  A=PEEK(FC+188+I):B=PEEK(FC+189+I)
550  M=A*256+B
560  IF M>32767 THEN M=M-65535!
570  MVAL=M*FSF
580  IF MVAL<MMIN THEN MMIN=MVAL
590  IF MVAL>MMAX THEN MMAX=MVAL
600  FARRAY(ICOUNT+1)=MVAL
610  C(ICOUNT+1)=100-INT(M/300)
620  IF C(ICOUNT+1)<CMIN THEN CMIN=C(ICOUNT+1)
630  IF C(ICOUNT+1)>CMAX THEN CMAX=C(ICOUNT+1)

```

```

640   ICOUNT=ICOUNT+1
650   IF ICOUNT>NPTS-1 THEN 680
660   NEXT I
670   NEXT IR
680   '
690   'PRINT DATA IF DESIRED
700   INPUT "DO YOU WANT A LISTING OF THE DATA? (Y OR N) ",A$
710   IF A$="N" OR A$="n" THEN 760
720   FOR I=1 TO NPTS
730   PRINT I,FARRAY(I)
740   NEXT I
750   '
760   'PUT DATA IN FILE IF DESIRED
770   PRINT ""
780   INPUT "DO YOU WANT TO PUT THE DATA IN A FILE? (Y OR N) ",A$
790   IF A$="N" OR A$="n" THEN 860
795   INPUT "WHAT .DAT FILE DO YOU WANT TO CREATE? ";FLNAME$
800   OPEN "O", #2, FLNAME$+".DAT"
810   FOR I=1 TO NPTS
820   PRINT #2, FARRAY(I)
830   NEXT I
840   CLOSE #2
850   '
860   'PLOT DATA IF DESIRED
870   PRINT ""
880   PRINT "THE IBM CAN ONLY PLOT 640 PTS. HORIZONTALLY THEREFORE"
890   PRINT " ONLY THE FIRST 640 PTS. OF THE DATA RECORD WILL BE PLOTTED."
900   PRINT ""
910   INPUT "DO YOU WANT A PLOT OF THE DATA ? (Y OR N) ";A$
920   IF A$="N" OR A$="n" THEN 1070
930   SCREEN 2
940   KEY OFF:CLS:LOCATE 1,1:PRINT "                                ",FLNA
950   YMIN=CMIN*FSF:YMAX=CMAX*FSF
960   LOCATE 2,1:PRINT "                                NPTS=";N
970   LOCATE 3,1:PRINT "                                YMIN=";:
980   LOCATE 4,1:PRINT "                                YMAX=";:
990   FOR I=2 TO NPTS
1000  IF I>640 THEN 930
1010  LINE (I-1,C(I-1))-(I,C(I))
1020  NEXT
1030  BEEP
1040  CLOSE #1
1050  LOCATE 23,1:PRINT "HIT ANY KEY TO EXIT-PROGRAM"
1060  A$=INKEY$:IF A$="" THEN 960 ELSE 970
1070  END
OK

```

Appendix I

Program for Converting A-Scan data to a B-Scan Image

```

*****
*
*           CONVERT.C
*
*   This program assembles the various A-line RF scans into a B-scan
*   gray scale image. It takes care of the end-of-line control
*   character, and also samples the data (twice or thrice) as desired
*   by the user. Due to the display limitation of 512x512 using the
*   Deanza Gould system (on VAXIMG), this sampling needs to be done
*   for the larger data.
*
*   Input File : The input file type should be ASCII.
*   Output Files : (1) The first part of the program is to assemble the
*   A-line data into a B-scan, which can be outputed as a .dat file.
*   (2) The second part of the program is to convert the ASCII B-scan
*   file into an 8-bit gray scale image (.pic file).
*   Program to add an index column to the data from the digitizer.
*
*   Written by : Sumat Mehra           October 1990
*
*****

#include <stdio.h>
#include <stdlib.h>
#include <math.h>

FILE *fpin, *fpout_vax, *fpout_gray;

main()

    int i,k,j,l,N,sample,choice;
    float index[8192];
    float data[8192];
    char vaxoutfile[80];

    printf("Enter the number of files (to add) ::");
    scanf("%d",&N);

    printf(" [1] ADD INDEX.\n [2] REMOVE INDEX.\n [3] GRAY SCALE.\n");
    printf(" [4] EDIT CONTROL CHAR, THEN ADD FILES WITH INDEX.\n");
    printf(" choice :: > ");
    scanf("%d",&choice);

    if( choice == 1 ) {
        printf("For sampling twice enter 2, thrice enter 3 else 0 ::");
        scanf("%d",&sample);

        if(sample == 2) {
            OutputFile();
            for(k=1;k<=N;k++){
                j=k-1;
                InputFile(k);
                i=0;
                while( !feof(fpin) ) {
                    fscanf(fpin,"%f\n",&data[i]);
                    if((fmod(i,2.0))==0.0){
                        printf(fpout_vax,"%d %d %f\n",j,i/2,data[i]);
                    }
                    i++;
                }
            }
        }
    }

```

```

        fclose(fpin);
    }
}

else if(sample == 3) {
    OutputFile();
    for(k=1;k<=N;k++){
        j=k-1;
        InputFile(k);
        i=0;
        while( !feof(fpin) ) {
            fscanf(fpin, "%f\n",&data[i]);
            if((fmod(i,3.0))==0.0){
                fprintf(fpout_vax, "%d %d %f\n",j,i/3,data[i]);
            }
            i++;
        }
        fclose(fpin);
    }
}

else {
    OutputFile();
    for(k=1;k<=N;k++){
        j=k-1;
        InputFile(k);
        i=0;
        while( !feof(fpin) ) {
            fscanf(fpin, "%f\n",&data[i]);
            fprintf(fpout_vax, "%d %d %f\n",j,i,data[i]);
            i++;
        }
        fclose(fpin);
    }
}

}

else if(choice == 2) {
    InputFile(1);
    OutputFile();
    i=0;
    while( !feof(fpin) ) {
        i++;
        fscanf(fpin, "%f %f\n",&index[i], &data[i]);
        fprintf(fpout_vax, "%f\n",data[i]);
    }
    fclose(fpin);
}

else if(choice == 3) {
    GrayScale(N);
}

else if(choice == 4) {
    printf("Input array length\n");
    scanf("%d",&l);

    OutputFile();
    for(k=1;k<=N;k++){

```

```

        j=k-1;
        InputFile(k);
        for(i=0;i<l;i++) {
            fscanf(fpin,"%f\n",&data[i]);
            if((fmod(i,3.0))==0.0){
                fprintf(fpout_vax,"%d %d %f\n",j,i/3,data[i]);
            }
        }
        fclose(fpin);
    }
}
fclose(fpout_vax);

```

*****/

InputFile(int t)

```

    char infile[80];

    printf("Enter input file %d name ::",t);
    scanf("%s", infile);

    if((fpin=fopen(infile,"r")) == NULL) {
        printf("Error opening input file\n");
        exit(0);
    }

```

*****/

OutputFile()

```

    char vaxoutfile[80];

    printf("Enter vaxoutput file name ::");
    scanf("%s", vaxoutfile);

    if((fpout_vax=fopen(vaxoutfile,"w")) == NULL) {
        printf("Error opening vax_output file\n");
        exit(0);
    }

```

*****/

GrayScale(int t)

```

    int m,n,i,total,length;
    char ans;
    char infile[80], vaxoutfile[80];
    float maxi, mini, value[57344];

    InputFile(1);

    printf("Enter vaxoutput file name ::");
    scanf("%s", vaxoutfile);
    if((fpout_gray=fopen(vaxoutfile,"wb")) == NULL) {
        printf("Error opening output file\n");
    }

```

```

        exit(0);
    }

    printf("Enter length of each scan line ::");
    scanf("%d",&length);

    total = t*length;

    for(i=0;i < total;i++){
        fscanf(fpin,"%d %d %f\n",&m,&n,&value[i]);
    }
    maxi = -100000.0;
    mini = 100000.0;
    for(i=0;i < total;i++){
        if(value[i] >= maxi){
            maxi = value[i];
        }
        if(value[i] <= mini){
            mini = value[i];
        }
    }
    for(i=0;i < total;i++){
        value[i] = (((float) ((value[i]-mini)/(maxi-mini)))*255));
        fprintf(fpout_gray,"%c",(unsigned char) value[i]);
    }

```

***** END *****/

Appendix J

ULTRASOUND SPECKLE STATISTICS VARIATIONS WITH IMAGING SYSTEMS IMPULSE RESPONSE

Navalgund Rao, Sumat Mehra and Hui Zhu

Center for Imaging Science - Rochester Institute of Technology - Rochester, NY 14623

ABSTRACT

The statistics of speckle depends on the density of scatterers and the resolution cell volume. The resolution cell volume depends on the impulse response of the imaging system. A fully developed speckle results from interference of scattered waves from a high density of random scatterers within a resolution cell volume. In such cases, the envelope detected signal is known to possess a Rayleigh distribution and a signal to noise ratio (SNR) of 1.91 whereas the intensity signal has a limiting SNR value of 1. Previous publications have shown that SNR can drop below this value when scatterer density departs from high density limit. It has been suggested that SNR be used as a tissue characterization parameter. In this paper, we show that a similar behavior can be observed when resolution cell volume is varied for a fixed scatterer density, and demonstrate its usefulness in tissue characterization. A three dimensional (3D) simulation phantom that takes into account 3D distribution of scatterers and the 3D nature of resolution cell volume, has been used. The medium is modeled as a uniform matrix material with discrete scatterers distributed randomly. Envelope detection from the simulated RF signal is carried out using Hilbert transform. Several simulations were performed to study the effect of scatterer number density (n) and the resolution cell volume on the SNR.

We report results with several major implications: (i) It is the number of scatterers within a resolution cell volume that determine the high density limiting behavior. We find this number to be around 10 for a full width at half maximum analysis of the resolution cell volume. (ii) A plot of SNR vs. resolution cell volume of the imaging system for various scatterer number densities reveals the sensitivity of different systems for tissue characterization. (iii) If we have the information about the system's resolution cell volume, then the scatterer number density can be estimated from the SNR measurements. (iv) Higher order moments can be more useful in number density estimation. But our analysis shows that higher moments are even more sensitive to variations in resolution cell volume.

INTRODUCTION

Speckle patterns in imaging systems such as ultrasound B-scans are classically interpreted as the result of coherent summation of responses from a large number of scattering targets. The central limit theorem can then be invoked: the RF signal amplitude exhibits a gaussian distribution from which a Rayleigh distribution is deduced for signal envelope and an

exponential distribution for signal intensity [1]. The signal-to-noise ratio (SNR), defined as the ratio of the mean to standard deviation of the distribution, then reaches a limiting value of 1.91 for signal envelope and 1.0 for signal intensity. In this, so called Rayleigh limit case, parameters derived from the first order statistics of the signal, such as SNR, become independent of the imaging system parameters and the scatterer density. However, if the mean distance between scatterers is not neglectable with respect to the resolution-cell size of the imaging system, the scatterer density cannot be considered "very large" any more. The speckle statistics will depend on the scatterer distribution and the resolution cell size of the system. Based on this behavior, it has been suggested that parameters derived from speckle statistics may be useful for tissue characterization, provided we are below the Rayleigh limit [2,3].

This limit can be reached, either by changing scatterer number density or the resolution cell volume. In a tissue characterization problem, the former is not under our control, but the later depends on the imaging system and hence could be adjusted. Although the influence of resolution cell size has been appreciated before, its usefulness has not been evaluated [4]. This paper is devoted to the study of the effects of resolution cell size on the speckle statistics below the Rayleigh limit. Simulations that take into account the 3D nature of imaging, have been performed to generate A-line data. Analysis of speckle statistics was carried out on this data.

THE 3-DIMENSIONAL POINT SPREAD FUNCTION

In dealing with ultrasound speckle, the concepts and tools of System Theory are currently used. The image formation is usually modeled as the superimposition of responses from point scatterers which are considered as the "excitation" of a system described by its (possibly varying) impulse response. The A-line signal is one-dimensional in nature and allows the construction of a two-dimensional B-scan image. However it should not be forgotten that the physical phenomena take place in the "real space", known to be three-dimensional. The tissues and their echo-generating structures have a spatial extent and no transducer can exactly focus the ultrasound wave on a line or a plane. This is why the impulse response characterizing an echographic system should have a 3D spatial dependence on the target position. Figure 1 describes the concepts for a circular element transducer. Z is along the central axis of the transducer and time $t = 2Z/c$ encodes the depth of the reflector, where c is the speed of sound in soft tissue. The radially symmetric point spread function (PSF) is

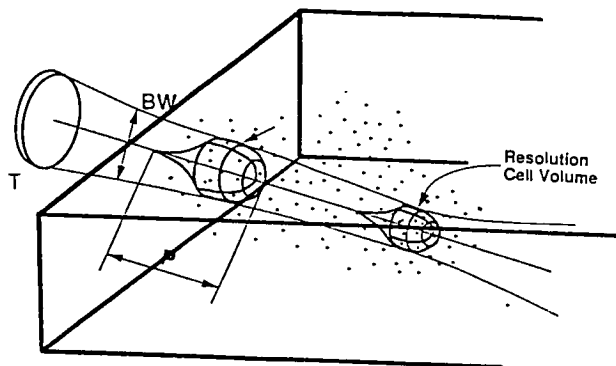


FIGURE - 1

then defined as the signal received by the imaging system, $h(r,z)$, in response to a scatterer located at (r,z) . Here r refers to the radial distance from the central axis. When many scatterers are present, the resultant response is a weighted sum of responses from each scatterer. The weighing is the scattering strength of the scatterer at that location.

A-Line RF signal:

$$m(z) = \sum_i w_i h(r, z) \quad ; \quad z = \frac{t}{2c} \quad (1)$$

However, in B-scan imaging the RF signal under goes an envelope detection. This non-linear processing is given a simple mathematical expression if the analytic signal is used instead of the real signal since the envelope of the RF signal is just the modulus of the complex signal. The intensity is then the squared modulus of envelope detected signal, and therefore we can also define an intensity PSF as $|h(r,z)|^2$.

The PSF of the imaging system we have considered can be written as a product of two components: $h(r,z) \equiv h(r,t) = B(r) \cdot h(t)$, where $B(r)$ describes the beam profile in the transverse direction and $h(t)$ is the interrogating pulse shape that describes the resolution in the axial or z direction. The 3-dimensional resolution cell volume is defined by a surface where the PSF falls to a certain fraction of its maximum value. PSF in ultrasonic imaging is not shift invariant. If we assume that our region of interest is small (2 cm in z direction) and is located in the far field of the transducer, then we can approximate the PSF as shift invariant and also calculate the beam profile $B(r)$ from the transducer and pulse parameters. We further assume that the beam profile depends only on the center frequency f_0 of the pulse and the envelope of $h(t)$ is gaussian and therefore depends only on the frequency bandwidth Δf of the pulse. In this study, we have varied f_0 and Δf over a range of frequencies, incorporated its effect on the simulated RF signal and finally performed analysis on the envelope detected signals.

THEORETICAL SIMULATION

We have used a computer model described by Kuc et. al [5] for simulating reflected signals from a three dimensional random

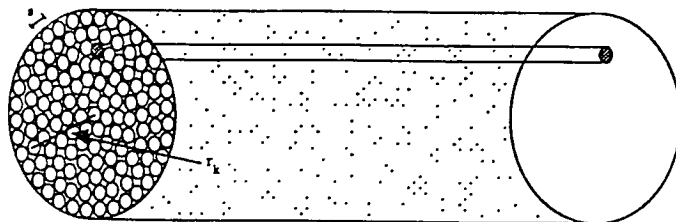


Figure - 2

medium. The algorithm has been modified to incorporate change in resolution cell volume as a function f_0 and Δf . The simulation model is composed of a transducer model and that of the medium. The former provides a description of the field of view, while the latter specifies the probability laws governing the random scatterer amplitude and location.

TRANSDUCER MODEL

We consider clinical transducer having circular aperture. The impulse response of the system at a range z and distance r from the axis is denoted by $h(r,t)$. We are interested in generating A-line signal coming from 3 dimensional tissue located at a range z_0 . The beam pattern is denoted by $B(r,z_0)$, and it is assumed to possess radial symmetry. The field of the transducer is partitioned into set of cylinders or microbeams which are parallel to the axis of the transducer, as shown in Fig. 2. The diameter of the microbeams is determined by the mean spacing of the scatterers, S .

STOCHASTIC MODEL OF RANDOM SCATTERERS

The tissue was modeled as a set of scatterers that have random scattering strengths and are randomly located within each microbeam. The microbeam approximation constrains the separation between the independent spacial sequences to be approximately equal to the mean spacing S . This allows the use of one dimensional probability function to describe the random spacing in 3 dimensions.

w_n , the scattering strengths of the scatterers, follow a Gaussian probability function with zero mean and standard deviation 0.5. Within each microbeam the distance between scatterers $j-1$ and j was also a random variable, with an exponential probability density function with a mean value of S .

Governed by these two probability laws, we generate the reflector sequence from the j th microbeam in the k th annulus, denoted by $m_{k,j}(t)$.

$$m_{k,j}(t) = \sum_{n=1}^{N_m} w_n \delta(t - t_n) \quad (2)$$

Assuming that the detection process of the transducer is linear, the total reflected signal is equal to the sum of the contributions from each microbeam. Since the microbeams within a given annulus are equidistant from the axis, their reflector sequences can first be added and then the annular sum

can be convolved with the reflector impulse response of the transducer appropriate for the given annulus. The composite reflection sequence $m_T(t, z_0)$ is then equal to

$$m_T(t, z_0) = \sum_{k=1}^{N_a} \left(h(r_k, z_0, t) * \sum_{j=1}^{N_m} m_{k,j}(t) \right) \quad (3)$$

where $*$ stands for convolution.

N_a and N_m are the number of annulus and number of microbeams in each annulus, respectively. Because of the radial symmetry we can write the impulse response $h(r_k, z_0, t)$ as $B(r_k, z_0) \cdot h(t)$, where $B(r_k, z_0)$ is the relative value of the beam pattern at radius r_k and $h(t)$ is the interrogating pulse.

$$m_T(t, z_0) = h(t) * \sum_{k=1}^{N_a} B(r_k, z_0) * \sum_{j=1}^{N_m} m_{k,j}(t) \quad (4)$$

We make an approximation here that the frequency content of the incident pulse does not change across the beam, only its amplitude varies and we call this variation, the beam pattern $B(r_k, z_0)$. In the Fraunhofer zone, $B(r_k, z_0)$ can be approximated by Bessel function.

$$\frac{J_1(x)}{x} \quad \text{where } x = \left(\frac{2\pi f_0 \cdot d \cdot r}{c \cdot z_0} \right) \quad (5)$$

where d is the diameter of the transducer.

Finally, considering $m_T(t)$ as the real part of a complex analytic signal, we can compute the envelope signal $A(t)$ by a sum using Hilbert transform, $\hat{m}_T(t)$:

$$A(t) = |m_T(t) + j \hat{m}_T(t)| \quad \text{and Intensity signal} = A^2(t) \quad (6)$$

IMAGING PULSE AND TISSUE MODEL PARAMETERS

The parameters of the interrogating pulses used in simulation are summarized in Table 1. Seven different combinations of center frequency f_0 and the full width at half maximum (FWHM) bandwidth Δf , were used. Each pulse has been labeled by a symbol A through G. The pulse width and beam width

(both FWHM) for each pulse is also tabulated along with the estimate of resolution cell volume. This volume was computed for a cylinder with radius equal to one half of beam width and height equal to one half of the pulse width. Three different tissue models were considered. In each model, the scattering strength w_n was a random variable with a zero mean gaussian distribution and standard deviation of 0.5. The scatterer spacing was also a random variable with exponential distribution, but the difference in the models was in terms of the mean value of spacing, S . It was 0.23 mm, 0.3 mm and 0.55 mm for model 1, 2 and 3 respectively. These numbers were chosen because they reflect the range in which we expect to see textural changes in soft tissue due to pathology. Due to the bandwidth limitation of the clinical PZT transducers, it may not be possible, with a single transducer, to generate all the 7 types of pulses used in this study. We are currently investigating the use of PVDF transducers driven with a frequency modulated pulse [3]. The details of the technique have been published elsewhere and will not be repeated here [6]. With such a technique, it would be possible to utilize the broad bandwidth of PVDF transducers to generate pulses of various f_0 and Δf .

All the three tissue models were probed with 7 different interrogating pulses. In each case, 20 different statistically independent simulations were performed. This is analogous to collecting 20-A-line signals from the region of interest, each time moving the transducer by a distance greater than the beam width. Every parameter computed from the first order statistics of the signal, therefore, is an average of 20-A-line simulations.

RESULTS

- (1) Figure-3 shows intensity SNR values for all three tissue models as a function of $1/V_e$, where V_e , to be defined later, is a measure of the space occupied by the intensity point spread function. Also shown along $1/V_e$ are the resolution cell volume values from Table 1, for the 7 different pulses. In the limit of large cell volume, the SNR approaches the Raleigh high density limiting value of 1. The behavior is similar to that observed by Osterveld et. al. except that in their case the scatterer number density was varied for a fixed resolution cell volume [4]. As we will see later, the two quantities play equivalent role in determining this limiting behavior.

Table 1. Imaging pulse parameters

LABEL	Center Freq MHz	Band Width MHz	Pulse Width μ S	Beam Width mm	FWHM cell size mm ³
A	1.00	0.50	1.60	1.59	2.48
B	2.00	1.02	0.80	0.81	0.32
C	3.00	1.57	0.50	0.53	0.09
D	4.00	2.12	0.40	0.41	0.04
E	2.00	0.50	1.60	0.83	0.67
F	3.00	1.02	0.80	0.55	0.15
G	4.00	1.57	0.50	0.41	0.05

Approximate calculations of the number of scatterers within the FWHM cell volume show that the 90% of the limiting value is reached when this number is about 10. This result is comparable to other published results [4,7]. We also note that the limiting SNR value is 5-10% higher than expected value. This could be due to a residual specular term that comes from a non-zero mean gaussian profile for the RF signal. Wagner et. al. have shown that in the Raleigh limit it will produce SNR value higher than 1 [7].

- (2) It is instructive to examine the results from our simulation experiments in the light of the theoretical predictions by Cardoso [9]. He has derived expression for intensity SNR values, below the Raleigh limit:

$$SNR = (1 - 1/Ne)^{1/2} \quad (7)$$

with

$$Ne = n \cdot Ve \cdot \left[\frac{E^2(w^2)}{E(w^4)} \right] = n \cdot Ve \cdot \infty \quad (8)$$

where n is scatterer number density, E(*) represents the statistical expectation value and the "effective volume" Ve is defined as:

$$Ve = \frac{c}{2} \cdot \frac{[\int B(r) \cdot 2\pi r \cdot dr \int \hat{h}(t) dt]^2}{\int B^2(r) \cdot 2\pi r \cdot dr \int \hat{h}^2(t) dt} \quad (9)$$

Equation (7) indicates that SNR approaches the limiting value of 1 as Ne becomes large. Equation (8) shows that this can happen as n → large (high scatterer density) or as Ve → large. It is the later behavior that we have studied and demonstrated with our simulation experiments. We have varied the "effective volume" Ve by changing f₀ and Δf which in turn effect the beam profile B(r) and pulse envelope ĥ(t) respectively. Both n and Ve play equivalent role in determining the behavior of SNR. There is another parameter ∞ in Ne which is related to statistical variability of the scattering strengths. It is the ratio of the square of second moment to the fourth moment of the probability distribution of scattering strengths. In our model, this distribution is zero mean gaussian and therefore ∞ = 1/3 [10].

From our knowledge of B(r) and ĥ(t) we have calculated 1/ve for each of the 7 pulse point spread functions. This is the value used for abscissa in Fig. 3. Equation (7) and (8) indicate that [(SNR)² - 1] should vary linearly with 1/ve with zero intercept and slope given by 1/(n·∞). Thus if ∞ does not change, the slope becomes inversely proportional to number density. Fig. 4 shows this behavior for all 3 tissue models with different number densities. As expected, we observe a linear dependence. The slopes are inversely proportional to n or directly proportional to the third power of mean spacing: S³. This method of analysis can be used to estimate n for tissue characterization, provided we know Ve or if it can be estimated from the data.

- (3) Ultrasound speckle is stochastic in nature. In the high density limit the histogram of speckle amplitude follows

a Rayleigh probability distribution (PDF). The SNR contains information about the first and second central moments of the PDF. Since the values of the moments give information about the shape of the PDF, it is reasonable to assume that SNR gives some information about the shape variations as we change number density n or effective cell volume Ve. But higher order moments may contain additional information about the PDF. For example, higher the order of the moment, the greater is the contribution to it by the tails of PDF, hence more information it gives about the nature of the tails. Therefore, it has been suggested that in addition to SNR, higher order moments should be considered for tissue characterization [8]. However, to our knowledge, no systematic study has been performed to look into the effect of resolution cell volume on the higher order moments. We have analyzed our data towards this objective. We define the nth order normalized moment M_n of the envelope detected data as the ratio of nth moment divided by nth power of the first moment. The second to sixth order normalized moments are shown in figure 5(a) and 5(b) for tissue model 1 and 3 respectively. Seven different values are obtained for each moment, corresponding to seven different imaging pulses used to interrogate the tissue model. Pulse label has been arranged in the order of decreasing cell volume. Clearly, the higher order moments are more sensitive to the variations in cell volume. In other words, the departure from the Rayleigh limit is more prominent for higher order moments. As the cell volume increases, all the moments approach their respective Rayleigh limit value.

Figure 6(a) and 6(b) show the values of these moments for the three different tissue models. Fig 6(b) is from data with pulse D with the smallest cell volume. Here we notice increasing power to discriminate between different tissue types, as we go to higher moments. Data for Fig. 6(a) comes from pulse A that has the largest cell volume. Notice that the differences between different tissue models has decreased significantly, even for the higher order moments. With this particular imaging system, it would be difficult to discriminate between the three tissue types.

CONCLUSIONS

In this paper we have examined the role played by an imaging system's point spread function in controlling and changing the speckle statistics. From tissue characterization point of view it is desirable to be in the so called "below the Rayleigh limit" region. Analysis of our data shows that this limit is reached when there are fewer than 10 scatterers per resolution cell volume. We have shown that ability to change the cell volume can be useful in either achieving this limit or moving away from it. We observe a deviation from the limiting value of 1 for intensity SNR, as a function of decreasing cell volume. The functional behavior of the deviations observed is in close agreement with the existing theoretical predictions that incorporate the effect of PSF on SNR. We have also demonstrated that scatterer density n could be calculated from SNR measurements, provided we are below the Rayleigh limit and we have a knowledge of the PSF. It is tempting to suggest that PSF could be estimated from the 2D autocorrelation of the

speckle data. But It has been shown that below the Rayleigh limit autocorrelation function also experiences departure from its limiting behavior [4,7]. Ability to change cell volume may also prove to be useful in evaluating the PSF under Rayleigh limit conditions.

SNR involves only the first and second central moments. It is possible that higher moments carry more information and may be more sensitive to variations in scatterer density. Analysis of our data confirms this, but it also shows that higher moments are more sensitive to variations in imaging system's PSF as well. Therefore, care must be exercised in building a data base by analyzing data from different systems. We have also demonstrated that the sensitivity of higher moments to changes in number density of scatterers is a strong function of the Imaging systems resolution cell volume or PSF. Therefore, ability to vary PSF could be used to our advantage.

ACKNOWLEDGEMENTS

This work was supported in part by a grant-in-aid #881095 awarded by the American Heart Association and by a DuPont science and engineering grant.

REFERENCES

1. Burckhardt, C.B. "Speckle in ultrasound B-mode scans," IEEE Trans. on Sonics & Ultrasonics, Vol. 25, pp 1-6, 1978.
2. Sleefe, G.E. and P. Lele, "Tissue characterization based on scatterer number density estimation," IEEE Trans. on UFFC, Vol. 35, No. 6, pp 749-757, 1988.
3. Rao, N.A.H.K., Hui Zhu, "Scatterer Number Density Estimation Using Frequency Modulated Ultrasound Pulse," IEEE 1989 Ultrasonic Symposium, Vol. 2, pp 911-916, 1989.

4. Osterveld, B.J., Thijssen, J.M., and Verhoef, W.A., Texture of B-mode echograms: 3-D simulations and experiments of the effects of diffraction and scatterer density. *Ultrasonic Imaging* 7, 142-160, 1985.
5. Kuc, R., "A Computer model for stimulating reflected ultrasound signals," J. Acoustic Soc. Am. Vol. 80, pp 951-54, 1986.
6. Rao, N.A.H.K., "Frequency Modulated Pulse for Ultrasonic Imaging in an Attenuating Medium," Proc. of 3rd Annual IEEE Symposium on Computer Based Medical Systems, pp 89-95, June 1990.
7. Wagner, R.F., M.R. Insanan, and S.W. Smith, "Fundamental correlation lengths of coherent speckle in Medical Ultrasonic Images," IEEE Trans. on UFFC, Vol. 35, No. 1, pp 34-44, 1988.
8. Weng, L.M., J.M. Reig, P.M. Shankar, K. Soetanto, Y. Li, X. Lu, H. Oung, R. Raghavan, V. Enis and A.W.Schmidt, "Moments and Phase of non-Rayleigh speckle statistics applied to Ultrasound image analysis," IEEE Eng. Med. & Biol. Soc. International Conf. Vol. 12, No. 1, pp 333-334, 1990.
9. Cardoso, J.F., "3-D Ultrasonic speckle modeling: below the Rayleigh limit," International Symposium on Pattern Recognition and Acoustical Imaging, SPIE Vol. 768, pp 207-214, 1987.
10. Kuc, R., "Ultrasonic tissue characterization using Kurtosis," IEEE Trans. Ultrasonics Ferroelec. Freq. Contr., UFFC-33, No. 3, pp 273-279, 1986.

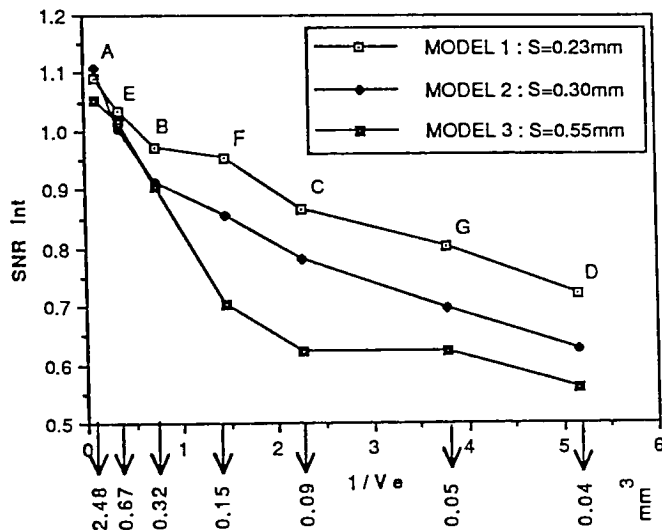


Figure 3: Intensity SNR vs 1/Ve for three different tissue models.

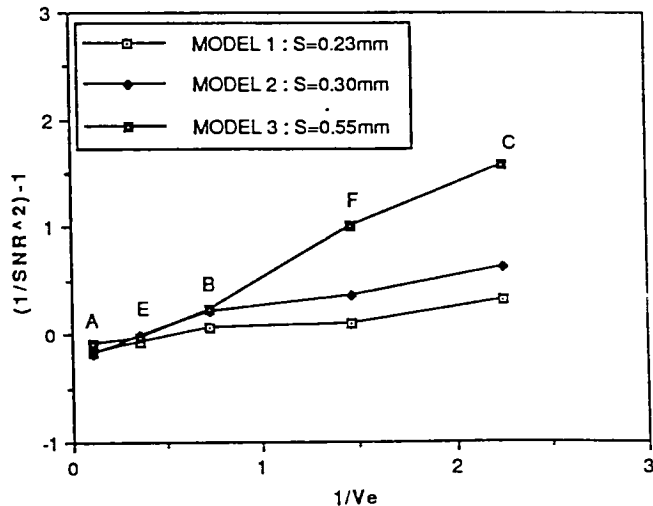


Figure 4 : (1/SNR²)-1 vs 1/Ve

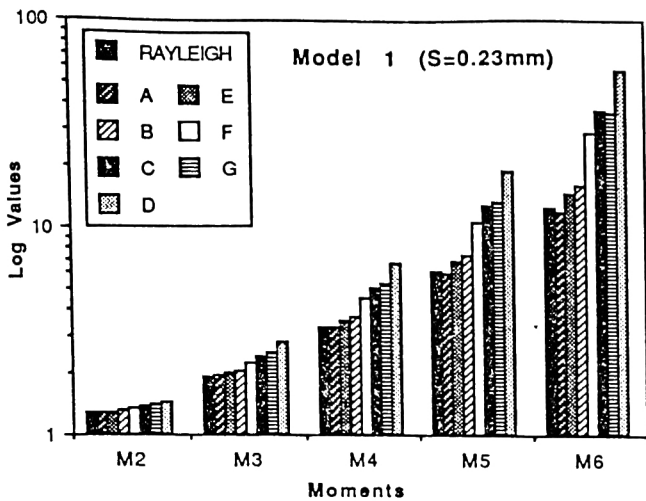


Figure 5(a) : Moment analysis of data from tissue model 1 for all the different imaging pulses

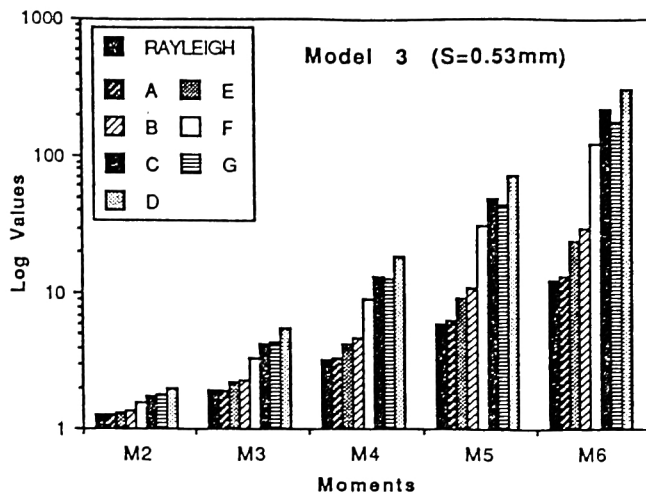


Figure 5(b) : Moment analysis of data from tissue model 3 for all the different imaging pulses

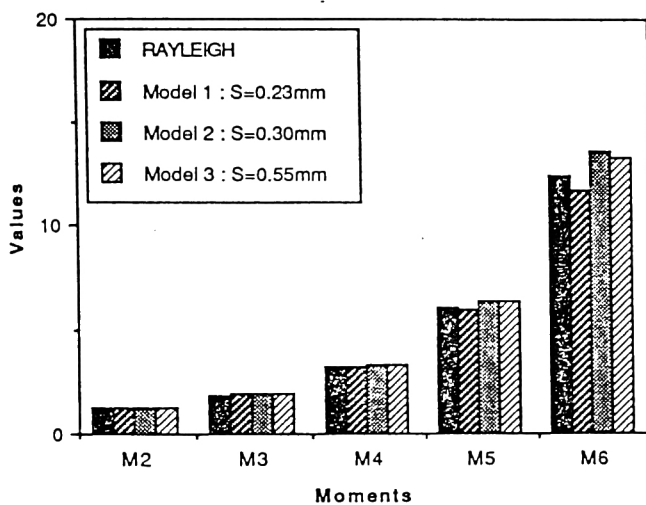


Figure 6(a) : Moment analysis of data from imaging pulse "A"

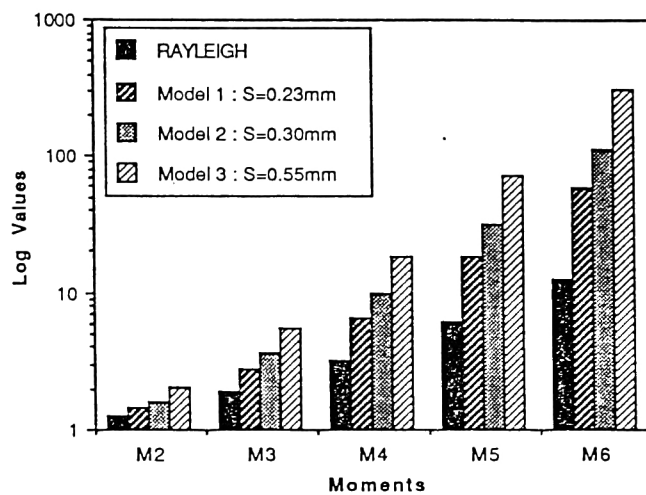


Figure 6(b) : Moment analysis of data from imaging pulse "D"

References

Arditi, M., Foster, F.S. and Hunt, J.W., (1981). "Transient Fields of Concave Annular Arrays", *Ultrasonic Imaging*, Vol. 3, pp. 37-61.

Bamber, J.C. and Dickinson, R. J., (1980). "Ultrasonic B-Scanning: A computer Simulation", *Phys. Med. Biol.*, Vol. 25, pp. 463-479.

Bartum, R. and Crowe, H., (1983). Real Time Ultrasound, Saunders, Philadelphia.

Baum, G., (1978). "The Current Status of Ultrasound Mamography", *Ultrasound in Medicine*, Vol. 4, Plenum Press, New York.

Burckhardt, C.B., (1978). "Speckle in Ultrasound B-Mode SCans", *IEEE Trans. Sonics. Ultrason.*, Vol. SU-25(1), pp. 1-6.

Carson, P.L., Fischella, P.R. and Oughton, T.V., (1978). "Ultrasonic Power and Intensities Produced by Diagnostic Ultrasound Equipment", *Ultra. Med. & Biol.*, Vol. 3, pp. 341-350.

Cartestensen, E.L., (1987). "Acoustic Cavitation and the Safety of Diagnostic Ultrasound", *Ultrasound Med. Biol.*, Vol. 13, pp. 597-606.

Claesson, I. and Salomomsson, G., (1988). "Frequency and Depth Dependent Compensation of Ultrasonic Signals", *IEEE Transactions on Ultrasonics, Ferroelectrics, and Frequency Control*, Vol. 35 (5), pp. 582-592.

Crum, L.A. and Fowlkes, J.B., (1986). "Acoustic Cavitation Generated by Microsecond Pulses of Ultrasound", *Nature*, Vol. 319, pp. 52-54.

Elias, C.M., (1980). "An Ultrasonic Pseudo Random Signal Correlation System", *IEEE Trans. Sonic. Ultrasonics*, Vol. SU-27, pp. 1-7.

Erikson, K.R. *et.al.*, (1974). "Ultrasound in Medicine-A Review", *IEEE Trans. Sonics Ultrason.*, Vol. SU-12(3).

Evans, T.C., Jr. and Taenzer, J.C., (1980). "Ultrasound Imaging of Atherosclerosis in Carotid Arteries", *Appl. Radiology*.

Fay, B., Brendel, K. and Ludwig, G., (1976). *Ultrasound in Medicine and Biology*, Vol. 2, pp. 195.

Ferrari, L. and Jones, J.P., (1985). "The Propagation of Gaussian Modulated Pulses in Dissipative and/or Dispersive Media such as Tissue", *Ultrasound in Med. & Biol.*, Vol. 11(2), pp. 299-305.

Fish, P., (1990). Physics and Instrumentation of Diagnostic Medical Ultrasound, Wiley, New York.

Flynn, H.G., (1932). "Generation of Transient Cavities in Liquids by Microsecond Pulses of Ultrasound", *J. Acoust. Soc. Am.*, Vol. 72, pp. 1926-1932.

Follett, D.H. and Atkinson, P. (1976). "Ultrasonic Pulse-Echo System Design: Transmitter-Receiver Matching", *Ultrasound in Medicine and Biology*, pp. 326.

Fullerton, G.D. and Zagzebski, J.A. (eds.), (1980). Medical Physics of CT and Ultrasound: Tissue Imaging and Characterization, pp. 531, Madsen, E.L., American Institute of Physics Press, New York.

Fullerton, G.D. and Zagzebski, J.A. (eds.), (1980). Medical Physics of CT and Ultrasound : Tissue Imaging and Characterization, pp. 298, Hendee, W.R. and Holmer, J.H., American Institute of Physics Press, New York.

Goodman, J.W., (1976). "Some Fundamental Properties of Speckle", *J.Opt. Soc. Am.*, Vol. 66 (11), pp. 1145-1150.

Goodsitt, M.M., Bleier, A.R. and Barber, F.E., (1987). "An Improved Ultrasound Simulatio Model: Use in Evaluating Log Versus Linear Processing for Lesion Detection", *Ultrasonic Imaging*, Vol. 9, pp. 260-270.

Gurumurthy, K.V. and Arthur, R. M., (1982). "A Dispersive Model for the Propagation of Ultrasound in Soft Tissue", *Ultrasonic Imaging*, Vol. 4, pp. 355-377.

Guyomar, D. and Powers, J., (1987). "A Fourier Approach to Diffraction of Pulsed Ultrasonic Waves in a Lossless Media", *J. Acoust. Soc. Am.*, Vol. 6, pp. 355-359.

Halliwell, M., (1979). "On the Ultrasonic Field Used in Medical Diagnosis", *Ph.D. Thesis*, Univ. of Bristol.

Havlice, J.F. and Taenzer, J.C., (1979). "Medical Ultrasonic Imaging: An Overview of Priciples and Instrumentation", *Proc. IEEE*, Vol. 67 (4), pp. 620-640.

Hertfeld, K.F. and Litovitz, T.A., (1959). Absorption and Dispersion of Ultrasonic Waves, Academic Press, New York.

Hykes, D.L., Hedrick, W.R. and Starchman, D.E., (1985). Ultrasound Physics and Instrumentation, Churchill Livingstone, New York.

Kak, A.C., Dines, K.A., (1978). "Signal Processing of Broadband Pulsed Ultrasound: Measurement of Attenuation of Soft Biological Tissues", *IEEE Transactions on Biomedical Engineering*, Vol. BME-25 (4), pp. 321-344.

Kinsler, L. and Frey, A., (1962). Fundamentals of Acoustics, 2nd ed., Wiley, New York.

Klauder, J.R., Price, A.C., Darlington, S. and Albershm, W.J., (1960). "The Theory and Design of Chirp Radars", *Bell System Tech. J.*, Vol 39, pp. 745-809.

Kossoff, G, (1979). "Analysis of Focusing Action of Spherically Curved Transducers", *Ultrasound Med. Biol.*, Vol. 5, pp. 359-369.

Kuc, R., Schwartz, M. and Lajos, V.M., (1976). "Parametric Estimation of the Acoustic Attenuation Coefficient Slope for Soft Tissue", *1976 Ultrasonic Symposium Proceedings, IEEE*, Cat. 76., pp. 44-47.

Kuc, R., (1984). "Modelling Acoustic Attenuation of Soft Tissue with a Minimum-Phase Filter", *Ultrasonic Imaging*, Vol. 6, pp. 24-36.

Kuc, R. and Miwa, H., (1986). "A Computer Model for Simulating Reflected Ultrasound Signals", *J. Acoust. Soc. Am.*, Vol. 80 (3), pp. 951-954.

Kuc, R., (1986). "Ultrasonic Tissue Characterization Using Kurtosis", *IEEE Transactions on Ultrasonics, Ferroelectrics, and Frequency Control*, Vol. UUF3-33 (3), pp. 273-279.

Lerch, R., Friedrich, W., (1986). "Ultrasound fields in attenuating media", *J. Acoust. Soc. Am.*, Vol. 80 (4), pp. 1140-1147.

Lewis, G.K., (1987). "Chirped PVDF Transducers for Medical Ultrasound Imaging", *IEEE Ultrasonics Symposium*, pp. 879-884.

Linzer, M. (ed.), (1976). Ultrasonic Tissue Characterization, "Challenges and Opportunities in Ultrasound", Reed, J.M., National Bureau of Standards Special Publication, #453.

Madsen, E.L., Goodsit, M.M. and Zagzebski, J.A., (1981) "Continuous Wave Generated by Focused Radiators", *J. Acoust. Soc. Am.*, Vol. 70 (5), pp. 1508-1517.

Maginness, M.G., (1979). "Methods and Terminology for Diagnostic Ultrasound Imaging Systems", *Proceedings of the IEEE*, Vol. 67 (4), pp. 641-653.

Melton, H.E. and Magnin, P.A., (1984). "A-Mode Speckle Reduction with Compound Frequencies and Compound Bandwidths", *Ultrasonic Imaging*, Vol. 6, pp. 159-173.

Milne, E.N.C. (ed.), (1983). Models and Techniques in Medical Imaging Research, pp. 466, Praeger Publishers Div.

Ninkoonahad, M and Iravani, M.V, (1989). "Focusing Ultrasound in Biological Media", *IEEE Trans. UFFC*, Vol. 36(2), pp. 209-215.

O'Donnell, M., Jaynes, E.T. and Miller, J.G., (1978). "General Relationship Between Ultrasonic Attenuation and Dispersion", *J. Acoust. Soc. Am.*, Vol. 63 (6), pp. 1935-1937.

Olinger, C.P. and Nigam, A.K., (1978). "Application of High-Resolution Imaging to the DEtection and Preliminary Characterization of Artherosclerosis", *Ultrasound in Medicine.*, Vol. 4, Plenum Press, New York.

Rao, N.A.H.K., Ritenour, R.E., Hendrick, R.E., (1988). "Frequency Modulated Pulse for Ultrasonic Imaging in an Attenuating Medium", *SPIE Proceedings on Medical Imaging II*, Vol. 914, pp. 67-74.

Rao, N.A.H.K., (1990). "Frequency Modulated Pulse for Ultrasonic Imaging in an Attenuating Medium", *IEEE Symp. Comp. Med. Sys.*, pp. 89-95.

Rao, N.A.H.K., Mehra, S. and Zhu, H., (1990). "Ultrasound Speckle Statistics Variations with Imaging System Impulse Response", *IEEE Ultrasonics Symposium*, pp. 1435-1440.

- Rao, N.A.H.K. and Zhu, H., (1989). "Scatterer Number Density Estimation Using Frequency Modulated Ultrasound Pulse", *Proc. of IEEE 1989 Ultrasonic Symposium*, Vol. 2, pp. 911-916.
- Rao, N. and Zhu, H., (1991). "Modeling Ultrasound Speckle Formation and its Dependence on Imaging Systems Response", *SPIE Proceedings on Medical Imaging V*.
- Reid, J. and Wild, J., (1952). "Application of Echo Ranging Techniques in Determination of Structure of Biological Tissues", *Science*, Vol. 115, pp. 226-230.
- Riesz, P., Berdahl, D. and Christman, (1985). "Free Radical Generation by Ultrasound in Aqueous and Nonaqueous Solutions", *Environ, Health Persp.*, Vol. 64, p. 233.
- Rose, J.L. and Goldgerg, B.B., (1979). Basic Physics in Diagnostic Ultrasound, Wiley, New York.
- Shoup, T.A. and Hart, J., (1988). "Ultrasonic Imaging Systems", *IEEE Ultrasonics Symposium*, pp. 863-871.
- Swenberg, C.E. and Conklin, J.J. (eds.), (1988), Imaging Techniques in Biology and Medicine, pp. 111-165, "Fundamental Principles of Imaging by Ultrasound", McCormack, P.D., Academic Press, New York.
- Tucker, D.G. *et al.*, (1958). "Electronic Sector Scanning", *Brit. Inst. Radio. Eng.*, Vol. 26, p. 465.
- Verhoef, W.A., Cloostermens, M.J.T.M and Thijssen, J.M., (1984). "The Impulse Response of a Focused Source with an Arbitrary Axisymmetric Surface Velocity Distribution", *J.Acoust. Soc. Am.*, Vol. 75, pp. 1716-1721.

Wagner, R.F., Smith, S.W., Sandrik, J.M. and Lopez, H., (1983). "Statistics of Speckle in Ultrasound B-Scans", *IEEE Transactions on Sonics and Ultrasonics*, Vol. 30 (3), pp. 156-163.

Webb, S. (ed.), (1988). The Physics of Medical Imaging, "Diagnostic Ultrasound", Bamber, J.C. and Tristram, M., pp. 319-388, Adam Hilger, Philadelphia.

Wells, P.N.T., (1969). Physical Principles of Ultrasonic Diagnosis, Academic Press, New York.

Weng, L., Reid, J.M., Shankar, P.M., Soetanto, K., Li, Y., Lu, X., Oung, H., Raghvan, R., Genis, V. and Schmidt, A.W., (1990). "Moments and Phase of Non-Rayleigh Speckle Statistics Applied to Ultrasound Image Analysis", *IEEE Engineering in Medicine and Biology Society*, Vol. 12 (1), pp. 333-334.

White, D.N. and Lyons, E.A. (eds.), (1978). Ultrasound in Medicine, Vol. 4, pp. 467, Madsen, E. Zagzebski, J.A., Banjavic, R.A. and Jutila, R., Pelnum Press, New York.